November 29, 2006

Chandra Multiwavelength Project X-ray Point Source Catalog

Minsun Kim[1,2], Dong-Woo Kim[1], Belinda J. Wilkes[1], Paul J. Green[1], Eunhyeuk Kim[1], Craig S. Anderson[1], Wayne A. Barkhouse[3], Nancy R. Evans[1], Željko Ivezić[4], Margarita Karovska[1], Vinay L. Kashyap[1], Myung Gyoon Lee[2], Peter Maksym[5], Amy E. Mossman[1], John D. Silverman[6], and Harvey D. Tananbaum[1]

mkim@cfa.harvard.edu

ABSTRACT

We present the *Chandra* Multiwavelength Project (ChaMP) X-ray point source catalog with $\sim 6{,}800$ X-ray sources detected in 149 *Chandra* observations covering ~ 10 deg^2. The full ChaMP catalog sample is seven times larger than the initial published ChaMP catalog. The exposure time of the fields in our sample ranges from 0.9 to 124 ksec, corresponding to a deepest X-ray flux limit of $f_{0.5-8.0} = 9 \times 10^{-16}$ $erg\ cm^{-2}\ sec^{-1}$. The ChaMP X-ray data have been uniformly reduced and analyzed with ChaMP-specific pipelines, and then carefully validated by visual inspection. The ChaMP catalog includes X-ray photometric data in 8 different energy bands as well as X-ray spectral hardness ratios and colors.

To best utilize the ChaMP catalog, we also present the source reliability, detection probability and positional uncertainty. To quantitatively assess those parameters, we performed extensive simulations. In particular, we present a set of empirical equations: the flux limit as a function of effective exposure time, and the positional uncertainty as a function of source counts and off axis angle. The false source detection rate is $\sim 1\%$ of all detected ChaMP sources, while the detection probability is better than

[1]Harvard-Smithsonian Center for Astrophysics, 60 Garden Street, Cambridge, MA 02138, USA

[2]Department of Physics and Astronomy, Astronomy Program, Seoul National University, Seoul 151-742, Korea

[3]Department of Astronomy, University of Illinois at Urbana-Champaign, Urbana, IL 61801, USA

[4]Department of Astronomy, University of Washington, Seattle, WA 98195, USA

[5]Department of Physics and Astronomy, Northwestern University, Evanston, IL 60208, USA

[6]Max-Planck-Institut für extraterrestrische Physik, D-84571 Garching, Germany

$\sim 95\%$ for sources with counts $\gtrsim 30$ and off axis angle $< 5'$. The typical positional offset between ChaMP X-ray source and their *SDSS* optical counterparts is $0.7 \pm 0.4''$, derived from ~ 900 matched sources.

Subject headings: surveys — X-rays: X-ray point source catalog — X-ray: general
On-line material: machine-readable tables

1. Introduction

Since the cosmic X-ray background (hereafter CXRB) was discovered by Giacconi et al. (1962), there have been several X-ray missions such as *Einstein*, *ROSAT*, *ASCA* and *BeppoSAX*. The *Chandra X-ray Observatory* (hereafter *Chandra*) and the *X-ray Multi-Mirror Mission-Newton* (hereafter *XMM-Newton*) are the current powerful X-ray missions with more sensitive imaging spectroscopy and higher positional accuracy than previous missions. To investigate the formation and evolution of galaxies, clusters of galaxies, and large scale structure of the universe, these previous and current X-ray missions have provided several deep and wide extra galactic X-ray surveys (see Brandt & Hasinger (2005) and references therein for a detailed review). Bauer et al. (2004) established the X-ray number counts from the *Chandra* Deep Field North (CDF-N) and South (CDF-S) and found that $\sim 90\%$ ($\sim 93\%$) of the CXRB is resolved into discrete X-ray sources in the 0.5-2 keV (2-8 keV) band. Using the *XMM-Newton* observation of the Lockman Hole and the CDFs, Worsley et al. (2005) found that the resolved fractions of the CXRB are $\sim 85\%$ (0.5-2 keV), $\sim 80\%$ (2-10 keV), and $\sim 50\%$ ($\gtrsim 8$ keV), respectively. Therefore, the CXRB is predominantly resolved into discrete sources in the 0.5-2 keV and 2-10 keV bands; however, the constituents of the CXRB in the hard energy band ($\gtrsim 8$ keV) are still unknown.

The deepest X-ray surveys are the 2*Msec* CDF-N (Brandt et al. 2001; Alexander et al. 2003) and the 1*Msec* CDF-S (Giacconi et al. 2001; Rosati et al. 2002) covering small sky areas ($\sim 0.12\ deg^2$). The faint flux limits of the CDFs are $\sim 2 \times 10^{-17}\ erg\ cm^{-2}\ sec^{-1}$ (0.5-2 keV) and $\sim 2 \times 10^{-16}\ erg\ cm^{-2}\ sec^{-1}$ (2-8 keV), respectively. The *XMM-Newton* survey of the Lockman Hole covers $\sim 0.43\ deg^2$ with an effective exposure time of ~ 700 *ksec* (flux range of $\sim few \times 10^{-16} \sim 3 - 5 \times 10^{-14}$ $erg\ cm^{-2}\ sec^{-1}$ in each band) (Worsley et al. 2004). The XMM large scale structure survey (*XMM-LSS*) is a medium depth (~ 10 *ksec*) and large area ($\sim 64\ deg^2$) X-ray survey (Pierre et al. 2004). The $3\ deg^2$ XMM medium depth survey (XMDS) pointed at the center of $XMM-LSS$ reaches a flux limit of $\sim 10^{-15}\ erg\ cm^{-2}\ sec^{-1}$ in the 0.5-2 keV band (Chiappetti et al. 2005). The *Chandra* X-ray survey of the NDWFS Boötes is a contiguous wide ($\sim 9.3\ deg^2$) and medium depth (~ 5 *ksec*) survey and contains 4642 sources with flux limits of $4 \times 10^{-15}\ erg\ cm^{-2}\ sec^{-1}$ in the 0.5-7 keV band (Murray et al. 2005).

The Chandra Multiwavelength Project (ChaMP) is a serendipitous *Chandra* archival survey of X-ray sources covering a wide area ($\sim 10\ deg^2$) with a range of depths $0.9 \sim 124$ *ksec* exposures. The main scientific goals of the ChaMP are to investigate the (1) formation and evolution of high redshift AGN, (2) properties of X-ray luminous galaxies and clusters, and (3) constituents of the CXRB. Kim, D.-W. et al. (2004a, hereafter Paper I) reported the first ChaMP X-ray source catalog including 991 near on-axis, bright X-ray sources obtained from 62 ChaMP fields and Green et al. (2004) have performed optical and spectroscopic follow up observations of a subset of these ChaMP X-ray sources.

Using the first ChaMP X-ray point source catalog and the follow up surveys of optical and spectroscopic observations, there have been several interesting results. Kim, D.-W. et al. (2004b) established the number counts of the ChaMP X-ray point sources in the 0.5-2 keV and the 2-8 keV bands, which agreed with previous studies within the uncertainties, and found that there are no significant field-to-field variations in cosmic X-ray source number density on the scale of $\sim 16'$ which corresponds to a single *Chandra* observational field of view. Silverman et al. (2005a) found the turnover in the co-moving space density of X-ray selected, luminous type 1 AGN ($logL_x > 44.5\ erg\ sec^{-1}$ measured in the 0.3-8 keV band) to be at $z > 2.5$ consistent with the optical results. The hard X-ray emitting AGNs in twenty ChaMP fields were investigated and classified as broad emission-line AGN (62%), narrow emission-line galaxies (24%), absorption line galaxies (7%), stars (5%), or clusters (2%). Most X-ray unabsorbed AGN ($N_H < 10^{22}\ cm^{-2}$) have broad emission lines and blue optical colors but there is a significant population of redder AGNs with broad optical emission lines. Most X-ray absorbed AGN ($10^{22} < N_H < 10^{24}\ cm^{-2}$) are associated with narrow emission-line galaxies, those with red optical colors being dominated by luminous, early type galaxy hosts rather than dust reddened AGN (Silverman et al. 2005b). Barkhouse et al. (2006) presented the ChaMP X-ray extended source catalog which contains 55 extended sources from 130 *Chandra* fields. From the overlapping optical/X-ray fields ($6.1\ deg^2$) they found 115 optical cluster candidates of which 13 were detected as extended X-ray sources. A comparison of the richness of the optical-only versus X-ray/optically matched cluster samples shows that the average richness of the optical-only clusters is smaller by $\sim 4\sigma$ than the matched X-ray/optical clusters. This result suggests that the optical-only sample is either (1) composed of mainly poor systems that lack sufficient hot gas for detection in the X-rays, or (2) are contaminated by nonvirialized filaments associated with the large-scale structure. Kim, D.-W. et al. (2006) investigated the normal galaxies at intermediate redshift in the ChaMP fields and found that normal galaxies at redshift, $z < 0.1$ do not show significant evolution in L_X/L_B. They built cumulative number counts and luminosity functions of the normal galaxies, and they found that a group of NELGs appear to be heavily obscured in X-rays while the low redshift AGNs in this sample do not appear to be significantly absorbed. Also, they found two E+A galaxy candidates and they concluded that those galaxies support the merger/interaction scenario of galaxy formation from their X-ray spectra studies.

In this paper, we present the ChaMP X-ray point source catalog including $\sim 6,800$ X-ray point sources obtained from 149 ChaMP fields and covering a sky area of $\sim 10\ deg^2$. Compared to the first ChaMP X-ray point source catalog, this catalog contains seven times more sources, covers three times more sky area, and includes fainter sources and those with larger off axis angle. We performed extensive simulations to investigate the sensitivity, source probability, and positional uncertainty of the ChaMP sources. This catalog allows more statistically robust results from X-ray point source studies. The ChaMP data reduction procedures are similar to those in Paper I, therefore, we briefly summarize and/or skip those parts which are already described in Paper I and concentrate on newly added or improved procedures. In §2, we summarize the selection criteria and properties of the ChaMP fields. In §3, the data reduction and analysis of the ChaMP are described. §4 discusses the process and results of the ChaMP simulations. The ChaMP X-ray point source catalogs are provided in §5, and a summary and conclusions are given in §6.

2. ChaMP Field Selection

We selected *Chandra* fields observed with ACIS at high Galactic latitude, $|b| > 20^\circ$ and excluded those fields containing large extended sources, planetary observations, and local group galaxies. Fields intended by their PIs as surveys were also excluded (see Paper I). These selection criteria yield 149 ChaMP fields in *Chandra* cycles 1 and 2, consisting of 35 ACIS-I and 114 ACIS-S observations. 7 ACIS-I and 28 ACIS-S ChaMP fields partly overlap one another on the sky, and those sources detected in multiple observations are listed separately, for example to allow study of source variability. In Table 1, the observational parameters of 149 ChaMP fields are listed in order of right ascension.

In Figure 1, we display the 149 ChaMP field locations in equatorial coordinates. Red circles represent ACIS-I at the aim point, and blue circles ACIS-S. The circle size crudely indicates the Chandra exposure time, ranging from 0.9 to 124 ksecs. The ChaMP samples are uniformly distributed over the entire celestial sphere except (by selection) the Galactic plane region. Figure 2 shows the number distributions of the exposure times and Galactic extinction of the ChaMP fields in top and bottom panels, respectively. The mean exposure time of the ChaMP is ~ 25 *ksec* and the mean Galactic extinction, $N_H = (3.4 \pm 2.2) \times 10^{20}\ cm^{-2}$. The ChaMP samples cover a wide range of exposure times and the Galactic extinction of the ChaMP fields are generally much lower than those of Galactic plane ($N_H \sim 10^{22} \sim 10^{23}\ cm^{-2}$). The 62 ChaMP fields included in Paper I are represented by shaded histograms. In this study, the X-ray point source catalog includes all X-ray sources in 149 ChaMP fields as well as fainter and larger off axis angle sources, while the catalog in Paper I included only near on-axis ($off\ axis\ angle < 6'$ or S3 chip for ACIS-S observations) and bright (*net counts* > 20) sources in 62 ChaMP fields.

3. ChaMP Data Reduction

We have developed a ChaMP-specific pipeline, XPIPE, to reduce the *Chandra* data. The pipeline consists of three main parts; (1) data correction and data screening using the CIAO[1] package, (2) source detection using the *wavdetect* tool in the CIAO package, and (3) source extraction using the *xapphot* tool (Kim, E. et al. 2006; Martini et al. 2006) based on $cfitsio$[2] library. The data correction and data screening procedures are the same as in Paper I. We do not use sources detected in the S4 chip (CCDID=8) because of the streaking problem (see Paper I).

3.1. Source Detection

For source detection, we use the *wavdetect* tool available in the CIAO package. *wavdetect* consists of two parts: *wtransform*, convolving the data with the wavelet function for selected size scales; and *wrecon*, constructing a final source list and estimating various parameters for each source (Freeman et al. 2002). We run *wavdetect* in the B band (see Table 2 for energy band definition) with a significance threshold parameter of 10^{-6}, which corresponds to one possible spurious pixel in one CCD (see §4.3.2 for our simulation results on the probability of finding a spurious source). We select a range of scale size parameters in seven steps from 1 to 64 pixels ($1 pixel = 0.492''$). To avoid finding spurious sources located at the edge of the CCD chips, a minimum of 10% of the on-axis exposure was required for source detection. Exposure maps of the ChaMP fields were generated for each CCD at an energy of 1.5 keV with an appropriate aspect histogram [3]. Other parameters were set at the default values given in *wavdetect*. The positions provided by *wavdetect* in CIAO 2.3 for off-axis sources, where the shape of the Point Spread Function (PSF) is highly asymmetrical and the background contribution to the counts in the source cell is non-negligible, are less accurate than the positions of on-axis sources (Paper I). To alleviate this problem, we applied a position refinement algorithm (P. Freeman 2003, private communication), which iteratively redetermines the position of the off-axis source until it converges on the best centroid (see Paper I for detail descriptions), to the X-ray positions determined by *wavdetect* in CIAO 2.3. When CIAO 3.0 or later versions are used, this process is not necessary, because the position refinement algorithm has been applied in *wavdetect*[4].

---

[1] See http://cxc.harvard.edu/ciao.

[2] See http://heasarc.gsfc.nasa.gov/docs/software/fitsio/fitsio.html.

[3] See http://cxc.harvard.edu/ciao/threads/expmap_acis_single.

[4] See http://cxc.harvard.edu/ciao/releasenotes/ciao_3.0_release.html.

The size and shape of the PSF for *Chandra* varies as a function of off axis angle and radial direction. *wavdetect* uses a Mexican Hat function, a reasonable function for mirrors/detectors which are characterized by a quasi-Gaussian PSF, and which detects sources successfully in most cases. However, the off-axis PSF is asymmetric and contains sub-structure in the core, causing *wavdetect* to detect sometimes a spurious pair of double sources. We note that the sub-structure of the off-axis PSF can be resolved by *wavdetect* because the size of the PSF becomes larger with increasing off axis angle. This PSF effect can be corrected by a PSF deconvolution (Paper I). In Paper I, source pairs with small separations were inspected and three pairs of spurious doubles were found, bright (*net counts* $>$ a few hundreds counts) enough to deconvolve with their PSFs. In this study, to identify and correct this PSF effect, we generated a single PSF image at the median location of each overlapping pair of sources whose positional centers are very close together (see §3.2.2 for quantitative definition of large overlapping sources) and a second image using a combination of two source PSFs. We then compared the observed source image with the modeled images. To generate the PSF images, we used a PSF ray trace tool *ChaRT*[5] and a *Chandra* detector simulation tool MARX[6] assuming a monochromatic energy at 1.5 keV and a source counts ratio corresponding to that of overlapping sources as determined by XPIPE.

We found twelve pairs of spurious double sources and Figure 3 shows the observed sources image and the modeled images for a sample pair. First, we can see that the PSF shape at this location is asymmetric (*middle*) and the positional centers of the spurious double sources are located along the elongated PSF direction. The shape of the observed X-ray sources (*left*) is similar to the single PSF (*middle*) rather than that of the double source PSFs (*right*). Therefore, we conclude that *wavdetect* has incorrectly detected a single source as a double source due to the asymmetric sub-structure in the PSF. All double sources found to be spurious are too faint (*net counts* $<$ a few hundred counts) to deconvolve with their PSFs. Therefore, we assigned the median position of the spurious double sources as the new position of the single source and half of the distance between double sources was quadratically summed to their positional uncertainties (see §4.2.1 for the positional uncertainty of the ChaMP X-ray point sources). The source counts were then extracted at the new source position (see §3.2 for the source counts extraction).

3.2. Source Properties

After detecting X-ray sources with *wavdetect*, we extracted their X-ray properties by applying aperture photometry. Since *wavdetect* sometimes underestimates the net counts for faint sources

[5]See http://asc.harvard.edu/chart/threads/index.html.

[6]See http://space.mit.edu/CXC/MARX/.

(see §4.3), we do not use the *wavdetect*-determined X-ray photometry. Instead, we apply an aperture photometry source extraction tool *xapphot*, developed for a general purpose and applicable to both *Chandra* and XMM-Newton data (Kim, E. et al. 2006). We note that XPIPE detects the source positions only in the B band with *wavdetect* and applies the same position and size for the source extraction regions in every energy band. The reliability of the ChaMP source properties using XPIPE will be discussed in §4.3.

3.2.1. Source Count Extraction Regions

With the X-ray source position determined by *wavdetect*, we extract source counts from a circle with a 95% encircled energy radius, determined at 1.5 keV from the PSF table [7]. A minimum radius of $3''$ and maximum of $40''$ are chosen to avoid small number statistics in the source counts and severe fluctuations in the background sky. The source radii in this study are slightly smaller than those in Paper I which used an older version of the PSF tables. In the top panel of Figure 4, the source radius for Paper I (*dotted line*) and that for this study (*solid line*) are displayed as a function of off axis angle. The difference between source sizes is plotted as a dashed line, indicating a significant difference at large off axis angle. The source size is reduced by a maximum of $\sim 18''$ at off axis angle of $\sim 13'$ and unchanged in the axis region of $\lesssim 3'$ compared to the old source size. In the bottom panel of Figure 4, the difference between source counts in this and previous studies are displayed. The reduced source radii yield an average net counts lower by $2 \pm 7\%$ in this catalog compared with Paper I.

The size of the background extraction annulus is a free parameter generally chosen within the range 2 to 5 times the source radius, depending on local and global background fluctuations. However, for point sources inside an extended source, the size of the background extraction annulus was set to 1 to 2 times the source radius because in this case local variations in the background are much more important than global variations. The ChaMP X-ray extended sources are identified by *wavdetect* with a large wavelet and source properties extracted via fitting with a Gaussian profile and a β model. The ChaMP extended source catalog used in the ChaMP point source photometry is provided in a separate paper (Barkhouse et al. 2006).

---

[7] See http://cxc.harvard.edu/cal/Hrma/psf/index.html.

3.2.2. Net Counts

The net counts N of a source in a given energy band are determined by subtracting the normalized background counts from the source counts in the source region as follows:

$$N = N_S - N_B/AR, \tag{1}$$

where N_S and N_B are the total counts in the source and background regions, respectively. The normalization factor AR in equation (1) is given by:

$$AR = \frac{< E_B > A_B}{< E_S > A_S}, \tag{2}$$

where $< E_S >$ and $< E_B >$ are the mean exposure times for the source and background regions, respectively, and A_S and A_B are the geometric areas of the two regions. To avoid contamination in the background region, we exclude other point and extended source regions within the background region. The net counts errors are derived following Gehrels (1986).

There is a significant probability that two or more sources will overlap with each other, especially at large off axis angle. Note that the PSF size increases exponentially with increasing off axis angle. For overlapping sources, simple aperture photometry overestimates the source counts. While simultaneous fitting of multiple PSFs may be a good way to deconvolve overlapping sources, this process requires sufficient counts (a few hundred), which is unusual for typical X-ray observations. Thus to determine the net counts for overlapping sources, we apply two independent correction methods as in Paper I, a small overlap correction and a large overlap correction, depending on the amount of overlapping area involved.

In the left side of Figure 5, we display a schematic diagram of a small overlapping source, in which the distance between them D_{12} is greater than the radius of each source but less than the sum of their radii:

$$0.5 < \frac{D_{12}}{D_{PSF}} < 1, \tag{3}$$

where D_{PSF} is the 95% encircled energy diameter of the PSF. A small overlap is the most common overlap among X-ray sources due to their relatively low density in the ChaMP fields. The corrected net counts N_1 and N_2 for the overlapping sources S1 and S2 are estimated as follows:

$$N_1 = 2\pi N_{1,A_1}/(2\pi - \theta_1), \tag{4}$$

$$N_2 = 2\pi N_{2,A_2}/(2\pi - \theta_2), \tag{5}$$

where N_{1,A_1} and N_{2,A_2} are the net counts of S1 in area A_1 and the net counts of S2 in area A_2, respectively. θ_1 and θ_2 are the angles in units of radians covered by sectors B_1 and B_2 of the

overlapping sources, respectively. We assumed a radially symmetric event distribution for both X-ray sources.

The right side of Figure 5 displays an example of large overlapping sources, where the distance D_{12} is less than the radius of each source. In this case, the center of each source is located within the source region of the overlapping partner, such that the above algorithm is not applicable. To correct this large overlapping case, first, we defined the core radius R_c of each source as follows:

$$R_c \equiv max\left(\frac{D_{12}}{3},\ 2\ pixels\right), \tag{6}$$

where D_{12} is the distance between two overlapping sources. R_c has a minimum of 2 *pixels* to allow a statistically robust estimation of the counts within the core radius. The corrected net counts of the large overlapping sources N_1 and N_2 are estimated as follows:

$$N_1 = N_t(2N_{1,A_1} + N_{1,C_1})/N_0, \tag{7}$$

$$N_2 = N_t(2N_{2,A_2} + N_{2,C_2})/N_0, \tag{8}$$

$$N_0 = (2N_{1,A_1} + N_{1,C_1}) + (2N_{2,A_2} + N_{2,C_2}), \tag{9}$$

where N_t is the sum of net counts of S1 and S2 (i.e. net counts in a union area of two source regions). N_{1,A_1} and N_{2,A_2} are the net counts of S1 in region A_1 and the net counts of S2 in region A_2, respectively. N_{1,C_1} and N_{2,C_2} are the net counts of S1 in core region C_1 and the net counts of S2 in core region C_2, respectively. The radii of core regions C_1 and C_2 are calculated with equation (6) and have the same size. Since the core region of each source is contaminated by photons from the overlapping source, the photons in unperturbed regions (A_1 and A_2) are weighted higher than those in core regions (C_1 and C_2) by a factor of two. Excluding spurious sources, small and large overlap corrections were applied to 2.5% and 0.6% of the ChaMP sources, respectively. We note that *xapphot* does not include the correction procedure for a source overlapping largely with more than one source. However, only one such case is included in the ChaMP X-ray point source catalog: CXOMP J111816.9+074558, CXOMP J111816.8+074600, and CXOMP J111816.8+074557 overlap largely each other, and they are the target of the observation (OBSID=363, gravitationally lensed quasar) having a pile-up flag (flag=37, see Table 4 in §3.2.5).

3.2.3. Hardness Ratio and Colors

The X-ray point source properties are extracted in the five ChaMP specified energy bands and in the three commonly used energy bands. The used energy bands and definitions of hardness ratio (HR) and X-ray colors (C21 and C32) are listed in Table 2 and their scientific rationale was described in Paper I. The HR and X-ray colors can be calculated from the source net counts in

two different energy bands according to their definitions (hereafter classical method). However, for the faint sources, the HR, C21, and C32 and their error propagations from the classical method are often unreliable or unrealistic because of negative/undetectable net counts in one band or a non-Gaussian nature. Therefore, we calculated the HR, C21, and C32 with a Bayesian approach which models the detected counts as a Poisson distribution and which gives reliable HR and X-ray colors for both low and high count sources (van Dyk et al. 2004; Park et al. 2006).

To derive the HR and X-ray colors with the Bayesian approach, we used the BEHR[8] program (version 07-27-2006, Park et al. 2006) with the required inputs: source counts, background counts, and ratio of background area to source area in both energy bands. We assumed a non-informative, flat, prior distribution on the linear scale ($softidx = hardidx = 1$). We note that the energy-dependent vignetting in the soft and hard counts is not corrected for deriving the HR. The BEHR program calculates the solution with two different method: a Gibbs sampler (Monte Carlo integration) and a Gaussian quadrature (numerical integration). The Gibbs sampler is efficient but less accurate than the Gaussian quadrature for faint sources; however, the Gaussian quadrature becomes less efficient with increasing source counts. Therefore, we used the Gibbs sampler for bright sources ($net\ counts > 15$ in two energy bands) and Gaussian quadrature for faint sources ($net\ counts < 15$ in at least one energy band), respectively. The default values were used for the remaining optional inputs. The BEHR program calculates the mode, mean, and median of the posterior probability distribution. The mean of the distribution is a robust estimator for the HR, while the mode for the X-ray colors (Park et al. 2006). In Figure 6, we compare the classical method with the Bayesian approach for HR and X-ray colors. For bright sources ($S/N > 2$), the HR and X-ray colors from both methods agree well; however, for faint sources ($S/N < 2$), they do not agree, because the classical method using the Gaussian statistics fails to describe the nature of faint sources.

3.2.4. Source Flux

In general, the *Chandra* X-ray source flux is determined as follows:

$$Flux = count\ rate \times ECF, \tag{10}$$

where the *ECF* is the energy conversion factor which converts source count rate to source flux in units of *erg* cm^{-2} *count*$^{-1}$. The *ECF* varies with observation date and CCD pixel position because of the temporal and spatial variations of the ACIS CCD quantum efficiency [9] and the

[8]See http://hea-www.harvard.edu/AstroStat/BEHR/.

[9]See http://asc.harvard.edu/cal/Acis/Cal_prods/qeDeg for the low energy QE degradation.

vignetting effect. The temporal QE variation of the *ECF* can be corrected by generating *ECF*s per observation and per CCD chip. To investigate the spatial variation of the *ECF*, we generated the 0.3-2.5 keV *ECF* map of an ACIS-I observation including ACIS-S S2 and S3 CCD chips. Using the redistribution matrix function (RMF) and ancillary response function (ARF) files and assuming a photon index of $\Gamma_{ph} = 1.7$ and Galactic absorption N_H (Stark et al. 1992) for a given observation, we derive *ECF*s with *Sherpa* [10] in 16×16 grid points with grid size of 32 pixels in each CCD chip (here after ECF_{grid}). In Figure 7, we display the ECF_{grid} contour maps smoothed with a cubic kernel and the left panels of Figure 8 shows the ECF_{grid} as a function of off axis angle in each CCD chip. The *ECF* spatially varies by up to $\sim 25\%$.

To quantitatively see the spatial variation of the QE, we display the ratios of the ECF_{grid} over the $V_{cor} \times ECF_{single}$ as a function of the off axis angle in the right panels of Figure 8, where the ECF_{single} is the *ECF* calculated at a single position (the aim point position for ACIS-I CCDs and at the maximum exposure positions for S2 and S3 chips) and V_{cor} is the vignetting correction factor which is estimated from the exposure map at each grid position. The vignetting corrected ECF_{single} agrees well with ECF_{grid} with the exception of points that are estimated from the CCD edge and bad pixels/columns (*blue squares*). The spatial variation of the QE is shown at large off axis angle (*red triangles*); however, the deviation is less than 5%. Therefore, in this study, we ignore the spatial variation of the QE and correct the vignetting effect to determine the source flux as follows:

$$Flux = count\ rate \times ECF_{single} \times V_{cor}. \tag{11}$$

In Table 3, the ECF_{single} are listed per observation (OBSID) and per CCD chip and calculated at the aim point for I0-I3 of ACIS-I observation and S3 of ACIS-S observation. For the remaining chips, ECF_{single} is calculated at the maximum exposure position. For general usage, we calculated ECF_{single} assuming various photon indices, $\Gamma_{ph} = 1.2$, 1.4, and 1.7 and Galactic absorption N_H from Stark et al. (1992) for that observation. We provide the effective exposure time of each X-ray source corrected for the vignetting effect at the source position (see Table 5 and 6 in §5.1).

3.2.5. Source Flags

All X-ray sources in the ChaMP catalog have been visually inspected to flag those sources with various special issues, as listed in Table 4. Flags 11 to 51, 53, and 54 were determined only by visual examination. The spurious double sources due to PSF effects (flag=15 and 38) are described in detail in §3.1. Since 35 of the 149 ChaMP fields partly overlap on the sky as seen in the 11^{th} column of Table 1, 453 sources were likely observed more than once (flag=52) in these

[10] See http://asc.harvard.edu/sherpa/threads/index.html.

overlapping fields. We identified these 453 source candidates by their positions, matching sources in multiply observed fields within a 95% confidence level positional uncertainty (see equation (12) in §4.2.1). False sources having flags from 11 to 21 and extended X-ray sources (flag=51) including the X-ray jets (flag=54) are not listed in the ChaMP X-ray point source catalogs.

To remove bad pixels/columns, we used the bad pixel file. Additional hot pixels and bad columns were identified by visually inspecting each CCD image and an event histogram as a function of chip x-coordinate (see §3.1 in Paper I for details). The bad pixels are then included in generating an exposure map, which is in turn used to calculate the count rate and flux. Although the source flux may be slightly underestimated when a bad pixel sits at a source location, the effect of a single bad pixel is considerably mitigated by the aspect dither (following a Lissajous pattern over 16x16 $arcsec^2$). Therefore, we flagged sources within which a bad pixel/column exists as flag=31 following visual inspection.

When the source is located at the edge of the CCD chip, where the minimum exposure value in the source region is less than 10% of the maximum exposure value, flag 61 is assigned. The edge flag 61 and overlapping flags from 62 to 68 are automatically flagged by *xapphot*. The overlapping flags correspond to flags $32-35$ in Paper I, with more detailed classes included here: the overlapping class is subclassified as either small or large overlaps (see §3.2.2 for the definition of small and large overlap).

4. ChaMP X-ray Point Source Simulations

4.1. Simulation Procedure

To investigate source reliability and sensitivity, and to establish the empirical equations for positional uncertainty on X-ray sources in the ChaMP fields, we have performed extensive simulations. The technique was based on that of Kim, D.-W. and Fabbiano (2003) and consists of three parts, (1) generating artificial X-ray sources with MARX[11], (2) adding them to the observed image, and (3) detecting these artificial sources with *wavdetect* and extracting source properties with the *xapphot*. We have used every observed ChaMP field for our simulations, rather than blank background sky fields, to investigate the effects of background counts and source confusion.

We used the active I0, I1, I2, and I3 CCD chips for ACIS-I, and I2, I3, S2, and S3 CCD chips for ACIS-S *Chandra* observations, and simulated 1,000 artificial X-ray sources per *Chandra* observation. The number of detected artificial sources in each field depends on the effective exposure

[11]See http://space.mit.edu/CXC/MARX/ and MARX 4.0 Technical Manual.

time and the observed region of the sky with various values of N_H. On average, 11.4% of the 146,178 input artificial X-ray sources are detected in our simulations, for a total $16,676$ artificial X-ray sources in 149 ChaMP fields. The number of detected artificial X-ray sources is 2.3 times the $7,106$ ChaMP sources in the same CCD chips and observations and statistically sufficient to estimate the properties of the ChaMP fields.

The form of the assumed number counts distribution is not critical to determine the detection probability, which is determined by the ratio of input to output numbers at a given flux (Vikhlinin et al. 1995; Kim, D.-W. and Fabbiano 2003). The actual X-ray differential number counts are described by a broken/double power law with faint and bright slopes of ~ -1.5 and ~ -2.5, respectively, (Yang et al. 2004; Basilakos et al. 2005; Chiappetti et al. 2005) in most energy bands; however, the break flux has not been well determined. Therefore, we assumed a cumulative number counts distribution with a single power law and a slope of -1 corresponding to a slope of -2 in the differential number counts, taking the average of the faint and bright slopes from the literature, in the 0.3-8 keV band. The flux of an artificial source was randomly selected from the assumed number counts distribution in a flux range of $5 \times 10^{-16} - 5 \times 10^{-10}$ *erg cm*$^{-2}$ *sec*$^{-1}$, and the MARX generated the artificial sources with a flux range of $8 \times 10^{-17} - 2 \times 10^{-11}$ *erg cm*$^{-2}$ *sec*$^{-1}$ including the Poisson uncertainty of the input source counts. The flux range of the detected artificial sources spans $1 \times 10^{-17} - 2 \times 10^{-11}$ *erg cm*$^{-2}$ *sec*$^{-1}$ which covers the flux range of the actual ChaMP X-ray point sources, $1 \times 10^{-17} - 6 \times 10^{-12}$ *erg cm*$^{-2}$ *sec*$^{-1}$.

We assume a power law spectrum with a photon index of $\Gamma_{ph} = 1.7$, because the ChaMP X-ray points sources with $S/N > 1.5$ have $\Gamma_{ph} = 1.5 \sim 2$ (Kim, D.-W. et al. 2004b; see Figure 20 and 21 in this paper). We note that these sources cover a flux range of $4 \times 10^{-16} \sim 2 \times 10^{-12}$ (0.5-2 keV) and $2 \times 10^{-15} \sim 7 \times 10^{-12}$ (2-8 keV) in *erg cm*$^{-2}$ *sec*$^{-1}$, respectively. Tozzi et al. (2006) performed X-ray spectral analysis for 82 X-ray bright sources in the CDF-S, and they found that the weighted mean value for the slope of the power law spectrum is $< \Gamma_{ph} > \simeq 1.75 \pm 0.02$. The flux range of these bright sources in the CDF-S overlaps with the faint flux end of the ChaMP sources, therefore, we assumed that the faint ChaMP sources ($S/N < 1.5$) also have a photon index of $\Gamma_{ph} \sim 1.7$. We assumed Galactic absorption, N_H, (Stark et al. 1992) for each observation; however, did not include intrinsic absorption in the artificial source spectrum. The spectrum of each X-ray point source was generated using the XSPEC[12] package.

The position of an artificial source was randomly selected on each CCD chip, but it was rejected if the source area at a given random position had an exposure map value with less than 10% of the maximum. This requirement is identical to that in the ChaMP X-ray point source reduction procedure. To avoid over-crowding of the artificial sources, ~ 250 artificial sources per

[12]See http://xspec.gsfc.nasa.gov/.

CCD were divided into several groups to be added into the observed image: while we did not allow the artificial X-ray point sources to overlap one another, we allowed overlap between artificial and real X-ray sources to provide an estimate of source confusion in each observed field. This resulted in ~ 10 (~ 20) simulated images per ACIS-I (ACIS-S) CCD, corresponding to $\sim 10,500$ CCD images (event files) to run through *wavdetect* (*xapphot*). Since $\sim 11.4\%$ of the artificial sources are detected on average we added only ~ 1.5 artificial sources to each simulated image. The net counts of the overlapping artificial sources with real sources were corrected following the overlapping source correction methods described in §3.2.2.

To correct the temporal QE degradation of *Chandra* [13], we used the ECF_{single} for each observation, as described in §3.2.4. However, because of the mis-match between calibration data used in MARX Version 4.0.8 and our analysis, there is a slight difference in the count-flux conversion. Thus we performed a set of test simulations for each CCD chip and observation to correct this mis-match and then renormalized the MARX output by as much as 10% per CCD chip in each observation. After generating and adding artificial X-ray point sources into observed X-ray images, we detected them and extracted their source properties with exactly the same techniques as used in the ChaMP X-ray point source catalog.

4.2. Positional Uncertainty

4.2.1. Empirical Equation of Positional Uncertainty

The positional uncertainty of *Chandra* X-ray sources is a function of source counts, off axis angle, and background counts. To estimate the positional uncertainty in the ChaMP fields, we investigated the offset between input and detected position for the artificial sources. To estimate the positional offsets of artificial sources, first we excluded the observed X-ray sources in simulated images to avoid the confusion caused by a mixture of observed and artificial X-ray sources. Second, we matched the input and detected artificial sources within twice the input source radius. The nearest object in this matching radius was assigned as a matched pair. An object with more than one match was assigned as a pair with the nearest neighbor. We then carefully performed a visual inspection to reject incorrectly matched sources. In the top panel of Figure 9, we display the positional offset of the artificial X-ray sources split into three source count categories as a function of off axis angle. Since the source position is determined by *wavdetect*, we used the source counts measured by *wavdetect* rather than by our aperture photometry *xapphot*. It appears that the positional offsets exponentially increase with off axis angle and decrease as the source count increases

[13] See CXC Memo on 2002 July 29 (http://cxc.harvard.edu/cal/Acis/Cal_prods/qeDeg/index.html).

with a power law form.

Applying the exponential function and the power law, we derive empirical equations for the positional uncertainty of ChaMP X-ray point sources. A 95% confidence level, these are:

$$logPU = \begin{cases} 0.1145 \times OAA - 0.4958 \times logC + 0.1932, & 0.0000 < logC \leq 2.1393 \\ \\ 0.0968 \times OAA - 0.2064 \times logC - 0.4260, & 2.1393 < logC \leq 3.3000 \end{cases} \quad (12)$$

A 90% confidence level:

$$logPU = \begin{cases} 0.1142 \times OAA - 0.4839 \times logC + 0.0499, & 0.0000 < logC \leq 2.1336 \\ \\ 0.0989 \times OAA - 0.2027 \times logC - 0.5500, & 2.1336 < logC \leq 3.3000 \end{cases} \quad (13)$$

A 68% confidence level:

$$logPU = \begin{cases} 0.1137 \times OAA - 0.4600 \times logC - 0.2398, & 0.0000 < logC \leq 2.1227 \\ \\ 0.1031 \times OAA - 0.1945 \times logC - 0.8034, & 2.1227 < logC \leq 3.3000. \end{cases} \quad (14)$$

Here positional uncertainty, PU, is in arcseconds, and off axis angle, OAA, is in arcminutes. Source counts, C, are as extracted by *wavdetct*. The above equations are valid for the ChaMP X-ray point sources with an off axis angle, $OAA \lesssim 15'$ and source counts, $logC \lesssim 3.3$. For ChaMP X-ray point sources located at off axis angle larger than $15'$, the positional uncertainties were assigned to be $60''$. In the bottom panel of Figure 9, using equation (12)-(14), we display the positional uncertainties as a function of off axis angle for three different source counts. Figure 10 shows the number distributions of positional uncertainty of the ChaMP X-ray point sources from equation (12)-(14). For 68%, 90%, and 95% confidence level positional uncertainty distributions, the medians are $0.7 \pm 0.45''$, $1.3 \pm 0.8''$, and $1.8 \pm 1.1''$, respectively.

We also investigated the dependence of the positional uncertainties on the background counts; however, it is negligible in the ChaMP sample. Since we excluded high background regions such as the Galactic plane, the background counts per unit pixel of ChaMP X-ray sources are only $3 \times 10^{-4} \sim 9 \times 10^{-2}$ *counts pixel*$^{-1}$ and there are no significant background fluctuations in these fields. However, the background effect should be carefully considered to estimate the positional uncertainties of X-ray sources when the background fluctuations are severe, such as in the Galactic plane.

4.2.2. Astrometry

To ensure accurate absolute positions for the ChaMP X-ray point sources, we apply the standard *Chandra* aspect offsets [14]. For the ChaMP data set, the magnitude of the mean aspect offset correction is $\sim 0.5''$, and the maximum is $\sim 2.7''$ (for OBSID=521). To further check the absolute positional accuracy of our ChaMP X-ray point sources, we matched the ChaMP X-ray sources with the SDSS-DR3 [15] (hereafter SDSS) optical objects, for which the absolute positional uncertainty is less than $0.5''$. 60 of the 149 ChaMP fields overlap with the SDSS sky regions. Using the 95% confidence level positional uncertainty equation (equation (12) in §4.2.1), over $2'' < radius < 12.33''$, we searched the SDSS optical candidates of the ChaMP X-ray sources. The minimum searching radius is large enough not to miss probable partners, and the maximum searching radius corresponds to half the mean separation of the SDSS objects, thereby, reducing the number of randomly matched objects.

Some X-ray sources have more than one SDSS candidate counterpart. To decide the most appropriate SDSS counterpart for these X-ray sources, we consider their X-ray and optical properties in addition to their offsets. The X-ray sources have a typical relation between X-ray flux and optical magnitude (Manners et al. 2003; Green et al. 2004). We applied the normalized distance D_n between ChaMP and SDSS sources with positional uncertainty PU and X-ray to optical flux ratio f_x/f_r as follows:

$$D_n = D/PU, \tag{15}$$

$$log(f_x/f_r) = Log(f_x) + 5.41 + 0.4 \times m_r, \tag{16}$$

where D is the distance between the ChaMP and the SDSS counterpart, f_x is the X-ray flux in the Sc band, and m_r is the visual magnitude in the r band. First, for objects with one counterpart and with $OAA < 6'$, we calculated the average of D_n and $log(f_x/f_r)$. Second, for objects with multiple counterparts, we calculated the standard deviations of D_n and $log(f_x/f_r)$ relative to the average D_n and $log(f_x/f_r)$, and introduced a likelihood as follows:

$$L = \sqrt{\Delta^2_{log(f_x/f_r)} + \Delta^2_{D_n}}, \tag{17}$$

where $\Delta_x \equiv (x - \bar{x})/\sigma_x$. Finally, we chose the counterpart with the lowest L among the multiple counterparts as the most appropriate counterpart.

We also calculated the average $log(f_x/f_r)$ as a function of optical color and optical size. We classified the SDSS sources into four groups and recalculated the average of $log(f_x/f_r)$ for

[14] See http://cxc.harvard.edu/cal/ASPECT/.

[15] See http://www.sdss.org/dr3/.

each group. The four groups are resolved (galaxies), unresolved with $u-g<0.6$ (UVX QSOs), unresolved with $g-r>1.2$ (M stars), and all other unresolved. We then redetermined the SDSS counterpart for each X-ray source, after repeating the above procedures. Except for 20 of $\sim 1,600$ pairs, the matching results were same. To confirm the matching results, we performed a visual inspection for all matched objects. In the top panel of Figure 11, the positional offsets between the ChaMP and the SDSS source are plotted as a function of off axis angle. The positional offset increases exponentially with off axis angle. The bottom panel shows the number distribution of the positional offsets between the matched ChaMP and SDSS sources. The median positional offset of confirmed ~ 900 matched sources is $0.7\pm0.4''$.

4.3. ChaMP Source Reliability

To understand the source reliability of the ChaMP point source catalog, we have investigated the detection probability, count recovery rate, false source rate, and flux limit of each ChaMP field using the simulation results.

4.3.1. Detection Probability

The detection probability is determined by the number ratio of detected artificial sources to input artificial sources. Since the sensitivity of the *Chandra* CCD chip varies spatially, the detection probability is a function of off axis angle as well as a function of source counts. Figure 12 shows the detection probability of a source as a function of the B band counts depending on off axis angle. The detection probability decreases as the source counts decrease, and as the off axis angle increases because the sensitivity of the *Chandra* CCD chip decreases as the off axis angle increases. Sources with counts >30 and off axis angle $<5'$ are detected with greater than 95% probability. We note that the detection probability as a function of flux may vary with source spectral shape if the source is quite different from our assumed spectral shape ($\Gamma_{ph}=1.7$).

4.3.2. False Source Rate

We also investigated the probability of false sources in the ChaMP catalog. With simulated images, we found that false sources are $\sim 1\%$ of the total detected sources. 80% of these spurious sources have counts less than ~ 30. Figure 13 shows the false source detection rate as a function of the B band source counts (*top*) and off axis angle (*bottom*). The dashed lines indicate the best

linear least square fitting results:

$$False\ Source\ Rate(C) = -0.05(\pm 0.00)C + 1.92(\pm 0.04), \quad (18)$$

$$False\ Source\ Rate(OAA) = 0.15(\pm 0.02)OAA - 0.01(\pm 0.18), \quad (19)$$

where *OAA* is in units of arcminutes and *C* is the source counts extracted by *wavdetect*. The false source detection rate increases with decreasing source counts and increasing off axis angle. To derive equation (18), we used false sources with $C < 40$ and for equation (19), we used all false sources.

4.3.3. Counts Recovery Rate

To confirm the quality of our photometry, we investigated the count recovery rate defined by the ratio of the difference between input counts and output counts ($C_{out} - C_{in}$) to input counts (C_{in}). First, we compared the photometry results from *xapphot* (aperture photometry) and *wavdetect*. The top panel of Figure 14 shows the count recovery rate using *xapphot* (*red circles*) and using *wavdetect* (*blue squares*) as a function of input counts. The count recovery rate of *xapphot* is $96 \pm 1\%$, regardless of input counts. This is very close to that expected, given that our choice of the source extraction radius corresponds to the 95% encircled energy. We note that our count recovery rate agrees with that of Tozzi et al. (2001) in which they applied aperture photometry to the CDF-S sources with the source extraction region defined as a circle of radius $R_s = 2.4 \times FWHM$, where $FWHM$ is modeled from the PSF. While the *wavdetect*-determined count recovery rate is $96 \pm 2\%$ for bright sources (*counts* > 50), it underestimates the counts for sources with counts < 70. For example, *wavdetect* recovers $87 \pm 2\%$ for sources with input counts $\lesssim 50$. This is primarily because *wavdetect* uses a smaller source extraction radius for fainter sources.

Second, we have investigated the count recovery rate of *xapphot* depending on the off axis angle in the bottom panel of Figure 14. The *xapphot* recovers source counts well regardless of the off axis angle; however, the statistical errors of the count recovery rate increase as the off axis angle increases, since the background fluctuations affect off-axis sources more severely than on-axis sources due to the larger source and background extraction regions.

4.3.4. Flux Limit and Exposure Time

Using four CCD chips (I0, I1, I2, and I3 for ACIS-I observations, and I2, I3, S2, and S3 for ACIS-S observations) per ChaMP field, we derived the relation between flux limit and exposure time of the observation in each energy band. The detected artificial sources with $S/N > 2.0$ have

been selected in each CCD chip, and their minimum flux is defined as the flux limit of that CCD chip. Figure 15 shows the flux limits of detected artificial sources in the ChaMP fields as a function of the exposure time. The best linear least square fit results of the relation between flux limits and exposure times in each energy band are as follows:

$$logF_{limit,B} = -1.04(\pm 0.02) \times logET - 12.87(\pm 0.03), \quad (20)$$

$$logF_{limit,S} = -1.06(\pm 0.02) \times logET - 13.10(\pm 0.02), \quad (21)$$

$$logF_{limit,H} = -1.23(\pm 0.03) \times logET - 12.08(\pm 0.04), \quad (22)$$

$$logF_{limit,Bc} = -1.06(\pm 0.02) \times logET - 12.81(\pm 0.02), \quad (23)$$

$$logF_{limit,Sc} = -1.08(\pm 0.02) \times logET - 13.17(\pm 0.02), \quad (24)$$

$$logF_{limit,Hc} = -1.22(\pm 0.03) \times logET - 12.15(\pm 0.03), \quad (25)$$

where ET is the net exposure time of each CCD chip in units of *ksec* after excluding any background flares (see Paper I) and the flux is estimated assuming a photon index of $\Gamma_{ph} = 1.7$. The scatter of the relation is caused by the varying sensitivity and detection probability of each CCD chip and OBSID. These equations give us a representative for the flux limit of X-ray sources depending on their exposure time in the B, S, H, Bc, Sc, and Hc bands in the ChaMP fields.

5. ChaMP X-ray Point Source Catalogs

5.1. Catalogs

We found 7365 X-ray point sources in 149 ChaMP fields, after excluding false sources (flag=11-21) and sources located close to the CCD chip edges (flag=61) (see Table 4 for flag definitions). The 102 target point sources (flag=53) are included in the catalog for completeness. We note that, for scientific analysis, target sources need to be carefully handled depending on their own scientific goals because they are not random sources. For example, we excluded the target sources to determine the X-ray point source number counts (Kim, D.-W. et al. 2004b; Kim, M. et al. 2006).

Since 35 of the 149 ChaMP fields partly overlap on the sky as seen in the 11^{th} column of Table 1, there are sources observed more than once in these overlapping fields. For simplicity and flexible usage, we present the sources in the overlapping fields in separate tables: e.g., for the X-ray number counts research, we used only the main ChaMP catalog to derive the sky coverage avoiding complex overlapping fields (Kim, M. et al. 2006). In the main ChaMP tables (Table 5, Table 8, and Table 10), we present all sources in fields observed once and those in the overlapping fields with the longest exposure time. In the supplementary ChaMP tables (Table 6, Table 9, and Table 11), we

present the sources in the overlapping fields with shorter exposure times. The main ChaMP tables list 6,512 X-ray point sources in 130 ChaMP fields and the supplementary ChaMP tables list 853 sources in 19 ChaMP fields. Tables 5 and 6 contain the source position, positional uncertainty, off axis angle, source radius, effective exposure time, and flag. Tables 8 and 9 give the photometry of the X-ray point sources in eight X-ray energy bands. Tables 10 and 11 list the hardness ratio and colors such as C21 and C32 of the X-ray point sources. In Table 7, we list the same source candidates in the overlapping fields (453 pairs/triples of 926 sources) with their observation date, source counts, count rates, and positional uncertainties. We note that these candidates are identified only by their positions, matching sources in the overlapping fields within a 95% confidence level positional uncertainty (see equation (12) in §4.2.1). These sources also have a source flag of 52 (see §3.2.5). Table 7 allows us to investigate the variability of X-ray source brightness.

The ChaMP source name is given by its right ascension and declination. We note that the position of some sources in Paper I and this paper could be slightly different because the position refinement process was applied to sources with an off axis angle of $> 400''$ in Paper I whereas in this paper it was applied to all sources. For the sources which were published in previous papers (Kim, D.-W. et al. 2004a; Green et al. 2004; Silverman et al. 2005a,b), we use the published name, even if the source position has been changed. The full versions of the tables are available in the electronic version of this paper and also on the ChaMP web site[16], while we only present a sample of each table in this paper.

5.2. The ChaMP X-ray Point Sources

To understand the properties of the ChaMP X-ray point sources, we investigated their statistical characteristics. After eliminating source duplications in the main and supplementary ChaMP catalogs, the ChaMP X-ray point source catalog contains 6,889 unique sources. To eliminate the source duplication, we selected a source having the smallest positional uncertainty among the same source candidates in Table 7: since the positional uncertainty is a function of off axis angle and source counts (see §4.2.1), this criterion automatically selects a higher quality source. With these individual sources, we display the distributions of source count, flux, off axis angle, and hardness ratio and colors of these individual sources with their median values in Figure 16 through Figure 19, respectively. Sources with signal to noise ratio, $S/N > 2.0$ are displayed with shaded histograms. Figures 20 and 21 show the X-ray color-color diagrams of the ChaMP X-ray point sources in four CCD chips observed with ACIS-I and ACIS-S, respectively. The grid in the X-ray color-color diagram indicates the predicted locations of sources at redshift $z = 0$ with various pho-

[16]See http://hea-www.cfa.harvard.edu/CHAMP.

ton indices ($0 \leq \Gamma_{ph} \leq 4$) and neutral hydrogen column densities ($10^{20} \leq N_H \leq 10^{22}$). Sources with $S/N > 1.5$ (*open circles*) and sources with $S/N > 2.0$ (*red closed circles*) are plotted. Most sources have absorption in the range $10^{20} \lesssim N_H \lesssim 10^{21}$ cm^{-2} and the photon index, $1 \lesssim \Gamma_{ph} \lesssim 2.5$. We note that the absorbed sources ($N_H > 10^{21}$ cm^{-2}) in the ChaMP sample are not statistically significant ($S/N < 1.5$ in at least one energy band) and so are not plotted in Figure 20 and 21.

In Table 12, we summarize the statistical properties of the ChaMP X-ray point sources: number of sources, minimum, maximum, median, and mean for the source counts, source fluxes, effective exposure times, off axis angle, hardness ratio HR, color C21, and color C32. We define the properties of typical ChaMP X-ray point source as the median values of these quantities for sources with $S/N > 2.0$. The typical source fluxes are 4.3×10^{-15} *erg* cm^{-2} sec^{-1} (0.5-2 keV) and 11.1×10^{-15} *erg* cm^{-2} sec^{-1} (2-8 keV), respectively. The typical flux ranges are $3.7 \times 10^{-16} \sim 2.5 \times 10^{-11}$ *erg* cm^{-2} sec^{-1} (0.5-2 keV) and $1.7 \times 10^{-15} \sim 6.7 \times 10^{-11}$ *erg* cm^{-2} sec^{-1} (2-8 keV), respectively. The flux ranges of ChaMP X-ray sources cover the flux gap between the *Chandra* Deep Fields and previous surveys such as *ASCA* and *ROSAT*, and fully cover the flux range around the break in the X-ray number counts (Kim, M. et al. 2006).

Thanks to the ChaMP's medium depth ($9.4 \times 10^{-16} \sim 5.9 \times 10^{-11}$ *erg* cm^{-2} sec^{-1} in the 0.5-8 keV), wide sky coverage area (~ 10 deg^2), and large number of sources ($\sim 6,800$), we can investigate populations and evolution models of cosmic X-ray sources with small statistical errors. The ChaMP is a serendipitous survey, therefore it is suitable for investigating the field-to-field variations of X-ray sources. In later ChaMP papers, we will provide number counts of X-ray point sources and their contributions to the CXRB, spatial angular correlations, X-ray color-color analysis, and optical/IR/radio properties of X-ray sources. Also, we will extend our study of X-ray galaxies (Kim, D.-W. et al. 2006) and X-ray galaxy clusters (Barkhouse et al. 2006) in ChaMP fields.

6. Summary and Conclusions

1. We present the full ChaMP X-ray point source catalog. The main catalog contains 6,512 sources from 130 ChaMP fields and the supplementary catalog contains 853 sources from 19 ChaMP fields which are partly overlapping in their field of view with those in the main catalog. After eliminating duplications, our catalogs contain $\sim 6,800$ individual point sources, in a sky area of ~ 10 deg^2.

2. The ChaMP X-ray sources are uniformly reduced with the ChaMP XPIPE pipeline and carefully confirmed by visual inspections. Photometry in eight X-ray energy bands, hardness ratio, and X-ray colors of ChaMP X-ray point sources are provided. To calculate the flux of ChaMP

X-ray point sources, we also provide the energy conversion factors (*ECF*s) for each CCD chip and observation for photon indices, $\Gamma_{ph} = 1.2$, 1.4, and 1.7 and Galactic absorption, N_H and the vignetting corrected effective exposure times.

3. To understand the sensitivity and reliability of ChaMP X-ray point sources, we have performed extensive simulations. The detection probability of ChaMP sources is greater than 95% for source counts of $\gtrsim 30$ and off axis angle of $< 5'$. The count recovery rate is $96 \pm 1\%$ regardless of source counts. *wavdetect* tends to underestimate the net counts for faint sources (87% for $\lesssim 50$ counts). The false source detection probability is $\sim 1\%$ of the total detected sources and $\sim 80\%$ of these have source counts of $\lesssim 30$.

4. Empirical equations for the positional uncertainties were derived from the ChaMP simulations. The positional uncertainty in ChaMP fields exponentially increases with off axis angle and decreases as the source counts increase with a power law form. Background fluctuations do not affect the positional uncertainty in our ChaMP sample. The 68%, 90%, and 95% confidence levels of equations for the positional uncertainties are provided.

5. The absolute positional accuracy of the ChaMP X-ray sources is $0.7 \pm 0.4''$, estimated by matching with *SDSS* optical sources.

6. The typical ChaMP X-ray point source in the 0.5-2 keV band has counts of 24.3, flux of 4.3×10^{-15} *erg cm*$^{-2}$ *sec*$^{-1}$, effective exposure time of 37.6 *ksec* and off axis angle of $6.3'$. In the 2-8 keV band, the typical source has counts of 18.9, flux of 11.1×10^{-15} *erg cm*$^{-2}$ *sec*$^{-1}$, effective exposure time of 41.7 *ksec* and off axis angle of $6.24'$.

7. The hardness ratio and X-ray colors were calculated with a Bayesian approach which models the detected counts as a Poisson distribution. The typical hardness ratio of the ChaMP X-ray source is -0.35, and X-ray colors C21 and C32 are -0.29 and 0.36, respectively.

8. The flux levels (in *erg cm*$^{-2}$ *sec*$^{-1}$) of sources are $9.4 \times 10^{-16} \sim 5.9 \times 10^{-11}$ (0.5-8 keV), $3.7 \times 10^{-16} \sim 2.5 \times 10^{-11}$ (0.5-2 keV), and $1.7 \times 10^{-15} \sim 6.7 \times 10^{-11}$ (2-8 keV), respectively. In the X-ray color-color diagram, typical ChaMP sources are located within absorption range: $10^{20} \lesssim N_H \lesssim 10^{21}$ *cm*$^{-2}$ and within photon index range: $1 \lesssim \Gamma_{ph} \lesssim 2.5$.

We gratefully acknowledge support for this project under NASA CXC archival research grant AR4-5017X and AR6-7020X . PJG, DWK, HT, and BJW also acknowledge support through NASA Contract NAS8-03060 (CXC). MGL is in part supported by the KOSEF grant (R01-2004-000-10490-0).

Facility: CXO (ACIS)

REFERENCES

Alexander, D. M., Bauer, F. E., Brandt, W. N., Schneider, D. P., Hornschemeier, A. E., Vignali, C., Barger, A. J., Broos, P. S., Cowie, L. L., Garmire, G. P., Townsley, L. K., Bautz, M. W., Chartas, G., Sargent, W. L. W. 2003, AJ, 126, 539

Barger, A. J., Cowie, L. L., Capak, P., Alexander, D. M., Bauer, F. E., Fernandez, E., Brandt, W. N., Garmire, G. P., Hornschemeier, A. E. 2003, AJ, 126, 632

Barkhouse, W. A., Green, P. J., Vikhlinin, A., Kim, D.-W., Perley, D., Cameron, R., Silverman, J., Mossman, A., Burenin, R., Jannuzi, B. T., Kim, M., Smith, M. G., Smith, R. C., Tananbaum, H., & Wilkes, B. J. 2006, astro-ph/0603521, accepted to ApJ

Basilakos, S., Plionis, M., Georgakakis, A., & Georgantopoulos, I. 2005, MNRAS, 356, 183

Bauer, F. E., Alexander, D. M., Brandt, W. N., Schneider, D. P., Treister, E., Hornschemeier, A. E., Garmire, G. P. 2004, AJ, 128, 2048

Brandt, W. N., Alexander, D. M., Hornschemeier, A. E., Garmire, G. P., Schneider, D. P., Barger, A. J., Bauer, F. E., Broos, P. S., Cowie, L. L., Townsley, L. K., Burrows, D. N., Chartas, G., Feigelson, E. D., Griffiths, R. E., Nousek, J. A., Sargent, W. L. W. 2001, AJ, 122, 2810

Brandt, W. N., & Hasinger, G., 2005, ARA&A, 43, 827

Chiappetti, L., Tajer, M., Trinchieri, G., Maccagni, D., Maraschi, L., Paioro, L., Pierre, M., Surdej, J., Garcet, O., Gosset, E., Le Fevre, O., Bertin, E., McCracken, H. J., Mellier, Y., Foucaud, S., Radovich, M., Ripepi, V., Arnaboldi, M., 2005, A&A, 439, 413

Gehrels, N. 1986, ApJ, 303, 336

Giacconi, R., Gursky, H., Paolini, F. R., Rossi, B. B. 1962, *Phys. Rev. Lett.* 9, 439

Giacconi, R., Rosati, P., Tozzi, P., Nonino, M., Hasinger, G., Norman, C., Bergeron, J., Borgani, S., Gilli, R., Gilmozzi, R., Zheng, W. ApJ, 551, 624

Green, P. J., Silverman, J. D., Cameron, R. A., Kim, D.-W., Wilkes, B. J., Barkhouse, W. A., LaCluyz, A., Morris, D., Mossman, A., Ghosh, H., Grimes, J. P., Jannuzi, B. T., Tananbaum, H., Aldcroft, T. L., Baldwin, J. A., Chaffee, F. H., Dey, A., Dosaj, A., Evans, N. R., Fan, X., Foltz, C., Gaetz, T., Hooper, E. J., Kashyap, V. L., Mathur, S., McGarry, M. B., Romero-Colmenero, E., Smith, M. G., Smith, P. S., Smith, R. C., Torres, G., Vikhlinin, A., Wik, D. R. 2004, ApJS, 150, 43

Freeman, P. E., Kashyap, V., Rosner, R., & Lamb, D.Q. 2002, ApJS, 138, 185

Hasinger, G., Burg, R., Giacconi, R., Hartner, G., Schmidt, M., Trumper, J., & Zamorani, G. 1993, A&A, 275, 1

Kim, D.-W., & Fabbiano, G. 2003, ApJ, 586, 826

Kim, D.-W., Cameron, R. A., Drake, J. J., Evans, N. R., Freeman, P., Gaetz, T. J., Ghosh, H., Green, P. J., Harnden, F. R., Jr., Karovska, M., Kashyap, V., Maksym, P. W., Ratzlaff, P. W., Schlegel, E. M., Silverman, J. D., Tananbaum, H. D., Vikhlinin, A. A., Wilkes, B. J., & Grimes, J. P. 2004a, ApJS, 150, 19 (Paper I)

Kim, D.-W., Wilkes, B. J., Green, P. J., Cameron, R. A., Drake, J. J., Evans, N. R., Freeman, P., Gaetz, T. J., Ghosh, H., Harnden, F. R., Jr., Karovska, M., Kashyap, V., Maksym, P. W., Ratzlaff, P. W., Schlegel, E. M., Silverman, J. D., Tananbaum, H. D., & Vikhlinin, A. A. 2004b, ApJ, 600, 59

Kim, D.-W., Barkhouse, W. A., Green, P. J., Kim, M., Mossman, A., Schlegel, E., Silverman, J. D., Aldcroft, T., Anderson, C., Kashyap, V., Tananbaum, H., & Wilkes, B. J. 2006, accepted to ApJ

Kim, E. et al. 2006, in preparation

Kim, M. et al. 2006, submitted to ApJ

Manners, J. C., Johnson, O., Almaini, O., Willott, C. J., Gonzalez-Solares, E., Lawrence, A., Mann, R. G., Perez-Fournon, I., Dunlop, J. S., McMahon, R. G., Oliver, S. J., Rowan-Robinson, M., & Serjeant, S. 2003, MNRAS, 343, 293

Martini, P., Kelson, D. D., Kim, E., Mulchaey, J. S., Athey, A. A. 2006, astro-ph/0602496, accepted to ApJ

Moretti, A., Campana, S., Lazzati, D., & Tagliaferri, G. 2003, ApJ, 588, 696

Murray, S. S., Kenter, A., Forman, W. R., Jones, C., Green, P. J., Kochanek, C. S., Vikhlinin, A., Fabricant, D., Fazio, G., Brand, K., Brown, M. J. I., Dey, A., Jannuzi, B. T., Najita, J., McNamara, B., Shields, J., Rieke, M., 2005, ApJS, 161, 1

Park, T., Kashyap, V. L., Siemiginowska, A., van Dyk, D. A., Zezas, A., Heinke, C., Wargelin, B. J. 2006, astro-ph/0606247, accepted to ApJ

Pierre, M., Valtchanov, I., Altieri, B., Andreon, S., Bolzonella, M., Bremer, M., Disseau, L., Dos Santos, S., Gandhi, P., Jean, C., Pacaud, F., Read, A., Refregier, A., Willis, J., Adami, C., Alloin, D., Birkinshaw, M., Chiappetti, L., Cohen, A., Detal, A., Duc, P.-A., Gosset, E., Hjorth, J., Jones, L., LeFevre, O., Lonsdale, C., Maccagni, D., Mazure, A., McBreen, B.,

McCracken, H., Mellier, Y., Ponman, T., Quintana, H., Rottgering, H., Smette, A., Surdej, J., Starck, J.-L., Vigroux, L., White, S. 2004, Journal of Cosmology and Astroparticle Physics, 9, 11

Rosati, P., Tozzi, P., Giacconi, R., Gilli, R., Hasinger, G., Kewley, L., Mainieri, V., Nonino, M., Norman, C., Szokoly, G., Wang, J. X., Zirm, A., Bergeron, J., Borgani, S., Gilmozzi, R., Grogin, N., Koekemoer, A., Schreier, E., Zheng, W. 2002, ApJ, 566, 667

Silverman, J. D., Green, P. J., Barkhouse, W. A., Cameron, R. A., Foltz, C., Jannuzi, B. T., Kim, D.-W., Kim, M., Mossman, A., Tananbaum, H., Wilkes, B. J., Smith, M. G., Smith, R. C., Smith, P. S. 2005, ApJ, 624, 630

Silverman, J., Green, P., Barkhouse, W., Kim, D.-W., Aldcroft, T., Cameron, R., Wilkes, B., Mossman, A., Ghosh, H., Tananbaum, H., Smith, M., Smith, R., Smith, P., Foltz, C., Wik, D., Jannuzi, B. 2005, ApJ, 618, 123

Stark, A. A. et al. 1992, ApJS, 79,77

Tozzi, P., Rosati, P., Nonino, M., Bergeron, J., Borgani, S., Gilli, R., Gilmozzi, R., Hasinger, G., Grogin, N., Kewley, L., Koekemoer, A., Norman, C., Schreier, E., Szokoly, G., Wang, J. X., Zheng, W., Zirm, A., Giacconi, R. 2001, ApJ, 562, 42

Tozzi, P., Gilli, R., Mainieri, V., Norman, C., Risaliti, G., Rosati, P., Bergeron, J., Borgani, S., Giacconi, R., Hasinger, G., Nonino, M., Streblyanska, A., Szokoly, G., Wang, J. X., & Zheng, W. 2006, A&A, 451, 457

van Dyk, D. A., Park, T., Kashyap, V. L., & Zezas, A. 2004, American Astronomical Society, HEAD meeting, 8, 16.27, ”Computing Hardness Ratios with Poissonian Errors”

Vikhlinin, A., Forman, W., Jones, C., & Murray, S. S. 1995, ApJ, 451, 542

Worsley, M. A., Fabian, A. C., Barcons, X., Mateos, S., Hasinger, G., & Brunner, H. 2004, MNRAS, 352, L28

Worsley, M. A., Fabian, A. C., Bauer, F. E., Alexander, D. M., Hasinger, G., Mateos, S., Brunner, H., Brandt, W. N., & Schneider, D. P., 2005, MNRAS, 357, 1281

Yang, Y., Mushotzky, R. F., Steffan, A. T., Barger, A. J., & Cowie, L. L. 2004, AJ, 128, 1501

Table 1. List of ChaMP Fields

Obs. ID (1)	Sequence Number (2)	Target Name (3)	R.A. (J2000) (4)	Decl. (J2000) (5)	N_H ($10^{20} cm^{-2}$) (6)	Obs. Date (7)	Exposure (*ksec*) (8)	Aim Point Detector (9)	CCD Used (10)	Multi ID (11)	Paper I Used (12)
520	800028	MS 0015.9+1609	00 : 18 : 32.7	+16 : 30 : 04.0	4.06	2000 Aug 18	60.99	ACIS-I	01236		Y
1595	700211	3C9	00 : 20 : 24.0	+15 : 42 : 09.1	4.16	2001 Jun 10	13.27	ACIS-S	235678		
2098	700288	LBQS 0019+0107	00 : 22 : 28.0	+01 : 23 : 37.6	2.92	2001 Dec 08	4.70	ACIS-S	235678		
2099	700289	LBQS 0021-0213	00 : 24 : 10.6	−01 : 56 : 12.1	2.95	2001 Aug 20	6.65	ACIS-S	235678		
929	800105	CL 0024+17	00 : 26 : 31.8	+17 : 10 : 57.4	4.19	2000 Sep 06	36.72	ACIS-S	245678		
2100	700290	LBQS 0025-0151	00 : 27 : 34.6	−01 : 35 : 25.9	2.81	2001 Oct 31	4.40	ACIS-S	235678		
2101	700291	LBQS 0029+0017	00 : 31 : 35.5	+00 : 34 : 58.7	2.41	2001 Jun 20	3.82	ACIS-S	235678		
2242	900069	GSGP4X:048	00 : 57 : 17.9	−27 : 22 : 23.8	1.69	2000 Dec 18	6.66	ACIS-S	235678	12	Y
2243	900070	GSGP4X:057	00 : 57 : 28.2	−27 : 44 : 02.8	1.76	2000 Oct 30	8.75	ACIS-S	235678	13	
2244	900071	GSGP4X:069	00 : 57 : 38.9	−27 : 33 : 30.0	1.62	2000 Oct 30	6.86	ACIS-S	235678	12	Y
2245	900072	GSGP4X:082	00 : 57 : 51.9	−27 : 23 : 30.6	1.43	2000 Oct 30	6.52	ACIS-S	235678	12	Y
2246	900073	GSGP4X:091	00 : 58 : 01.5	−27 : 53 : 49.2	1.62	2001 Jan 13	8.49	ACIS-S	235678	13	
2247	900074	GSGP4X:109	00 : 58 : 26.4	−27 : 29 : 51.0	1.37	2000 Nov 07	10.88	ACIS-S	235678	12	Y
2248	900075	GSGP4X:114	00 : 58 : 38.3	−27 : 49 : 17.5	1.55	2000 Nov 08	10.11	ACIS-S	235678	13	Y
2179	700369	PSS 0059+0003	00 : 59 : 23.0	+00 : 03 : 35.9	3.01	2001 Sep 18	2.58	ACIS-S	235678		
521	800029	CL 0107+31	01 : 02 : 05.2	+31 : 47 : 54.7	5.49	1999 Oct 23	46.87	ACIS-I	01237		Y
813	700118	Q0059-2735	01 : 02 : 15.4	−27 : 19 : 15.2	1.97	2000 May 15	4.29	ACIS-S	235678		
2180	700370	BRI 0103+0032	01 : 06 : 19.3	+00 : 48 : 57.7	3.15	2001 Sep 18	3.61	ACIS-S	235678		
342	700014	NGC 526A	01 : 23 : 53.6	−35 : 04 : 33.5	2.09	2000 Feb 07	5.78	ACIS-S	235678		Y
2129	700319	3C 47	01 : 36 : 24.4	+20 : 56 : 49.1	5.71	2001 Jan 16	39.89	ACIS-S	235678		
814	700119	Q0135-4001	01 : 37 : 13.1	−39 : 46 : 46.2	1.97	2000 Jan 02	3.82	ACIS-S	23678		
2181	700371	SDSS0150+0041	01 : 50 : 48.9	+00 : 42 : 01.3	2.82	2001 Aug 31	2.74	ACIS-S	235678		
913	800089	CL J0152.7-1357	01 : 52 : 49.3	−13 : 56 : 19.1	1.61	2000 Sep 08	34.81	ACIS-I	012367		Y
2223	800162	NGC 741 GROUP	01 : 56 : 22.9	+05 : 35 : 60.0	4.43	2001 Jan 28	24.72	ACIS-S	235678		
2081	700271	SDSS021102-000910	02 : 11 : 03.4	−00 : 09 : 47.2	2.72	2001 Jan 09	3.80	ACIS-S	235678		
1642	700258	HE0230-2130	02 : 32 : 35.7	−21 : 17 : 12.2	2.27	2000 Oct 14	8.35	ACIS-S	123678		Y
135	700120	Q0254-334	02 : 56 : 46.8	−33 : 16 : 08.8	2.26	2000 Feb 15	0.94	ACIS-S	235678	1	
815	700120	Q0254-334	02 : 56 : 48.4	−33 : 16 : 05.3	2.26	2000 Jan 02	1.16	ACIS-S	23678	1	
525	800033	MS 0302.7+1658	03 : 05 : 28.3	+17 : 13 : 20.6	10.94	2000 Oct 03	8.95	ACIS-I	01236		Y
796	600099	SBS 0335-052	03 : 37 : 44.5	−05 : 02 : 19.4	4.98	2000 Sep 07	46.81	ACIS-I	012367		Y
624	200049	LP 944-20	03 : 39 : 36.8	−35 : 26 : 21.2	1.44	1999 Dec 15	40.94	ACIS-S	23678		Y
2182	700372	BRI 0401-1711	04 : 03 : 56.1	−17 : 02 : 49.4	2.30	2001 Aug 03	3.35	ACIS-S	235678		
418	700090	MITG J0414+0534	04 : 14 : 37.0	+05 : 34 : 10.6	11.31	2000 Apr 02	7.34	ACIS-S	123678	3	
1628	700244	MITG J0414+0534	04 : 14 : 37.5	+05 : 34 : 03.8	11.31	2001 Feb 05	8.72	ACIS-S	123678	3	
421	700093	MITG J0414+0534	04 : 14 : 37.7	+05 : 35 : 20.2	11.31	2000 Aug 16	6.56	ACIS-S	123678	3	
936	900008	AX J0431-0526	04 : 31 : 43.6	−05 : 26 : 08.1	4.89	2000 Oct 03	3.81	ACIS-I	012367		
902	800078	MS 0451.6-0305	04 : 54 : 12.9	−02 : 58 : 52.4	5.18	2000 Oct 08	41.53	ACIS-S	235678		Y
346	700018	PICTOR A	05 : 19 : 45.6	−45 : 46 : 29.3	4.12	2000 Jan 18	25.44	ACIS-S	23678		Y
914	800090	CL J0542.8-4100	05 : 42 : 49.0	−40 : 58 : 48.4	3.59	2000 Jul 26	48.72	ACIS-I	01236		Y
1602	700218	Q0615+820	06 : 26 : 01.5	+82 : 03 : 00.9	5.27	2001 Oct 18	43.08	ACIS-S	235678		
377	700049	B2 0738+313	07 : 41 : 11.9	+31 : 12 : 35.8	4.18	2000 Oct 10	26.91	ACIS-S	235678		Y
838	700143	3C 200	08 : 27 : 26.8	+29 : 19 : 19.9	3.69	2000 Oct 06	10.07	ACIS-S	235678		Y
1643	700259	APM08279+5255	08 : 31 : 43.9	+52 : 45 : 48.7	3.91	2000 Oct 11	6.87	ACIS-S	123678		Y
2130	700320	3C 207	08 : 40 : 49.2	+13 : 12 : 57.0	4.14	2000 Nov 04	22.90	ACIS-S	235678		Y
818	700123	Q0842+3431	08 : 45 : 36.5	+34 : 21 : 14.0	3.41	2000 Jan 22	4.07	ACIS-S	23678		
1708	800103	CL 0848.6+4453	08 : 48 : 54.7	+44 : 54 : 33.3	2.73	2000 May 03	59.39	ACIS-I	012367	8	Y
927	800103	CL 0848.6+4453	08 : 48 : 54.8	+44 : 54 : 32.9	2.73	2000 May 04	122.18	ACIS-I	012367	8	Y
1596	700212	0902+343	09 : 05 : 32.8	+34 : 09 : 07.9	2.28	2000 Oct 26	9.68	ACIS-S	235678		Y
2452	800166	RX J0910+5422	09 : 10 : 39.1	+54 : 19 : 57.1	1.99	2001 Apr 24	63.83	ACIS-I	01236	11	
2227	800166	RX J0910+5422	09 : 10 : 39.7	+54 : 19 : 54.8	1.98	2001 Apr 29	104.25	ACIS-I	01236	11	Y
419	700091	RX J0911.4+0551	09 : 11 : 26.8	+05 : 50 : 57.3	3.70	1999 Nov 02	24.55	ACIS-S	01237	4	Y
1629	700245	RXJ0911.4+0551	09 : 11 : 28.7	+05 : 51 : 25.9	3.70	2000 Oct 29	9.13	ACIS-S	123678	4	Y
839	700144	3C 220.1	09 : 32 : 35.0	+79 : 07 : 10.8	1.90	1999 Dec 29	17.14	ACIS-S	23678		Y
805	600108	I ZW 18	09 : 33 : 56.5	+55 : 14 : 37.7	1.99	2000 Feb 08	24.49	ACIS-S	235678		Y
2453	700285	3C 228	09 : 50 : 09.3	+14 : 19 : 27.6	3.14	2001 Apr 23	9.13	ACIS-S	235678	10	
2095	700285	3C 228	09 : 50 : 09.3	+14 : 19 : 27.3	3.13	2001 Jun 03	13.69	ACIS-S	235678	10	
926	800102	MS 1008.1-1224	10 : 10 : 14.7	−12 : 41 : 04.9	6.74	2000 Jun 11	43.87	ACIS-I	012367		Y
937	900009	AX J1025+4714	10 : 25 : 54.1	+47 : 14 : 11.5	1.28	2000 Jun 07	1.99	ACIS-I	012367		
2102	700292	LBQS 1029-0125	10 : 31 : 48.1	−01 : 41 : 43.4	4.89	2001 May 30	4.40	ACIS-S	235678		
512	800020	EMSS 1054.5-0321	10 : 56 : 55.8	−03 : 39 : 20.3	3.67	2000 Apr 21	75.60	ACIS-S	123678		Y
915	800091	CL J1113.1-2615	11 : 12 : 54.1	−26 : 15 : 41.2	5.52	2000 Aug 13	101.35	ACIS-I	012367		Y
2209	800148	3C254	11 : 14 : 32.0	+40 : 36 : 56.0	1.91	2001 Mar 26	28.38	ACIS-S	23678		
363	700035	PG 1115+080	11 : 18 : 15.1	+07 : 45 : 16.0	4.01	2000 Jun 02	24.42	ACIS-S	123678	2	Y
1630	700246	PG1115+080	11 : 18 : 18.5	+07 : 46 : 29.8	4.01	2000 Nov 03	9.73	ACIS-S	123678	2	Y
868	700173	PG 1115+407	11 : 18 : 42.8	+40 : 25 : 17.6	1.91	2000 Oct 03	17.37	ACIS-I	012367		Y

Table 1—Continued

Obs. ID (1)	Sequence Number (2)	Target Name (3)	R.A. (J2000) (4)	Decl. (J2000) (5)	N_H ($10^{20} cm^{-2}$) (6)	Obs. Date (7)	Exposure (*ksec*) (8)	Aim Point Detector (9)	CCD Used (10)	Multi ID (11)	Paper I Used (12)
1660	800128	V 1121+2327	11 : 20 : 48.5	+23 : 24 : 09.1	1.30	2001 Apr 23	68.19	ACIS-I	01236		
819	700124	UM 425	11 : 23 : 19.6	+01 : 37 : 17.7	4.09	2000 Apr 07	2.55	ACIS-S	235678		
424	700096	PMN J1131+0455	11 : 31 : 58.0	+04 : 56 : 20.3	3.46	2000 Dec 15	6.37	ACIS-S	123678		
2126	700316	3C263	11 : 40 : 05.2	+65 : 47 : 59.7	1.15	2000 Oct 28	29.15	ACIS-S	235678		Y
898	800074	B1138-262	11 : 40 : 46.1	−26 : 30 : 20.9	4.95	2000 Jun 06	23.50	ACIS-S	235678		Y
536	800044	MS 1137.5+6625	11 : 40 : 47.1	+66 : 07 : 19.7	1.18	1999 Sep 30	114.61	ACIS-I	012367		Y
874	700179	1156+295	11 : 59 : 30.8	+29 : 14 : 28.4	1.66	2000 Jun 29	94.57	ACIS-I	012367		
2183	700373	SDSS1204-0021	12 : 04 : 43.3	−00 : 21 : 19.6	2.13	2000 Dec 02	5.19	ACIS-S	235678		
2083	700273	SDSS120823+001027	12 : 08 : 24.2	+00 : 11 : 00.6	1.99	2001 Mar 18	4.52	ACIS-S	235678		
2103	700293	LBQS 1205+1436	12 : 08 : 24.3	+14 : 19 : 52.6	2.56	2002 Mar 08	5.59	ACIS-S	235678		
2104	700294	LBQS 1208+1535	12 : 11 : 24.4	+15 : 19 : 22.3	2.66	2002 Mar 08	4.01	ACIS-S	235678		
2106	700296	LBQS 1216+1103	12 : 19 : 29.2	+10 : 47 : 29.0	2.14	2001 Mar 18	4.14	ACIS-S	235678		
1662	800130	V 1221+4918	12 : 21 : 31.2	+49 : 15 : 07.5	1.43	2001 Aug 05	77.01	ACIS-I	01236		
2486	900080	CHVC125	12 : 27 : 37.4	+75 : 25 : 42.0	2.73	2001 Dec 24	20.54	ACIS-S	235678	15	
938	900010	AX J1227+4421	12 : 27 : 45.0	+44 : 21 : 28.4	1.34	2000 Oct 04	4.75	ACIS-I	012367		
2484	900080	CHVC125	12 : 28 : 50.1	+75 : 24 : 23.8	2.71	2001 Oct 25	23.94	ACIS-S	235678	15	
2253	900080	CHVC125	12 : 29 : 04.5	+75 : 25 : 43.5	2.69	2002 Jan 14	43.95	ACIS-S	235678	15	
1712	790054	3C 273	12 : 29 : 06.3	+02 : 03 : 14.0	1.79	2000 Jun 14	12.04	ACIS-S	456789		Y
2107	700297	LBQS 1231+1320	12 : 33 : 54.8	+13 : 03 : 35.4	2.57	2001 Aug 07	5.82	ACIS-S	235678		
2108	700298	LBQS 1235+0857	12 : 37 : 53.8	+08 : 41 : 40.7	1.74	2001 Mar 18	5.33	ACIS-S	235678		
820	700125	LBQS 1235+1807B	12 : 38 : 22.0	+17 : 51 : 12.6	1.96	2000 Jan 21	1.24	ACIS-S	23678		
2109	700299	LBQS 1239+0955	12 : 41 : 34.8	+09 : 38 : 59.2	1.79	2001 Jul 25	5.06	ACIS-S	235678		
821	700126	Q1246-0542	12 : 49 : 15.6	−05 : 58 : 47.9	2.17	2000 Feb 08	5.38	ACIS-S	235678		
2084	700274	PC 1247+3406	12 : 49 : 39.4	+33 : 50 : 10.0	1.23	2001 Mar 24	4.52	ACIS-S	235678		
1031	700389	Mrk 231	12 : 56 : 19.0	+56 : 52 : 24.6	1.25	2000 Oct 19	23.30	ACIS-S	235678		
2210	800149	3C280	12 : 56 : 58.7	+47 : 19 : 48.2	1.15	2001 Aug 27	49.80	ACIS-S	235678		
325	800063	S-Z CLUSTER	13 : 12 : 22.4	+42 : 41 : 42.8	1.37	1999 Dec 03	80.61	ACIS-S	23678		Y
2228	800167	RX J1317.4+2911	13 : 17 : 12.2	+29 : 10 : 18.3	1.04	2001 May 04	108.09	ACIS-I	01236		Y
2110	700300	LBQS 1331-0108	13 : 34 : 28.8	−01 : 23 : 12.4	2.31	2001 Mar 18	4.96	ACIS-S	235678		
415	700087	NGC 5273	13 : 42 : 11.5	+35 : 37 : 34.9	0.96	2000 Sep 03	1.44	ACIS-S	235678		
2249	900076	RXJ13434+0001	13 : 43 : 30.7	+00 : 02 : 04.7	1.90	2001 Jan 08	9.53	ACIS-S	235678	14	
2250	900077	F864X:052	13 : 44 : 08.8	−00 : 28 : 01.6	2.02	2001 Jan 08	8.74	ACIS-S	235678		
2251	900078	F864X:012	13 : 44 : 26.6	−00 : 00 : 35.3	1.93	2001 Jan 08	9.54	ACIS-S	235678	14	
809	700114	MRK 273X	13 : 44 : 43.0	+55 : 54 : 16.4	1.09	2000 Apr 19	40.93	ACIS-S	012367		Y
507	800015	RX J1347-114	13 : 47 : 28.7	−11 : 46 : 24.2	4.88	2000 Apr 29	9.90	ACIS-S	235678		Y
2229	800168	RX J1350.0+6007	13 : 50 : 55.1	+60 : 05 : 08.6	1.76	2001 Aug 29	54.86	ACIS-I	01236		
1588	700204	3C294	14 : 06 : 50.4	+34 : 11 : 20.0	1.21	2000 Oct 29	19.02	ACIS-S	235678		Y
578	890023	3C295	14 : 11 : 11.5	+52 : 13 : 01.6	1.34	1999 Aug 30	15.80	ACIS-S	235678	7	Y
2254	900081	3C295	14 : 11 : 18.3	+52 : 12 : 10.3	1.34	2001 May 18	87.48	ACIS-I	012367	7	
930	800106	H1413+117	14 : 15 : 43.9	+11 : 30 : 00.1	1.80	2000 Apr 19	24.09	ACIS-S	456789		Y
2024	600158	RXJ1416.4+2315	14 : 16 : 28.0	+23 : 14 : 02.1	1.91	2001 Sep 05	14.47	ACIS-S	235678		
541	800049	V1416+4446	14 : 16 : 43.0	+44 : 48 : 28.5	1.24	1999 Dec 02	29.67	ACIS-I	01236		Y
1657	800125	MACS J1423.8+2404	14 : 23 : 36.2	+24 : 02 : 48.6	2.48	2001 Jun 01	18.23	ACIS-I	01236		
367	700039	Q1422+231	14 : 24 : 35.6	+22 : 55 : 43.7	2.69	2000 Jun 01	26.75	ACIS-S	123678		
907	800083	QB 1429-008A,B	14 : 32 : 29.5	−01 : 05 : 58.4	3.54	2000 Mar 31	21.32	ACIS-I	01236		Y
2111	700301	LBQS 1442-0011	14 : 45 : 12.8	−00 : 24 : 21.1	3.69	2001 May 30	3.98	ACIS-S	235678		
2112	700302	LBQS 1443+0141	14 : 45 : 45.7	+01 : 29 : 50.2	3.47	2001 Mar 23	5.84	ACIS-S	235678		
939	900011	AX J1510+0742	15 : 10 : 22.2	+07 : 42 : 05.4	2.45	2000 Jun 01	4.54	ACIS-I	012367		
800	600103	CB 58	15 : 14 : 18.5	+36 : 36 : 11.7	1.35	2000 Jun 06	43.55	ACIS-S	235678		
800	600103	CB 58	15 : 14 : 18.5	+36 : 36 : 11.7	1.35	2000 Jul 07	43.55	ACIS-S	235678		
2085	700275	SDSSJ153259-003944	15 : 33 : 00.3	−00 : 39 : 06.5	6.25	2001 Mar 26	4.99	ACIS-S	235678		
869	700174	ARP 220	15 : 34 : 54.7	+23 : 29 : 52.5	4.28	2000 Jun 24	54.18	ACIS-S	235678		Y
822	700127	SBSG 1542+541	15 : 43 : 58.3	+53 : 59 : 49.0	1.27	2000 Mar 22	4.05	ACIS-S	235678		
326	800064	3C 324	15 : 49 : 46.3	+21 : 25 : 19.3	4.30	2000 Jun 25	31.95	ACIS-S	235678		Y
981	200088	HD141569	15 : 49 : 51.0	−03 : 55 : 38.3	9.59	2001 Jun 23	2.62	ACIS-I	012367		
2086	700276	SDSS160501-011220	16 : 04 : 59.2	−01 : 12 : 44.5	8.92	2001 Jun 24	4.54	ACIS-S	235678		
427	700099	CLASS 1608+656	16 : 09 : 10.6	+65 : 32 : 26.2	2.68	2000 Jan 20	4.88	ACIS-S	01237		
2127	700317	3C330	16 : 09 : 39.8	+65 : 56 : 24.6	2.83	2001 Oct 16	40.23	ACIS-S	235678		
2184	700374	SDSS1621-0042	16 : 21 : 16.2	−00 : 43 : 25.0	7.26	2001 Sep 05	1.27	ACIS-S	235678		
546	800054	MS 1621.5+2640	16 : 23 : 25.4	+26 : 36 : 12.4	3.59	2000 Apr 24	29.57	ACIS-I	01236		Y
615	200040	VB 8	16 : 55 : 34.0	−08 : 24 : 07.6	13.40	2000 Jul 10	8.54	ACIS-S	456789		Y
2221	800160	53W002 CLUSTER	17 : 14 : 16.5	+50 : 15 : 07.9	2.29	2001 Nov 01	35.97	ACIS-S	23678		
548	800056	RX J1716.9+6708	17 : 17 : 01.0	+67 : 11 : 44.1	3.71	2000 Feb 27	50.35	ACIS-I	01236		Y
841	700146	3C 371	18 : 06 : 52.3	+69 : 50 : 05.5	4.84	2000 Mar 21	9.43	ACIS-S	456789		Y
1899	300047	DQ HERCULIS	18 : 07 : 27.1	+45 : 51 : 17.8	3.63	2001 Jul 26	43.70	ACIS-S	235678	9	

Table 1—Continued

Obs. ID (1)	Sequence Number (2)	Target Name (3)	R.A. (J2000) (4)	Decl. (J2000) (5)	N_H ($10^{20} cm^{-2}$) (6)	Obs. Date (7)	Exposure (*ksec*) (8)	Aim Point Detector (9)	CCD Used (10)	Multi ID (11)	Paper I Used (12)
2503	300047	DQ HERCULIS	18 : 07 : 27.1	+45 : 51 : 17.9	3.63	2001 Jul 29	20.90	ACIS-S	235678	9	
830	700135	JET OF 3C 390.3	18 : 41 : 46.8	+79 : 48 : 21.2	4.16	2000 Apr 17	22.71	ACIS-S	235678		Y
842	700147	PKS 2005-489	20 : 09 : 25.2	−48 : 50 : 14.5	5.03	2000 Oct 07	5.17	ACIS-I	012367		
551	800059	MS 2053.7-0449	20 : 56 : 18.6	−04 : 34 : 32.3	4.95	2000 May 13	42.34	ACIS-I	01236	6	Y
1667	800135	MS 2053.7-0449	20 : 56 : 23.6	−04 : 41 : 02.7	4.95	2001 Oct 07	43.23	ACIS-I	01236	6	
2036	600170	IRAS 20551-4250	20 : 58 : 27.8	−42 : 39 : 40.3	3.82	2001 Oct 31	34.31	ACIS-S	235678		
1626	700242	PKS 2135-14	21 : 37 : 45.6	−14 : 33 : 30.5	4.65	2001 Oct 07	14.44	ACIS-S	235678		
928	800104	MS 2137.3-2353	21 : 40 : 14.8	−23 : 40 : 22.0	3.57	1999 Nov 18	29.09	ACIS-S	23678		Y
1644	700260	HE2149-2745	21 : 52 : 07.8	−27 : 32 : 28.2	2.33	2000 Nov 18	9.18	ACIS-S	123678		Y
2113	700303	LBQS 2154-2005	21 : 57 : 07.2	−19 : 51 : 44.4	2.71	2001 Sep 04	3.91	ACIS-S	235678		
2114	700304	LBQS 2201-1834	22 : 04 : 02.1	−18 : 19 : 07.9	2.79	2001 Aug 03	4.98	ACIS-S	235678		
1479	980429	LEONID ANTI-RADIANT	22 : 13 : 12.7	−22 : 10 : 43.4	2.49	1999 Nov 17	20.02	ACIS-I	01236		Y
2185	700375	BRI 2212-1626	22 : 15 : 27.5	−16 : 12 : 08.1	2.65	2001 Dec 16	2.73	ACIS-S	235678		
1694	900053	PROTO CLUSTER	22 : 17 : 28.2	+00 : 15 : 09.9	4.61	2001 Jul 10	75.27	ACIS-S	235678		
789	600092	HCG 92	22 : 35 : 58.5	+33 : 59 : 31.4	7.74	2000 Jul 09	19.60	ACIS-S	235678		Y
431	700103	EINSTEIN CROSS	22 : 40 : 27.9	+03 : 21 : 19.2	5.35	2000 Sep 06	21.89	ACIS-S	123678	5	Y
1632	700248	2237+0305	22 : 40 : 30.9	+03 : 20 : 54.2	5.34	2001 Dec 08	8.06	ACIS-S	123678	5	
918	800094	CL J2302.8+0844	23 : 02 : 47.4	+08 : 45 : 14.7	5.05	2000 Aug 05	106.09	ACIS-I	012367		Y
861	700166	Q2345+007	23 : 48 : 18.1	+00 : 58 : 36.4	3.81	2000 May 26	65.00	ACIS-S	123678		Y
861	700166	Q2345+007	23 : 48 : 18.1	+00 : 58 : 36.4	3.81	2000 Jun 27	65.00	ACIS-S	123678		Y
2115	700305	LBQS 2350-0045A	23 : 52 : 53.0	−00 : 28 : 17.2	3.47	2002 May 16	5.09	ACIS-S	235678		

Note. — Col. (1): observational ID. Col. (2): sequence number. Col. (3): target name. Col. (4) and (5): the right ascension in units of hours, minutes, and seconds, and declination in units of degrees, arcminutes, and arcseconds of the aim point in J2000. Col. (6): the galactic extinction in units of 10^{20} cm^{-2} from Stark et al. (1992). Col. (7): the date of observation. Col. (8): the net exposure time estimated after removing background flares within the aim pointed CCD chip. Col. (9): aim point detector type. Col. (10): used CCD chips (CCD ID=0-3 for ACIS-I and 4-9 for ACIS-S). Col. (11): multiple observation ID indicates overlapping fields, labeled with the same ID. Col. (12): 62 ChaMP fields included in Paper I are marked as Y.

Table 2. Definition of Energy Bands and X-ray Colors

Band	Definition
Broad (B)	$0.3-8$ keV
Soft (S)	$0.3-2.5$ keV
Hard (H)	$2.5-8$ keV
Soft1 (S_1)	$0.3-0.9$ keV
Soft2 (S_2)	$0.9-2.5$ keV
Conventional Broad (Bc)	$0.5-8$ keV
Conventional Soft (Sc)	$0.5-2$ keV
Conventional Hard (Hc)	$2-8$ keV
Hardness Ratio HR	$(\mathrm{Hc}-\mathrm{Sc})/(\mathrm{Hc}+\mathrm{Sc})$
X-ray Color $C21$	$-log(\mathrm{S_2})+log(\mathrm{S_1})=log(\mathrm{S_1}/\mathrm{S_2})$
X-ray Color $C32$	$-log(\mathrm{H})+log(\mathrm{S_2})=log(\mathrm{S_2}/\mathrm{H})$

Table 3. Energy Conversion Factor

Obs.	CCD	$\Gamma_{ph} = 1.2$						$\Gamma_{ph} = 1.4$						$\Gamma_{ph} = 1.7$					
ID	ID	B	S	H	Bc	Sc	Hc	B	S	H	Bc	Sc	Hc	B	S	H	Bc	Sc	Hc
(1)	(2)	(3)	(4)	(5)	(6)	(7)	(8)	(9)	(10)	(11)	(12)	(13)	(14)	(15)	(16)	(17)	(18)	(19)	(20)
135	2	130.25	64.24	289.26	128.03	50.19	262.14	117.76	65.36	277.79	114.15	50.74	250.33	104.04	68.04	262.06	97.53	51.74	234.34
135	3	131.44	65.01	289.92	129.12	50.77	263.01	118.98	66.21	278.41	115.23	51.36	251.20	105.31	69.03	262.70	98.60	52.44	235.21
135	5	103.05	44.69	341.86	108.74	37.58	289.69	87.98	43.67	324.75	93.20	37.10	272.63	71.00	42.50	301.68	75.06	36.43	249.91
135	6	115.00	56.38	259.13	113.61	44.20	235.68	103.57	57.09	249.59	101.04	44.53	225.69	90.79	58.94	236.46	85.88	45.16	212.07
135	7	85.12	38.20	248.29	89.43	32.10	217.62	73.37	37.40	237.38	77.30	31.73	206.28	59.93	36.52	222.43	62.89	31.19	190.93
325	2	135.69	65.77	314.52	133.17	51.72	277.16	122.42	67.05	301.06	118.41	52.31	263.12	107.98	70.02	282.68	100.88	53.40	244.09
325	3	136.58	66.61	311.79	133.90	52.20	276.84	123.44	67.96	298.62	119.24	52.85	263.16	109.16	71.07	280.62	101.81	54.01	244.65
325	6	116.57	56.64	268.51	114.83	44.43	240.60	104.94	57.48	258.07	102.01	44.81	229.59	92.06	59.55	243.72	86.62	45.50	214.58
325	7	87.06	39.22	250.62	90.66	32.64	219.17	75.33	38.53	240.01	78.57	32.33	208.12	61.90	37.82	225.51	64.19	31.90	193.17
326	2	141.37	72.20	289.98	137.55	56.19	263.37	129.48	74.21	278.53	123.88	57.19	251.61	116.84	78.56	262.84	107.52	58.94	235.67
326	3	142.52	72.95	290.89	138.63	56.76	264.47	130.64	75.04	279.41	124.94	57.80	252.67	118.06	79.53	263.69	108.58	59.64	236.72
326	5	120.60	54.50	343.34	121.62	43.95	291.69	105.60	54.40	326.20	105.76	43.84	274.61	88.81	54.81	303.08	87.11	43.74	251.86
326	6	123.48	62.82	255.43	120.47	48.92	232.80	112.81	64.33	246.06	108.31	49.65	223.00	101.26	67.67	233.17	93.65	50.94	209.66
326	7	98.82	46.35	250.47	99.86	37.54	220.71	87.34	46.35	239.60	87.68	37.54	209.47	74.35	46.85	224.73	73.11	37.58	194.26
342	2	134.75	67.44	289.09	131.78	52.54	262.23	122.53	68.93	277.65	118.00	53.27	250.46	109.28	72.31	261.99	101.50	54.58	234.53
342	3	135.96	68.20	290.14	132.89	53.11	263.41	123.75	69.77	278.65	119.10	53.89	251.61	110.55	73.29	262.93	102.58	55.28	235.66
342	5	110.56	48.78	342.63	114.09	40.15	290.59	95.47	48.13	325.50	98.40	39.82	273.51	78.48	47.57	302.36	80.02	39.38	250.76
342	6	117.31	58.39	254.84	115.17	45.59	231.94	106.32	59.43	245.47	102.90	46.08	222.13	94.18	61.88	232.56	88.10	46.96	208.77
342	7	91.03	41.60	249.81	93.99	34.36	219.79	79.37	41.14	238.95	81.85	34.16	208.54	66.07	40.82	224.08	67.39	33.91	193.32
346	2	142.39	70.28	315.57	138.98	55.17	278.54	129.36	72.03	302.11	124.25	56.01	264.48	115.39	75.89	283.72	106.75	57.50	245.45
346	3	143.17	71.10	312.78	139.63	55.64	278.13	130.28	72.92	299.59	125.01	56.53	264.46	116.49	76.92	281.59	107.63	58.10	245.94
346	6	122.63	60.78	269.13	120.00	47.52	241.52	111.24	62.04	258.69	107.23	48.11	230.52	98.83	64.91	244.37	91.90	49.16	215.55
346	7	94.67	43.72	251.38	96.25	35.56	220.19	83.06	43.46	240.76	84.06	35.41	209.12	69.83	43.46	226.25	69.51	35.23	194.16
363	1	171.64	85.40	373.31	167.13	66.33	335.14	156.41	87.78	356.94	149.76	67.53	318.67	140.29	92.93	334.70	129.20	69.63	296.58
363	2	140.46	71.54	289.81	136.75	55.67	263.18	128.52	73.48	278.36	123.06	56.63	251.40	115.80	77.69	262.70	106.68	58.33	235.49
363	3	141.64	72.30	290.84	137.85	56.25	264.36	129.71	74.31	279.35	124.14	57.26	252.55	117.04	78.66	263.62	107.75	59.03	236.59
363	6	122.66	62.21	255.43	119.76	48.45	232.76	111.94	63.65	246.06	107.58	49.15	222.95	100.30	66.87	233.17	92.89	50.38	209.60
363	7	97.79	45.71	250.42	99.07	37.10	220.62	86.29	45.65	239.55	86.89	37.07	209.38	73.24	46.03	224.68	72.33	37.07	194.16
367	1	160.01	77.47	372.08	157.13	60.37	333.43	144.28	78.97	355.71	139.66	61.12	316.96	127.18	82.44	333.48	118.95	62.46	294.88
367	2	131.06	64.83	289.04	128.71	50.63	262.02	118.62	66.01	277.59	114.86	51.21	250.23	104.97	68.81	261.90	98.25	52.26	234.29

Note. — Col. (1): observation ID. Col. (2): CCD ID. Col. (3) - Col. (8): energy conversion factors in units of *erg* cm^{-2} *count*$^{-1}$ assumimg a photon index of $\Gamma_{ph} = 1.2$ in the B, S, H, Bc, Sc, and Hc bands, respectively. Col. (9) - Col. (14): energy conversion factors in units of *erg* cm^{-2} *count*$^{-1}$ assuming a photon index $\Gamma_{ph} = 1.4$ in the B, S, H, Bc, Sc, and Hc bands, respectively. Col. (15) - Col. (20): energy conversion factors in units of *erg* cm^{-2} *count*$^{-1}$ assuming a photon index of $\Gamma_{ph} = 1.7$ in the B, S, H, Bc, Sc, and Hc bands, respectively. The complete version of this table is in the electronic edition of the *Astrophysical Journal Supplement*. The printed edition contains only a sample.

Table 4. Definition of Source Flag

Flag	Definition
1n	False X-ray Sources
11	False source due to a hot pixel or by a bad bias value
12	False source due to a bad column
13	False source along the readout direction of a very strong source
14	False source due to the FEP 0/3 problem
15	Double sources detected due to the PSF effect
2n	It is not certain whether it is a valid X-ray source
21	V&Ver found it might be a spurious source
3n	Source properties may be subject to a large uncertainty
31	Bad pixel/column exists within source extraction radius
37	Pile-up (see *Chandra* POG 2004)
38	Uncertain source position by flag=015
5n	Other cases
51	Source is extended
52	Same source candidate in multiple observations
53	Target of observation
54	X-ray jet
55	Variable source (see Paper I)
6n	Flagged by the automatic pipeline *xapphot*
61	Source region falls near the edge of the chip
62	Small portion of source region overlaps with nearby point source
63	Large portion of source region overlaps with nearby point source
64	Small portion of source region overlaps with nearby extended source
65	Large portion of source region overlaps with nearby extended source
66	Background region overlaps with a nearby point source
67	Background region overlaps with a nearby extended source
68	Source region falls inside the extended source

Table 5. The Main ChaMP X-ray Point Sources

Source Name (1)	Obs. ID (2)	CCD ID (3)	Source No. (4)	R.A. (deg) (5)	Decl. (deg) (6)	PU (arcsec) (7)	$D_{off-axis}$ (arcmin) (8)	Radius (arcsec) (9)	Exposure (ksec) (10)	Flag (11)
CXOMP J001709.7+162604	520	6	1	4.290515	16.434570	60:	20.28	40.00	51.72	66
CXOMP J001716.0+162722	520	6	4	4.316865	16.456352	60:	18.56	40.00	53.94	66
CXOMP J001739.7+162330	520	6	2	4.415671	16.391680	3.12	14.28	27.02	59.54	
CXOMP J001743.5+163144	520	2	24	4.431394	16.528941	7.21	11.90	18.98	48.00	
CXOMP J001756.6+163006	520	2	23	4.486132	16.501804	2.44	8.63	10.69	55.58	
CXOMP J001758.4+162647	520	2	21	4.493674	16.446530	2.79	8.82	11.11	58.17	55
CXOMP J001758.9+163119	520	2	20	4.495359	16.521831	1.79	8.20	9.75	58.94	66
CXOMP J001801.0+163139	520	2	19	4.504432	16.527670	2.14	7.75	8.77	54.89	66
CXOMP J001801.4+163237	520	2	18	4.506178	16.543632	2.59	7.90	9.12	59.10	
CXOMP J001801.7+163426	520	2	17	4.507101	16.573669	1.69	8.61	10.65	58.61	
CXOMP J001803.4+162751	520	2	12	4.514173	16.464428	2.34	7.35	8.01	57.29	
CXOMP J001805.7+162852	520	2	22	4.523928	16.481311	1.96	6.56	6.76	60.74	55
CXOMP J001805.9+163038	520	2	16	4.524780	16.510817	2.17	6.43	6.56	58.35	
CXOMP J001806.7+162517	520	3	15	4.528315	16.421658	3.36	7.82	8.93	51.74	66
CXOMP J001807.2+163551	520	2	15	4.530068	16.597307	2.19	8.41	10.21	58.89	
CXOMP J001807.9+163120	520	2	5	4.532916	16.522052	0.80	6.07	5.99	61.20	
CXOMP J001808.5+163231	520	2	4	4.535611	16.541869	0.94	6.28	6.32	61.51	66
CXOMP J001809.3+162532	520	3	10	4.538662	16.425403	1.16	7.21	7.78	54.48	66
CXOMP J001809.8+162556	520	3	14	4.540869	16.432422	1.98	6.85	7.22	44.87	66
CXOMP J001810.0+163208	520	2	11	4.541983	16.535624	1.51	5.80	5.57	62.13	66
CXOMP J001810.2+162942	520	2	10	4.542706	16.494819	1.37	5.39	4.91	62.60	
CXOMP J001810.2+163223	520	2	3	4.542568	16.539805	0.44	5.87	5.67	61.15	66
CXOMP J001812.4+162713	520	2	9	4.551720	16.453788	1.60	5.62	5.27	62.26	
CXOMP J001817.6+163107	520	2	2	4.573363	16.518440	0.75	3.76	3.18	64.71	
CXOMP J001818.0+163316	520	2	8	4.575189	16.554260	0.85	4.75	4.07	62.00	
CXOMP J001818.8+163748	520	0	30	4.578632	16.630076	3.25	8.43	10.25	56.52	66
CXOMP J001820.0+162931	520	2	14	4.583690	16.491973	2.74	3.06	3.00	62.63	
CXOMP J001820.7+162315	520	3	13	4.586617	16.387553	2.74	7.37	8.04	54.98	
CXOMP J001821.2+163238	520	2	13	4.588713	16.544022	1.80	3.76	3.18	34.15	
CXOMP J001821.7+161941	520	3	9	4.590651	16.327982	1.52	10.70	15.62	51.46	
CXOMP J001822.1+162926	520	2	7	4.592218	16.490700	1.14	2.60	3.00	66.04	

Note. — Col. (1): ChaMP source name given by right ascension in units of hours, minutes, and seconds, and declination in units of degrees, arcminutes, and arcseconds in J2000. Col. (2): observation ID. Col. (3): CCD ID (0-3 for ACIS-I and 4-9 for ACIS-S observation). Col. (4): source number assigned by *wavdetect* as marked in the public X-ray image of the ChaMP web site (http://hea-www.harvard.edu/CHAMP). Col. (5) and (6): right ascension and declination in units of degrees after refinement and aspect correction. Col. (7): positional uncertainty in units of arcseconds estimated by the 95% confidence level of the empirical formula (see equation (12) in §4.2). Col. (8): off axis angle from the aim point of the observation in units of arcminutes. Col. (9): source extraction radius in units of arcseconds (The 95% encircled energy radius at 1.5 keV. See §3.2.1). Col. (10): mean effective exposure time in units of ksec after vignetting correction (see §3.2.4). Col. (11): source flag (see Table 4). The complete version of this table is in the electronic edition of the *Astrophysical Journal Supplement*. The printed edition contains only a sample.

Table 6. The Supplementary ChaMP X-ray Point Sources

Source Name (1)	Obs. ID (2)	CCD ID (3)	Source No. (4)	R.A. (deg) (5)	Decl. (deg) (6)	PU (arcsec) (7)	$D_{off-axis}$ (arcmin) (8)	Radius (arcsec) (9)	Exposure (ksec) (10)	Flag (11)
CXOMP J005618.9-272429	2242	3	4	14.079076	-27.408259	15.58	13.24	23.32	8.60	66
CXOMP J005622.4-272223	2242	3	2	14.093514	-27.373174	6.50	12.31	20.13	8.33	
CXOMP J005622.8-272746	2242	3	3	14.095076	-27.462953	13.97	13.35	23.71	8.35	
CXOMP J005630.6-273141	2242	2	4	14.127555	-27.528123	12.27	14.01	26.06	9.67	66
CXOMP J005633.8-272954	2242	2	2	14.140895	-27.498360	5.52	12.33	20.18	10.15	66
CXOMP J005644.3-274936	2243	3	5	14.184665	-27.826692	18.16	11.18	16.97	8.13	
CXOMP J005645.6-272444	2242	3	1	14.190344	-27.412292	3.66	7.52	8.29	9.59	
CXOMP J005645.9-275522	2243	3	4	14.191467	-27.922784	8.72	14.68	28.46	7.53	
CXOMP J005649.8-273319	2242	2	3	14.207559	-27.555305	11.77	12.57	20.92	9.28	
CXOMP J005651.7-272856	2242	2	1	14.215693	-27.482293	2.70	8.74	10.92	10.86	
CXOMP J005654.5-275116	2243	3	3	14.227221	-27.854715	8.08	10.39	14.74	8.23	
CXOMP J005657.0-274025	2244	3	1	14.237721	-27.673876	4.54	11.58	18.08	8.04	
CXOMP J005659.0-274913	2243	3	2	14.246074	-27.820540	6.08	8.27	9.92	8.59	
CXOMP J005659.3-272251	2242	7	6	14.247296	-27.381031	1.82	4.14	3.52	6.14	
CXOMP J005701.0-272334	2242	7	5	14.254508	-27.393036	2.27	3.91	3.31	6.11	
CXOMP J005701.4-274344	2243	7	6	14.256135	-27.729051	3.35	5.91	5.74	7.97	
CXOMP J005704.7-280145	2246	2	3	14.269942	-28.029192	60:	14.83	29.00	7.58	
CXOMP J005705.3-274554	2243	7	7	14.272302	-27.765143	3.78	5.38	4.90	5.83	
CXOMP J005710.1-274952	2246	3	2	14.292476	-27.831169	6.09	12.02	19.31	8.42	
CXOMP J005710.2-274954	2243	3	1	14.292750	-27.831766	2.15	7.08	7.58	8.20	52
CXOMP J005712.9-272650	2242	6	15	14.303934	-27.447320	2.70	4.58	3.91	10.66	
CXOMP J005714.0-272536	2242	6	4	14.308480	-27.426900	2.22	3.33	3.00	10.88	
CXOMP J005714.9-271851	2242	7	4	14.312284	-27.314413	1.20	3.59	3.02	6.57	
CXOMP J005715.3-271735	2242	7	7	14.313933	-27.293127	2.20	4.84	4.15	6.10	
CXOMP J005716.6-273230	2244	7	11	14.319131	-27.541602	1.18	5.03	4.35	6.47	
CXOMP J005716.8-272128	2242	7	1	14.320197	-27.357975	0.41	0.95	3.00	6.35	53
CXOMP J005717.3-274236	2243	7	5	14.322400	-27.710021	0.61	2.78	3.00	8.42	
CXOMP J005717.5-272617	2242	6	7	14.322936	-27.438214	1.42	3.90	3.30	10.74	
CXOMP J005717.9-271830	2242	7	3	14.324672	-27.308354	1.16	3.90	3.30	6.55	55
CXOMP J005719.7-272035	2242	7	2	14.332301	-27.343318	1.29	1.85	3.00	6.35	
CXOMP J005720.5-274452	2243	7	4	14.335529	-27.747964	0.73	1.89	3.00	8.41	

Note. — Col. (1): ChaMP source name given by right ascension in units of hours, minutes, and seconds, and declination in units of degrees, arcminutes, and arcseconds in J2000. Col. (2): observation ID. Col. (3): CCD ID (0-3 for ACIS-I and 4-9 for ACIS-S observation). Col. (4): source number assigned by *wavdetect* as marked in the public X-ray image of the ChaMP web site (http://hea-www.harvard.edu/CHAMP). Col. (5) and (6): right ascension and declination in units of degrees after refinement and aspect correction. Col. (7): positional uncertainty in units of arcseconds estimated by the 95% confidence level of the empirical formula (see equation (12) in §4.2). Col. (8): off axis angle from the aim point of the observation in units of arcminutes. Col. (9): source extraction radius in units of arcseconds (The 95% energy encircled radius at 1.5 keV. See §3.2.1). Col. (10): mean effective exposure time in units of ksec after vignetting correction (see §3.2.4). Col. (11): source flag (see Table 4). The complete version of this table is in the electronic edition of the *Astrophysical Journal Supplement*. The printed edition contains only a sample.

Table 7. The Multiply-Observed ChaMP X-ray Point Source Candidates

Source Name (1)	Multi ID (2)	Obs. ID (3)	CCD ID (4)	Source No. (5)	Obs. Date (6)	netB (7)	rateB (8)	$D_{off-axis}$ (arcmin) (9)	PU (arcsec) (10)
CXOMP J025656.1-331757	1	135	6	1	Feb 15 2000	3.00 ± 2.94	4.20 ± 4.11	2.65	1.84
CXOMP J025656.1-331756	1	815	6	2	Jan 2 2000	2.00 ± 2.66	1.30 ± 1.73	2.43	2.13
CXOMP J025655.6-332109	2	135	6	2	Feb 15 2000	5.86 ± 3.60	6.65 ± 4.09	5.40	2.74
CXOMP J025655.9-332106	2	815	6	4	Jan 2 2000	3.62 ± 3.18	2.47 ± 2.17	5.31	4.66
CXOMP J025647.8-331524	3	135	7	1	Feb 15 2000	24.81 ± 6.08	27.44 ± 6.72	0.65	0.38
CXOMP J025647.8-331524	3	815	7	1	Jan 2 2000	17.85 ± 5.33	15.97 ± 4.77	0.65	0.46
CXOMP J025642.6-331521	4	135	7	2	Feb 15 2000	24.00 ± 5.98	26.69 ± 6.65	1.23	0.45
CXOMP J025642.5-331520	4	815	7	2	Jan 2 2000	27.81 ± 6.36	25.27 ± 5.78	1.52	0.46
CXOMP J025639.1-331503	5	135	7	3	Feb 15 2000	12.00 ± 4.57	13.32 ± 5.08	1.99	0.78
CXOMP J025639.1-331502	5	815	7	3	Jan 2 2000	17.90 ± 5.33	16.53 ± 4.92	2.29	0.71
CXOMP J111812.0+074030	6	363	6	2	Jun 2 2000	75.25 ± 9.82	3.45 ± 0.45	4.85	0.67
CXOMP J111812.1+074031	6	1630	7	17	Nov 3 2000	29.20 ± 6.74	3.36 ± 0.77	6.17	1.57
CXOMP J111802.3+074325	7	363	6	5	Jun 2 2000	35.48 ± 7.07	1.54 ± 0.31	3.69	1.03
CXOMP J111802.3+074325	7	1630	7	21	Nov 3 2000	13.66 ± 4.98	1.54 ± 0.56	5.03	1.60
CXOMP J111759.2+074405	8	363	6	6	Jun 2 2000	167.33 ± 13.99	7.30 ± 0.61	4.14	0.33
CXOMP J111759.2+074405	8	1630	7	22	Nov 3 2000	74.84 ± 9.77	8.03 ± 1.05	5.33	0.93
CXOMP J111806.3+074053	9	363	6	10	Jun 2 2000	19.71 ± 5.67	0.89 ± 0.26	4.91	1.66
CXOMP J111806.2+074056	9	1630	7	25	Nov 3 2000	12.80 ± 4.99	1.46 ± 0.57	6.33	3.45
CXOMP J111804.2+074324	10	363	6	11	Jun 2 2000	10.57 ± 4.43	0.46 ± 0.19	3.30	1.92
CXOMP J111804.2+074324	10	1630	7	27	Nov 3 2000	6.22 ± 3.79	0.66 ± 0.40	4.68	2.52
CXOMP J111758.6+074310	11	363	6	12	Jun 2 2000	15.95 ± 5.22	0.70 ± 0.23	4.61	1.75
CXOMP J111758.6+074311	11	1630	7	23	Nov 3 2000	11.19 ± 4.72	1.22 ± 0.51	5.90	3.49
CXOMP J111822.2+074448	12	363	7	1	Jun 2 2000	371.34 ± 20.33	16.68 ± 0.91	1.79	0.17
CXOMP J111822.2+074448	12	1630	7	1	Nov 3 2000	193.57 ± 14.96	20.71 ± 1.60	1.93	0.20
CXOMP J111816.9+074558	13	363	7	2	Jun 2 2000	1681.05 ± 42.05	72.06 ± 1.80	0.81	0.10
CXOMP J111816.9+074558	13	1630	7	2	Nov 3 2000	642.60 ± 26.38	68.48 ± 2.81	0.63	0.11
CXOMP J111816.8+074600	14	363	7	3	Jun 2 2000	1605.85 ± 41.12	68.85 ± 1.76	0.82	0.14
CXOMP J111816.8+074600	14	1630	7	3	Nov 3 2000	113.70 ± 11.74	12.11 ± 1.25	0.62	0.19
CXOMP J111816.1+074315	15	363	7	5	Jun 2 2000	92.84 ± 10.74	9.82 ± 1.14	2.04	0.28
CXOMP J111816.2+074315	15	1630	7	6	Nov 3 2000	85.50 ± 10.32	8.93 ± 1.08	3.28	0.41

Note. — Col. (1): ChaMP source name given by right ascension in units of hours, minutes, and seconds, and. declination in units of degrees, arcminutes, and arcseconds in J2000. Col. (2): multiple observation ID indicates the same source candidate in overlapping fields, labeled with the same ID. Col. (3): observation ID. Col. (4): CCD ID (0-3 for ACIS-I and 4-9 for ACIS-S). Col. (5): source number assigned by *wavdetect* as marked in the public X-ray images of the ChaMP web site (http://hea-www.harvard.edu/CHAMP). Col. (6): date of observation. Col. (7): net counts in the 0.3-8 keV band and errors. Col. (8): count rates in the 0.3-8 keV band and errors. Col. (9): off axis angle from the aim point of the observation in units of arcminutes. Col. (10): positional uncertainty in units of arcseconds estimated by the 95% confidence level of the empirical formula (see equation (12) in §4.2). The errors in net counts are given following Gehrels statistics (Gehrels 1986). The complete version of this table is in the electronic edition of the *Astrophysical Journal Supplement*. The printed edition contains only a sample.

Table 8. The Main ChaMP X-ray Point Source Photometry

Source Name (1)	B (2)	S_1 (3)	S_2 (4)	S (5)	H (6)	Bc (7)	Sc (8)	Hc (9)
CXOMP J001709.7+162604	10.20 ± 17.71	5.55 ± 9.03	14.43 ± 10.48	19.98 ± 13.40	—	6.13 ± 17.38	17.75 ± 11.51	—
CXOMP J001716.0+162722	94.40 ± 20.17	25.10 ± 9.91	48.11 ± 12.09	73.21 ± 15.20	21.19 ± 13.91	90.00 ± 20.10	60.42 ± 13.42	29.58 ± 14.97
CXOMP J001739.7+162330	233.49 ± 20.14	51.89 ± 9.68	131.11 ± 14.06	183.00 ± 16.66	50.48 ± 12.03	234.00 ± 20.48	169.84 ± 15.74	64.16 ± 13.11
CXOMP J001743.5+163144	20.29 ± 9.20	—	16.27 ± 6.38	15.86 ± 7.24	4.43 ± 6.39	21.71 ± 9.45	18.72 ± 6.76	3.00 ± 6.61
CXOMP J001756.6+163006	34.54 ± 8.17	6.26 ± 4.14	19.36 ± 6.00	25.62 ± 6.84	8.92 ± 5.26	30.65 ± 8.28	20.31 ± 6.10	10.34 ± 5.60
CXOMP J001758.4+162647	29.16 ± 8.14	4.83 ± 3.99	14.49 ± 5.59	19.32 ± 6.41	9.85 ± 5.74	28.73 ± 8.53	20.11 ± 6.21	8.63 ± 5.85
CXOMP J001758.9+163119	58.38 ± 9.57	4.80 ± 3.99	41.65 ± 7.78	46.45 ± 8.36	11.93 ± 5.48	56.72 ± 9.83	43.87 ± 8.00	12.85 ± 5.71
CXOMP J001801.0+163139	28.72 ± 7.43	3.82 ± 3.62	13.39 ± 5.11	17.21 ± 5.79	11.51 ± 5.37	27.78 ± 7.74	15.95 ± 5.46	11.83 ± 5.48
CXOMP J001801.4+163237	22.07 ± 6.94	—	7.49 ± 4.45	7.16 ± 4.74	14.91 ± 5.70	22.85 ± 7.39	4.71 ± 4.15	18.13 ± 6.11
CXOMP J001801.7+163426	82.88 ± 11.03	3.16 ± 3.62	45.22 ± 8.22	48.39 ± 8.63	34.50 ± 7.57	82.30 ± 11.38	40.27 ± 7.86	42.03 ± 8.23
CXOMP J001803.4+162751	19.90 ± 6.68	6.00 ± 3.97	9.22 ± 4.59	15.22 ± 5.58	4.69 ± 4.47	18.23 ± 6.98	13.24 ± 5.23	4.99 ± 4.61
CXOMP J001805.7+162852	19.23 ± 6.20	1.26 ± 2.96	6.74 ± 3.97	8.00 ± 4.45	11.23 ± 4.99	19.67 ± 6.67	5.82 ± 3.98	13.84 ± 5.35
CXOMP J001805.9+163038	17.12 ± 5.90	4.67 ± 3.61	11.77 ± 4.72	16.44 ± 5.46	0.68 ± 3.21	17.45 ± 6.35	16.15 ± 5.34	1.30 ± 3.43
CXOMP J001806.7+162517	11.27 ± 6.17	0.89 ± 3.23	7.36 ± 4.47	8.25 ± 5.03	3.02 ± 4.35	11.72 ± 6.66	7.84 ± 4.76	3.88 ± 4.65
CXOMP J001807.2+163551	38.82 ± 8.18	0.36 ± 2.69	25.97 ± 6.48	26.33 ± 6.66	12.49 ± 5.49	39.55 ± 8.64	22.97 ± 6.19	16.57 ± 6.02
CXOMP J001807.9+163120	101.33 ± 11.39	7.00 ± 3.97	61.62 ± 8.99	68.62 ± 9.48	32.71 ± 7.08	100.71 ± 11.80	55.33 ± 8.61	45.38 ± 8.07
CXOMP J001808.5+163231	81.25 ± 10.44	12.67 ± 4.85	42.57 ± 7.70	55.24 ± 8.68	26.01 ± 6.57	78.86 ± 10.73	48.31 ± 8.13	30.55 ± 7.00
CXOMP J001809.3+162532	88.92 ± 11.02	15.70 ± 5.35	51.19 ± 8.41	66.90 ± 9.55	22.02 ± 6.30	86.98 ± 11.35	62.66 ± 9.25	24.32 ± 6.58
CXOMP J001809.8+162556	25.35 ± 6.77	1.57 ± 2.96	20.07 ± 5.79	21.64 ± 6.10	3.71 ± 3.83	25.49 ± 7.25	13.35 ± 5.12	12.14 ± 5.13
CXOMP J001810.0+163208	23.04 ± 6.39	0.82 ± 2.67	9.52 ± 4.44	10.34 ± 4.73	12.70 ± 4.98	22.70 ± 6.77	8.41 ± 4.29	14.29 ± 5.23
CXOMP J001810.2+162942	22.45 ± 6.29	7.41 ± 3.96	12.53 ± 4.85	19.95 ± 5.78	2.51 ± 3.42	22.60 ± 6.74	18.53 ± 5.56	4.07 ± 3.81
CXOMP J001810.2+163223	269.67 ± 17.61	59.00 ± 8.80	156.73 ± 13.60	215.73 ± 15.80	53.94 ± 8.61	262.20 ± 17.78	189.63 ± 14.85	72.57 ± 9.77
CXOMP J001812.4+162713	19.64 ± 6.00	1.79 ± 2.95	11.01 ± 4.58	12.79 ± 4.99	6.85 ± 4.14	19.69 ± 6.49	12.18 ± 4.86	7.51 ± 4.30
CXOMP J001817.6+163107	34.42 ± 7.07	0.71 ± 2.33	19.76 ± 5.56	20.47 ± 5.67	13.95 ± 4.98	34.42 ± 7.55	16.57 ± 5.22	17.85 ± 5.45
CXOMP J001818.0+163316	43.40 ± 7.85	3.58 ± 3.19	29.63 ± 6.55	33.20 ± 6.90	10.20 ± 4.59	43.56 ± 8.30	29.47 ± 6.55	14.09 ± 5.11
CXOMP J001818.8+163748	21.55 ± 7.04	3.89 ± 3.62	9.83 ± 4.87	13.72 ± 5.60	7.84 ± 5.02	22.37 ± 7.51	11.54 ± 5.12	10.84 ± 5.50
CXOMP J001820.0+162931	11.15 ± 4.72	5.38 ± 3.61	2.48 ± 2.94	7.86 ± 4.13	3.29 ± 3.19	10.25 ± 5.09	7.05 ± 3.97	3.19 ± 3.19
CXOMP J001820.7+162315	12.97 ± 5.92	0.36 ± 2.68	9.16 ± 4.59	9.52 ± 4.87	3.46 ± 4.16	13.21 ± 6.41	8.29 ± 4.60	4.93 ± 4.47
CXOMP J001821.2+163238	6.38 ± 3.79	—	3.81 ± 3.18	3.66 ± 3.18	2.71 ± 2.94	6.43 ± 4.34	2.76 ± 2.94	3.66 ± 3.18
CXOMP J001821.7+161941	138.87 ± 14.31	27.88 ± 6.93	94.16 ± 11.32	122.04 ± 12.87	16.83 ± 7.07	135.98 ± 14.51	116.89 ± 12.43	19.09 ± 7.48

Note. — Col. (1): ChaMP source name given by right ascension in units of hours, minutes, and seconds, and declination in units of degrees, arcminutes, and arcseconds in J2000. Col. (2): net counts and errors in the B (0.3 – 8 keV) band. Col. (3): net counts and errors in the S_1 (0.3 – 0.9 keV) band. Col. (4): net counts and errors in the S_2 (0.9 – 2.5 keV) band. Col. (5): net counts and errors in the S (0.3 – 2.5 keV) band. Col. (6): net counts and errors in the H (2.5 – 8 keV) band. Col. (7): net counts and errors in the Bc (0.5 – 8 keV) band. Col. (8): net counts and errors in the Sc (0.5 – 2 keV) band. Col. (9): net counts and errors in the Hc (2 – 8 keV) band. For detail information about the X-ray photometry, see §3.2. The errors of the net counts are given by following Gehrels statistics (Gehrels 1986). The net counts which are not determined are marked as –. The complete version of this table is in the electronic edition of the *Astrophysical Journal Supplement*. The printed edition contains only a sample.

Table 9. The Supplementary ChaMP X-ray Point Source Photometry

Source Name (1)	B (2)	S_1 (3)	S_2 (4)	S (5)	H (6)	Bc (7)	Sc (8)	Hc (9)
CXOMP J005618.9-272429	16.06 ± 6.51	0.97 ± 2.96	12.10 ± 4.99	13.07 ± 5.36	2.99 ± 4.48	13.88 ± 6.71	7.72 ± 4.45	6.16 ± 5.02
CXOMP J005622.4-272223	40.97 ± 8.15	12.45 ± 4.85	24.58 ± 6.28	37.03 ± 7.48	3.94 ± 4.16	36.65 ± 8.23	30.40 ± 6.82	6.25 ± 4.61
CXOMP J005622.8-272746	14.02 ± 6.43	3.71 ± 3.62	5.99 ± 4.31	9.70 ± 5.14	4.32 ± 4.63	13.42 ± 6.82	7.13 ± 4.61	6.29 ± 5.03
CXOMP J005630.6-273141	32.02 ± 8.48	8.35 ± 4.74	18.61 ± 6.11	26.96 ± 7.27	5.07 ± 5.16	27.21 ± 8.52	20.34 ± 6.50	6.87 ± 5.51
CXOMP J005633.8-272954	59.47 ± 9.69	12.47 ± 4.99	36.54 ± 7.48	49.01 ± 8.56	10.46 ± 5.37	57.77 ± 10.00	46.50 ± 8.28	11.27 ± 5.60
CXOMP J005644.3-274936	14.48 ± 5.91	0.94 ± 2.67	9.03 ± 4.44	9.97 ± 4.73	4.51 ± 4.32	14.06 ± 6.30	9.27 ± 4.44	4.79 ± 4.47
CXOMP J005645.6-272444	10.36 ± 4.58	1.69 ± 2.66	5.59 ± 3.60	7.28 ± 3.97	3.08 ± 3.19	10.36 ± 5.09	7.33 ± 3.97	3.02 ± 3.19
CXOMP J005645.9-275522	85.54 ± 12.10	22.51 ± 6.40	49.65 ± 8.77	72.16 ± 10.43	13.38 ± 6.92	83.65 ± 12.35	64.45 ± 9.75	19.20 ± 7.58
CXOMP J005649.8-273319	17.78 ± 6.50	6.47 ± 4.14	9.74 ± 4.73	16.21 ± 5.80	1.57 ± 3.82	18.91 ± 6.96	16.24 ± 5.57	2.66 ± 4.16
CXOMP J005651.7-272856	36.83 ± 7.48	0.47 ± 2.33	9.79 ± 4.44	10.25 ± 4.58	26.57 ± 6.47	36.98 ± 7.90	7.74 ± 4.13	29.24 ± 6.74
CXOMP J005654.5-275116	10.10 ± 5.49	1.26 ± 2.96	6.44 ± 4.14	7.69 ± 4.60	2.40 ± 3.82	9.72 ± 5.87	8.10 ± 4.45	1.63 ± 3.83
CXOMP J005657.0-274025	45.14 ± 9.17	5.42 ± 4.15	31.94 ± 7.25	37.36 ± 7.94	7.78 ± 5.38	45.96 ± 9.55	33.75 ± 7.41	12.21 ± 6.03
CXOMP J005659.0-274913	10.24 ± 4.73	0.61 ± 2.33	4.96 ± 3.61	5.57 ± 3.80	4.67 ± 3.61	9.39 ± 5.11	5.21 ± 3.61	4.18 ± 3.62
CXOMP J005659.3-272251	10.57 ± 4.43	4.89 ± 3.40	2.84 ± 2.94	7.73 ± 3.96	2.84 ± 2.94	7.62 ± 4.50	2.84 ± 2.94	4.78 ± 3.40
CXOMP J005701.0-272334	4.47 ± 3.41	—	2.84 ± 2.94	2.63 ± 2.94	1.84 ± 2.66	4.57 ± 3.97	2.84 ± 2.94	1.73 ± 2.66
CXOMP J005701.4-274344	7.77 ± 6.99	0.01 ± 3.44	—	—	9.51 ± 6.04	8.43 ± 7.34	—	8.51 ± 6.15
CXOMP J005704.7-280145	83.77 ± 11.30	15.47 ± 5.47	47.30 ± 8.36	62.77 ± 9.57	21.00 ± 6.79	79.52 ± 11.49	57.01 ± 9.08	22.51 ± 7.05
CXOMP J005705.3-274554	6.93 ± 5.15	0.40 ± 2.68	6.46 ± 4.31	6.87 ± 4.61	0.06 ± 3.22	7.56 ± 5.64	6.52 ± 4.31	1.04 ± 3.65
CXOMP J005710.1-274952	40.96 ± 8.09	9.60 ± 4.44	32.81 ± 6.99	42.40 ± 7.85	—	41.69 ± 8.47	39.86 ± 7.55	1.83 ± 3.83
CXOMP J005710.2-274954	24.52 ± 6.18	1.86 ± 2.66	16.65 ± 5.22	18.51 ± 5.45	6.01 ± 3.80	24.52 ± 6.66	16.72 ± 5.22	7.80 ± 4.14
CXOMP J005712.9-272650	4.43 ± 3.41	—	3.91 ± 3.18	3.76 ± 3.18	0.67 ± 2.33	4.43 ± 3.97	1.81 ± 2.66	2.62 ± 2.94
CXOMP J005714.0-272536	2.52 ± 2.94	1.00 ± 2.33	1.86 ± 2.66	2.86 ± 2.94	—	1.52 ± 3.29	0.86 ± 2.33	0.67 ± 2.33
CXOMP J005714.9-271851	15.62 ± 5.10	8.86 ± 4.12	4.95 ± 3.40	13.81 ± 4.84	1.81 ± 2.66	15.67 ± 5.55	12.86 ± 4.71	2.81 ± 2.94
CXOMP J005715.3-271735	9.21 ± 4.29	0.67 ± 2.33	7.86 ± 3.96	8.53 ± 4.13	0.67 ± 2.33	9.35 ± 4.74	8.72 ± 4.13	0.63 ± 2.33
CXOMP J005716.6-273230	33.84 ± 8.46	6.46 ± 4.14	17.39 ± 5.90	23.85 ± 6.76	9.99 ± 5.83	32.67 ± 8.79	19.95 ± 6.20	12.72 ± 6.23
CXOMP J005716.8-272128	24.57 ± 6.08	4.95 ± 3.40	14.86 ± 4.97	19.81 ± 5.56	4.76 ± 3.40	22.62 ± 6.32	17.90 ± 5.33	4.71 ± 3.40
CXOMP J005717.3-274236	29.94 ± 7.34	8.08 ± 4.13	17.73 ± 5.57	25.82 ± 6.47	4.12 ± 4.32	28.27 ± 7.63	23.78 ± 6.18	4.49 ± 4.47
CXOMP J005717.5-272617	19.71 ± 5.56	4.95 ± 3.40	5.95 ± 3.60	10.90 ± 4.43	8.81 ± 4.12	17.71 ± 5.82	5.91 ± 3.60	11.81 ± 4.57
CXOMP J005717.9-271830	34.71 ± 6.98	17.95 ± 5.33	11.95 ± 4.57	29.90 ± 6.55	4.81 ± 3.40	24.71 ± 6.53	18.90 ± 5.45	5.81 ± 3.60
CXOMP J005719.7-272035	4.48 ± 3.40	2.81 ± 2.94	0.95 ± 2.33	3.76 ± 3.18	0.71 ± 2.33	3.52 ± 3.75	2.81 ± 2.94	0.71 ± 2.33

Note. — Col. (1): ChaMP source name given by right ascension in units of hours, minutes, and seconds, and declination in units of degrees, arcminutes, and arcseconds in J2000. Col. (2): net counts and errors in the B (0.3 – 8 keV) band. Col. (3): net counts and errors in the S_1 (0.3 – 0.9 keV) band. Col. (4): net counts and errors in the S_2 (0.9 – 2.5 keV) band. Col. (5): net counts and errors in the S (0.3 – 2.5 keV) band. Col. (6): net counts and errors in the H (2.5 – 8 keV) band. Col. (7): net counts and errors in the Bc (0.5 – 8 keV) band. Col. (8): net counts and errors in the Sc (0.5 – 2 keV) band. Col. (9): net counts and errors in the Hc (2.0 – 8 keV) band. For detail information about the X-ray photometry, see §3.2. The errors of the net counts are given by following Gehrels statistics (Gehrels 1986). The net counts which are not determined are marked as –. The complete version of this table is in the electronic edition of the *Astrophysical Journal Supplement*. The printed edition contains only a sample.

Table 10. The Main ChaMP X-ray Point Source Hardness Ratio and X-ray Colors

Source Name (1)	HR_l68 (2)	HR_mean (3)	HR_u68 (4)	C21_l68 (5)	C21_mode (6)	C21_u68 (7)	C32_l68 (8)	C32_mode (9)	C32_u68 (10)
CXOMP J001709.7+162604	−1.00	−0.46	−0.32	−0.70	−0.22	0.20	−0.10	0.36	0.96
CXOMP J001716.0+162722	−0.53	−0.35	−0.10	−0.45	−0.28	−0.08	0.02	0.23	0.53
CXOMP J001739.7+162330	−0.53	−0.45	−0.37	−0.48	−0.39	−0.32	0.30	0.37	0.51
CXOMP J001743.5+163144	−0.90	−0.54	−0.33	−1.22	−0.70	−0.36	0.04	0.34	0.74
CXOMP J001756.6+163006	−0.53	−0.31	−0.10	−0.66	−0.44	−0.22	0.08	0.28	0.52
CXOMP J001758.4+162647	−0.62	−0.38	−0.14	−0.68	−0.40	−0.14	−0.08	0.14	0.38
CXOMP J001758.9+163119	−0.67	−0.53	−0.40	−1.10	−0.84	−0.62	0.35	0.50	0.68
CXOMP J001801.0+163139	−0.36	−0.15	0.08	−0.76	−0.44	−0.20	−0.14	0.05	0.26
CXOMP J001801.4+163237	0.35	0.54	0.78	−1.20	−0.66	−0.26	−0.50	−0.26	−0.06
CXOMP J001801.7+163426	−0.09	0.02	0.14	−1.32	−1.00	−0.76	0.01	0.10	0.22
CXOMP J001803.4+162751	−0.70	−0.41	−0.14	−0.42	−0.16	0.08	−0.08	0.20	0.54
CXOMP J001805.7+162852	0.17	0.37	0.62	−0.90	−0.44	−0.10	−0.42	−0.20	0.02
CXOMP J001805.9+163038	−0.99	−0.71	−0.63	−0.60	−0.34	−0.12	0.32	0.66	1.14
CXOMP J001806.7+162517	−0.66	−0.26	0.10	−0.96	−0.46	−0.10	−0.12	0.22	0.64
CXOMP J001807.2+163551	−0.33	−0.16	0.03	−1.60	−1.10	−0.78	0.13	0.29	0.47
CXOMP J001807.9+163120	−0.20	−0.10	0.00	−1.08	−0.88	−0.74	0.17	0.27	0.37
CXOMP J001808.5+163231	−0.35	−0.22	−0.12	−0.65	−0.50	−0.37	0.09	0.19	0.32
CXOMP J001809.3+162532	−0.54	−0.43	−0.33	−0.63	−0.48	−0.37	0.23	0.36	0.47
CXOMP J001809.8+162556	−0.26	−0.05	0.17	−1.24	−0.84	−0.56	0.36	0.60	0.92
CXOMP J001810.0+163208	0.04	0.24	0.46	−1.12	−0.66	−0.32	−0.30	−0.12	0.08
CXOMP J001810.2+162942	−0.81	−0.59	−0.42	−0.42	−0.20	−0.02	0.24	0.52	0.90
CXOMP J001810.2+163223	−0.50	−0.44	−0.39	−0.49	−0.42	−0.35	0.39	0.46	0.53
CXOMP J001812.4+162713	−0.46	−0.22	0.01	−0.96	−0.58	−0.28	−0.04	0.18	0.40
CXOMP J001817.6+163107	−0.14	0.04	0.20	−1.48	−1.06	−0.72	−0.01	0.14	0.29
CXOMP J001818.0+163316	−0.49	−0.34	−0.20	−1.06	−0.82	−0.60	0.28	0.43	0.60
CXOMP J001818.8+163748	−0.28	−0.04	0.23	−0.64	−0.32	−0.04	−0.18	0.08	0.34
CXOMP J001820.0+162931	−0.64	−0.32	−0.06	−0.06	0.26	0.58	−0.46	−0.08	0.26
CXOMP J001820.7+162315	−0.56	−0.22	0.11	−1.20	−0.68	−0.32	−0.02	0.28	0.66
CXOMP J001821.2+163238	−0.23	0.11	0.49	−1.28	−0.68	−0.22	−0.20	0.10	0.44
CXOMP J001821.7+161941	−0.79	−0.71	−0.62	−0.62	−0.50	−0.42	0.56	0.68	0.88

Note. — Col. (1): ChaMP source name given by right ascension in units of hours, minutes, and seconds, and declination in units of degrees, arcminutes, and arcseconds in J2000. Col. (2): the 68% lower limit of hardness ratio HR. Col. (3): the mean of hardness ratio (HR=(Hc−Sc)/(Hc+Sc)). Col. (4): the 68% upper limit of hardness ratio HR. Col. (5): the 68% lower limit of color C21. Col. (6): the mode of X-ray color C21 (= $log(S_1/S_2)$). Col. (7): the 68% upper limit of color C21. Col. (8): the 68% lower limit of color C32. Col. (9): the mode of X-ray color C32 (= $log(S_2/H)$). Col. (10): the 68% upper limit of color C32. For detail information about photometry and color determinations, see §3.2. See Table 2 for definition of energy bands. The complete version of this table is in the electronic edition of the *Astrophysical Journal Supplement*. The printed edition contains only a sample.

Table 11. The Supplementary ChaMP X-ray Point Source Hardness Ratio and X-ray Colors

Source Name (1)	HR_l68 (2)	HR_mean (3)	HR_u68 (4)	C21_l68 (5)	C21_mode (6)	C21_u68 (7)	C32_l68 (8)	C32_mode (9)	C32_u68 (10)
CXOMP J005618.9-272429	−0.43	−0.11	0.26	−1.14	−0.70	−0.36	0.10	0.40	0.80
CXOMP J005622.4-272223	−0.80	−0.63	−0.48	−0.44	−0.28	−0.13	0.40	0.64	0.98
CXOMP J005622.8-272746	−0.40	−0.06	0.32	−0.52	−0.16	0.16	−0.28	0.06	0.46
CXOMP J005630.6-273141	−0.71	−0.46	−0.22	−0.54	−0.30	−0.10	0.16	0.42	0.76
CXOMP J005633.8-272954	−0.73	−0.59	−0.47	−0.60	−0.44	−0.30	0.33	0.50	0.70
CXOMP J005644.3-274936	−0.60	−0.29	0.04	−1.08	−0.64	−0.28	−0.08	0.22	0.54
CXOMP J005645.6-272444	−0.68	−0.35	−0.10	−0.76	−0.38	−0.06	−0.10	0.20	0.52
CXOMP J005645.9-275522	−0.66	−0.53	−0.40	−0.46	−0.33	−0.22	0.34	0.51	0.72
CXOMP J005649.8-273319	−0.90	−0.61	−0.44	−0.40	−0.16	0.08	0.12	0.44	0.90
CXOMP J005651.7-272856	0.43	0.55	0.71	−1.26	−0.80	−0.42	−0.58	−0.40	−0.26
CXOMP J005654.5-275116	−0.89	−0.47	−0.24	−0.88	−0.44	−0.06	−0.10	0.24	0.68
CXOMP J005657.0-274025	−0.63	−0.46	−0.29	−0.94	−0.68	−0.48	0.32	0.54	0.78
CXOMP J005659.0-274913	−0.43	−0.10	0.24	−1.00	−0.52	−0.12	−0.26	0.02	0.32
CXOMP J005659.3-272251	−0.08	0.20	0.56	−0.10	0.18	0.50	−0.34	0.00	0.34
CXOMP J005701.0-272334	−0.61	−0.17	0.19	−1.20	−0.58	−0.10	−0.24	0.12	0.50
CXOMP J005701.4-274344	0.40	0.51	1.00	−0.54	0.08	0.74	−1.28	−0.70	−0.26
CXOMP J005704.7-280145	−0.55	−0.42	−0.31	−0.62	−0.45	−0.35	0.21	0.35	0.48
CXOMP J005705.3-274554	−0.93	−0.44	−0.23	−1.08	−0.56	−0.16	0.08	0.48	1.02
CXOMP J005710.1-274952	−0.99	−0.84	−0.80	−0.66	−0.50	−0.34	0.88	1.24	1.80
CXOMP J005710.2-274954	−0.54	−0.34	−0.16	−1.10	−0.78	−0.52	0.20	0.40	0.60
CXOMP J005712.9-272650	−0.24	0.12	0.58	−1.30	−0.70	−0.24	0.04	0.42	0.90
CXOMP J005714.0-272536	−0.62	−0.04	0.50	−0.62	−0.16	0.26	−0.06	0.46	1.08
CXOMP J005714.9-271851	−0.81	−0.57	−0.43	0.00	0.22	0.46	0.00	0.32	0.68
CXOMP J005715.3-271735	−1.00	−0.70	−0.63	−1.14	−0.68	−0.32	0.32	0.68	1.14
CXOMP J005716.6-273230	−0.43	−0.22	0.01	−0.62	−0.38	−0.18	−0.02	0.20	0.44
CXOMP J005716.8-272128	−0.74	−0.54	−0.40	−0.64	−0.42	−0.22	0.22	0.44	0.66
CXOMP J005717.3-274236	−0.85	−0.63	−0.47	−0.50	−0.32	−0.14	0.24	0.50	0.84
CXOMP J005717.5-272617	0.11	0.30	0.54	−0.32	−0.06	0.18	−0.38	−0.16	0.06
CXOMP J005717.9-271830	−0.68	−0.49	−0.35	0.01	0.17	0.32	0.14	0.34	0.58
CXOMP J005719.7-272035	−0.89	−0.37	−0.12	−0.10	0.28	0.74	−0.48	0.02	0.56

Note. — Col. (1): ChaMP source name given by right ascension in units of hours, minutes, and seconds, and declination in units of degrees, arcminutes, and arcseconds in J2000. Col. (2): the 68% lower limit of hardness ratio HR. Col. (3): the mean of hardness ratio (HR=(Hc−Sc)/(Hc+Sc)). Col. (4): the 68% upper limit of hardness ratio HR. Col. (5): the 68% lower limit of color C21. Col. (6): the mode of X-ray color C21 (= $log(S_1/S_2)$). Col. (7): the 68% upper limit of color C21. Col. (8): the 68% lower limit of color C32. Col. (9): the mode of X-ray color C32 (= $log(S_2/H)$). Col. (10): the 68% upper limit of color C32. For detail information about photometry and color determinations, see §3.2. See Table 2 for definition of energy bands. The complete version of this table is in the electronic edition of the *Astrophysical Journal Supplement*. The printed edition contains only a sample.

Table 12. Statistical Summary of the ChaMP X-ray Point Sources

		ALL					$S/N > 2.0$				
	Band	Number	Min	Max	Median	Mean	Number	Min	Max	Median	Mean
	(1)	(2)	(3)	(4)	(5)	(6)	(7)	(8)	(9)	(10)	(11)
Count[a]	B	6755	0.04	40535.59	21.03	68.05	5407	8.00	40535.59	28.14	83.49
	S	6696	0.00	38117.52	15.46	54.70	4561	7.94	38117.52	25.66	77.89
	H	6221	0.00	11604.93	5.87	15.12	1914	8.28	11604.93	18.02	39.16
	Bc	6736	0.20	39760.98	20.53	65.33	4950	9.53	39760.98	30.05	86.45
	Sc	6634	0.01	36010.96	13.52	48.23	4245	7.94	36010.96	24.27	72.73
	Hc	6401	0.00	13624.92	7.16	18.85	2406	8.33	13624.92	18.88	42.24
Flux[b]	B	6755	0.01	6484.14	7.97	23.10	5407	0.80	6484.14	10.04	27.52
	S	6696	0.00	3482.36	3.92	12.19	4561	0.45	3482.36	5.96	16.71
	H	6221	0.00	6326.57	5.08	12.78	1914	1.89	6326.57	11.09	26.93
	Bc	6736	0.02	5882.11	7.34	20.90	4950	0.94	5882.11	9.96	26.47
	Sc	6634	0.00	2470.09	2.64	8.27	4245	0.37	2470.09	4.28	11.90
	Hc	6401	0.00	6673.65	5.65	14.10	2406	1.65	6673.65	11.10	26.59
Exp.	B	6755	0.71	123.63	33.91	39.82	5407	0.86	123.63	36.67	42.30
Time[c]	S	6696	0.71	123.63	33.95	39.81	4561	0.86	123.63	36.84	42.51
	H	6221	0.71	123.63	34.76	40.57	1914	2.04	123.63	42.98	52.65
	Bc	6736	0.71	123.63	33.95	39.83	4950	0.90	123.63	37.70	43.30
	Sc	6634	0.71	123.63	33.98	39.87	4245	0.86	123.63	37.57	43.22
	Hc	6401	0.71	123.63	34.41	40.23	2406	1.21	123.63	41.67	50.59
OAA[d]	B	6755	0.05	23.26	5.40	6.13	5407	0.05	23.23	5.98	6.55
	S	6696	0.05	23.26	5.42	6.15	4561	0.05	23.23	6.22	6.80
	H	6221	0.05	23.26	5.47	6.16	1914	0.06	23.23	6.23	6.76
	Bc	6736	0.05	23.26	5.40	6.13	4950	0.05	23.23	6.15	6.71
	Sc	6634	0.05	23.26	5.44	6.16	4245	0.05	23.23	6.34	6.91
	Hc	6401	0.05	23.23	5.45	6.15	2406	0.06	23.23	6.24	6.76
	HR	6795	-0.99	0.96	-0.36	-0.28	2005	-0.96	0.76	-0.35	-0.31
	C21	6795	-1.80	1.36	-0.41	-0.40	1606	-1.47	0.78	-0.28	-0.27
	C32	6795	-1.36	2.30	0.32	0.29	1650	-0.87	1.73	0.35	0.32

Note. — Col. (1): X-ray energy band. Col. (2)-(6): the statistical properties of all ChaMP X-ray point sources. Col. (7)-(11): the statistical properties of sources with $S/N > 2.0$.

[a]Source Counts

[b]Source Flux with $\Gamma_{ph} = 1.7$ in units of 1×10^{-15} *erg cm*$^{-2}$ *sec*$^{-1}$

[c]Effective Exposure Time in units of *ksec*

[d]Off axis angle in units of arcminutes

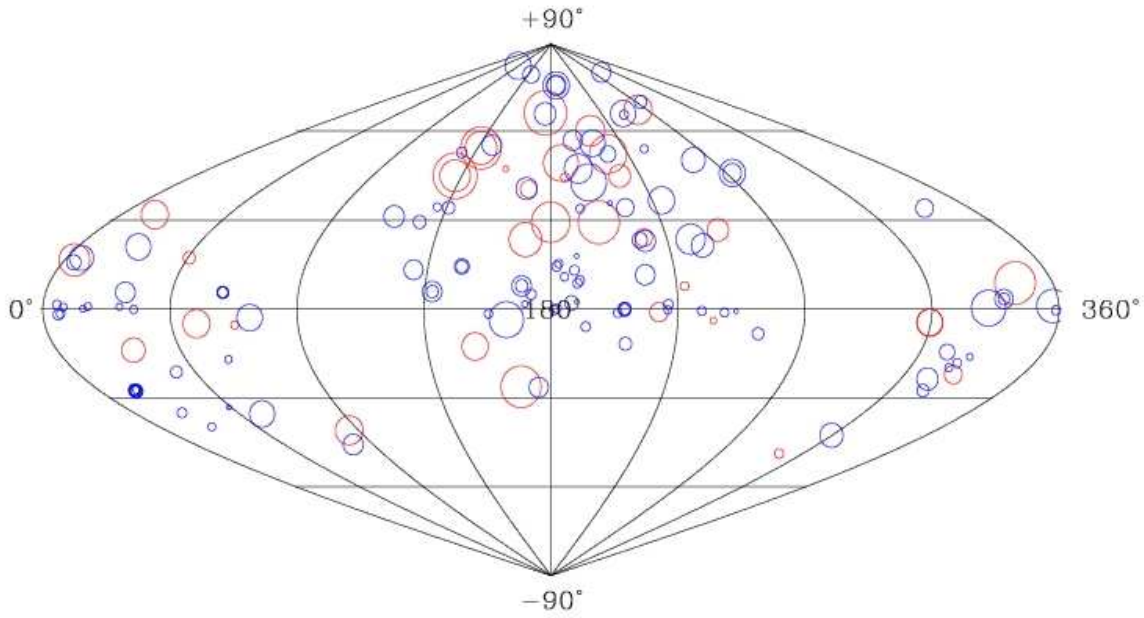

Fig. 1.— The location of 149 ChaMP fields in equatorial coordinates. Red circles represent ACIS-I at the aim point, and blue circles ACIS-S. The circle size crudely indicates the Chandra exposure time, ranging from 0.9 to 124 ksecs. The ChaMP fields are uniformly distributed over the celestial space except (by selection) the Galactic plane region.

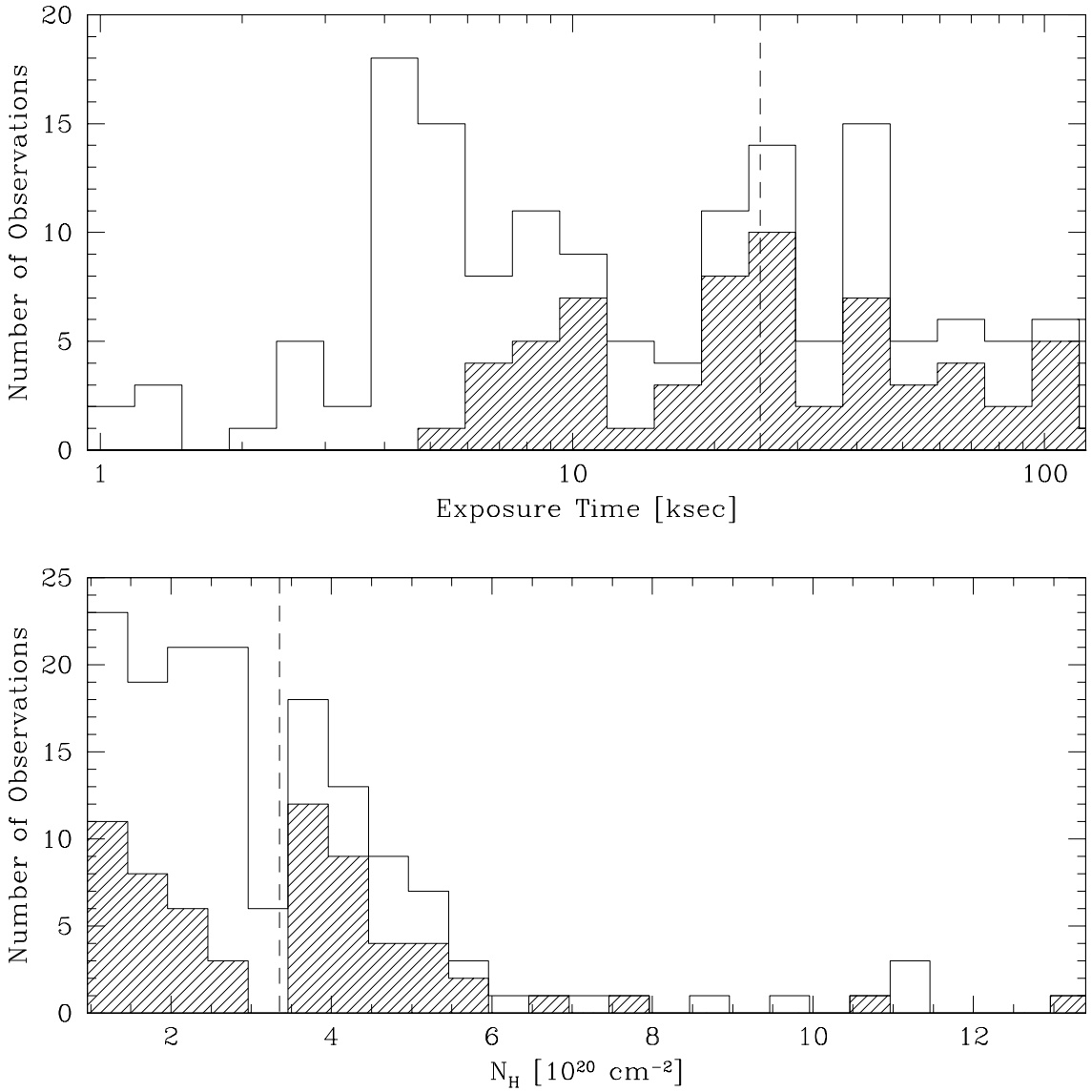

Fig. 2.— The number distribution of effective exposure times (*top*) and Galactic extinction, N_H (*bottom*) of the 149 ChaMP observations. The dashed line indicates the mean of each number distribution. The mean exposure time of the ChaMP is ~ 25 *ksec* and the mean Galactic extinction in the ChaMP is $N_H \sim (3.4 \pm 2.2) \times 10^{20}\ cm^{-2}$. The ChaMP fields range from short to long exposure times and their Galactic absorption is lower than the Galactic plane ($N_H \sim 10^{22} \sim 10^{23}\ cm^{-2}$). The number distributions of the 62 ChaMP fields from Paper I are displayed as shaded histograms.

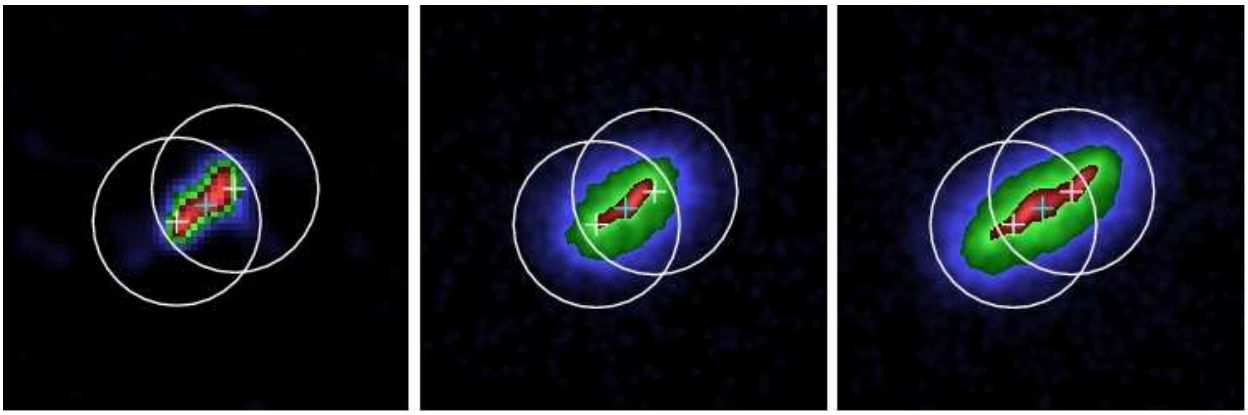

Fig. 3.— The large overlapping double X-ray sources detected by *wavdetect* (*left*), the PSF image at their median location (*middle*), and the combined image of two PSFs at each X-ray source position (*right*). The white crosses and circles mark the positions and sizes of the double sources. The cyan crosses indicate the median location of the double sources. Circle size corresponds to the source extraction region used in *xapphot*. The shape of the detected overlapping X-ray sources (*left*) are similar to the shape of the single PSF (*middle*), rather than double PSFs (*right*). We conclude that the overlapping X-ray sources are spurious doubles due to the elongated PSF shape and sub-structures in the PSF. The PSF images are generated by the *ChaRT* tool in the CIAO package and MARX package. The size of all images is $\sim 30'' \times 30''$ and all images are aligned with the world coordinate system.

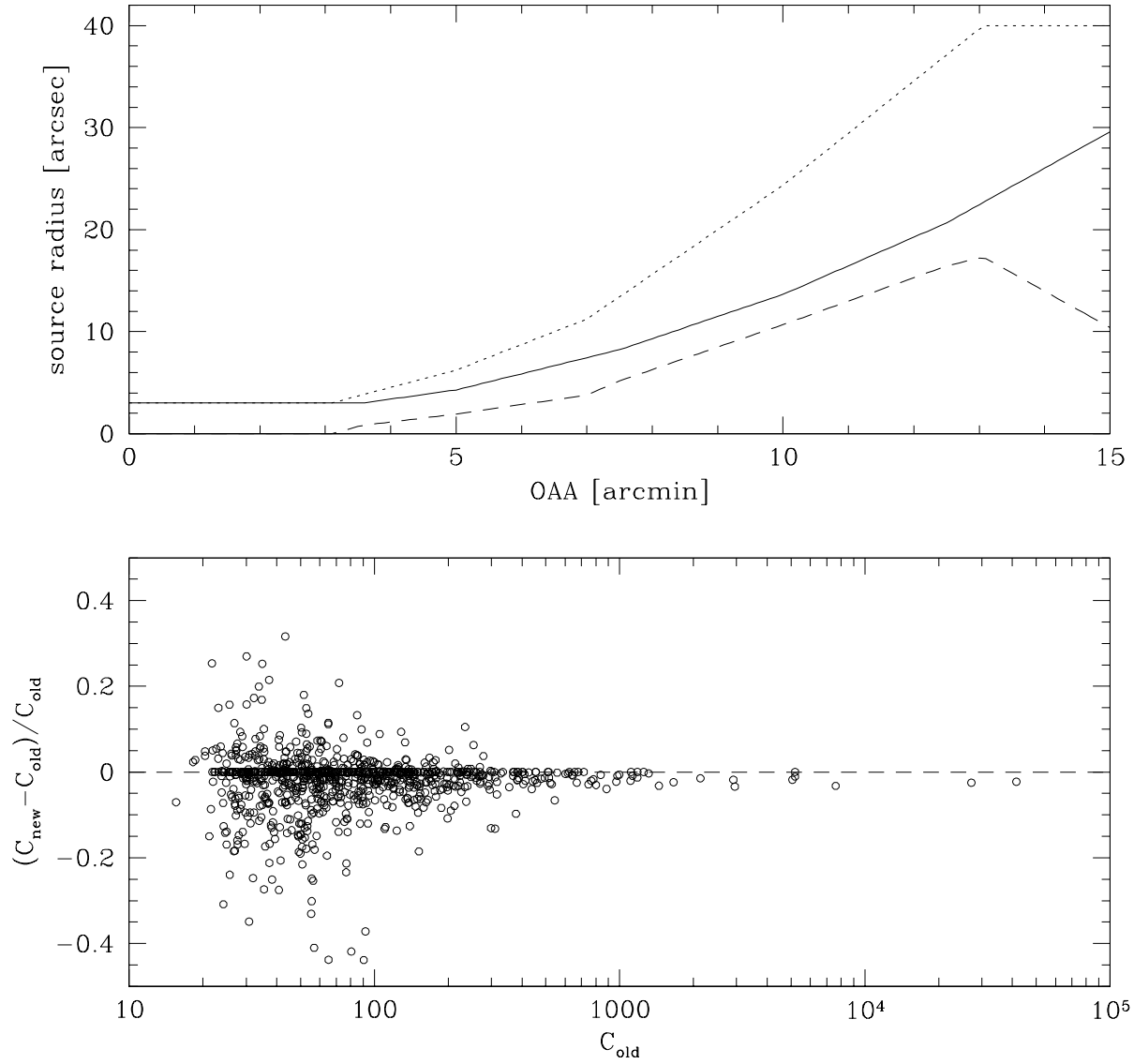

Fig. 4.— *top*. Source extraction radius as a function of off-axis angle. The dotted line represents the source radius from the old version of the CIAO CALDB used in the previous ChaMP catalog (Paper I). The solid line represents the source radius from the latest version of the CIAO CALDB used in this catalog. The source size is limited to a minimum radius of $3''$ and a maximum of $40''$. The difference between the two radii is plotted as a dashed line. *bottom*. The difference between the source counts in this and the previous catalog as a function of the previous counts. On average the reduced source radius yields source counts lower by $\sim 2 \pm 7\%$ in this catalog. The dashed line indicates the zero difference level.

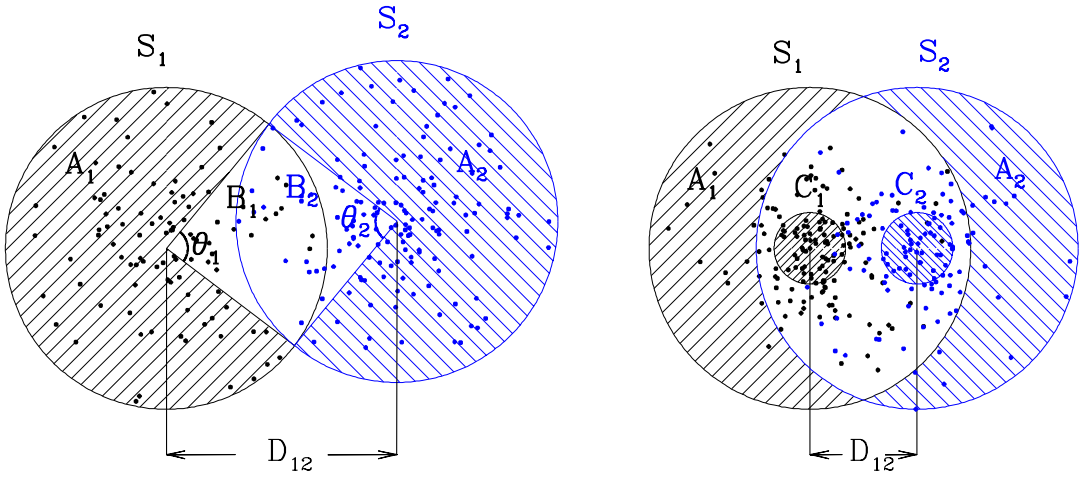

Fig. 5.— Schematic diagrams of the two types of overlapping X-ray source pairs, small (*left*) and large (*right*). S_1 and S_2 represent the source1 and source2, respectively. A_1 and A_2 represent the independent area of each source. θ_1 and θ_2 represent the angles covered by sectors B_1, and B_2 of overlapping regions of two sources, respectively. C_1 and C_2 represent the core regions of large overlapping sources, respectively. D_{12} represents the distance between S_1 and S_2. The points are simulated X-ray events assuming a β model for the event distribution. For the small overlapping case, only the photons in regions A_1 and A_2 are used to determine the correction, while the photons in regions $A's$ and $C's$ are used in the large overlapping case. The detailed correction method of *xapphot* is described in the text.

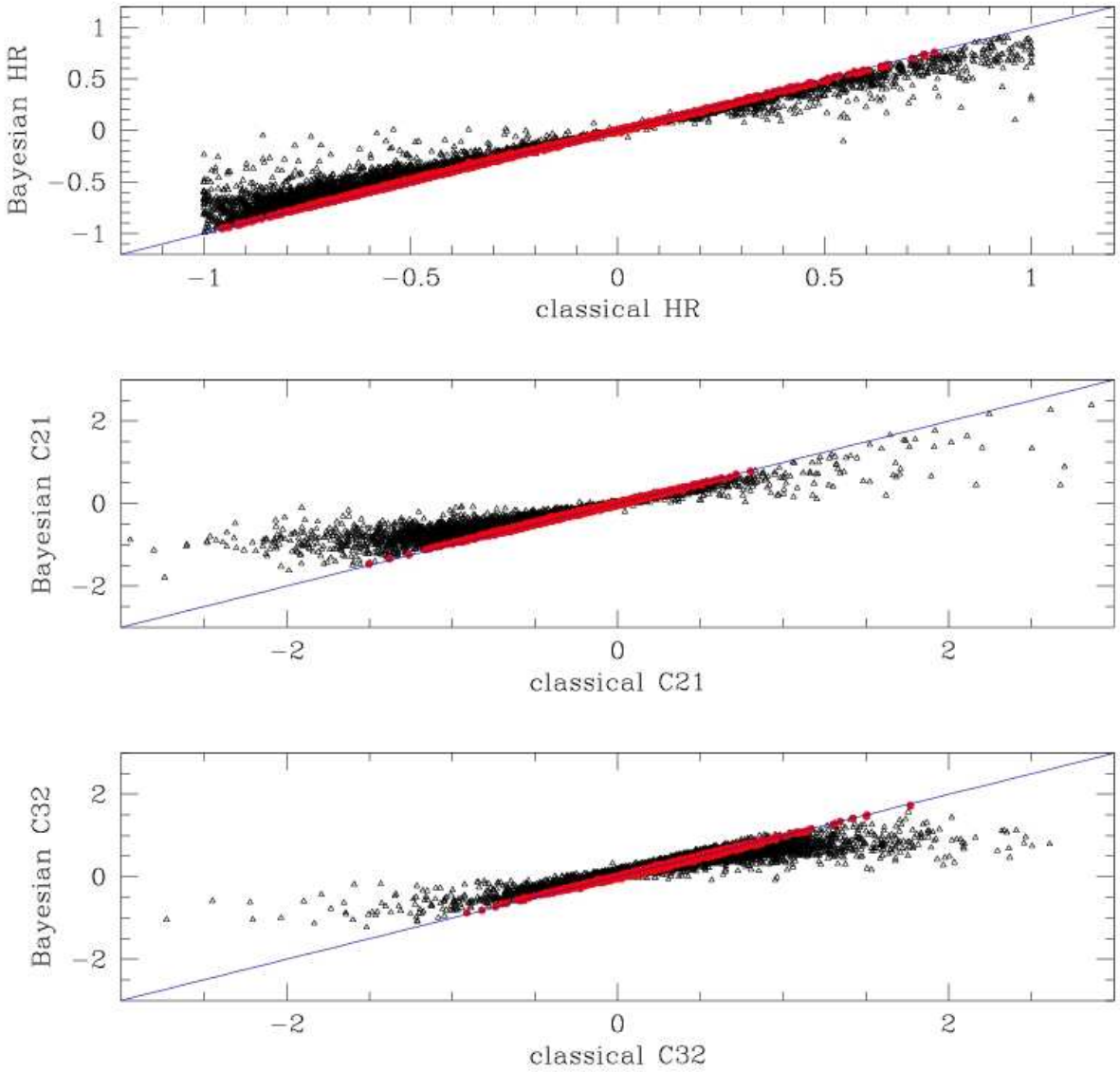

Fig. 6.— Comparison of a classical with a Bayesian method for HR (*top*), C21 (*middle*), and C32 (*bottom*). The sources with *net counts* ≥ 0 (*net counts* > 0) for HR (X-ray colors) in both energy bands are plotted. The black open triangles represent the sources with $S/N < 2$ in at least one energy band. The red closed circles represent the sources with $S/N > 2$ in two energy bands. The blue line represents the line of equality for the two methods and is shown for illustrative comparison. For bright sources ($S/N > 2$), the HR and X-ray colors from both methods agree well; however, for faint sources ($S/N < 2$), they do not agree, because the classical method, using Gaussian statistics, fails to describe the nature of faint sources.

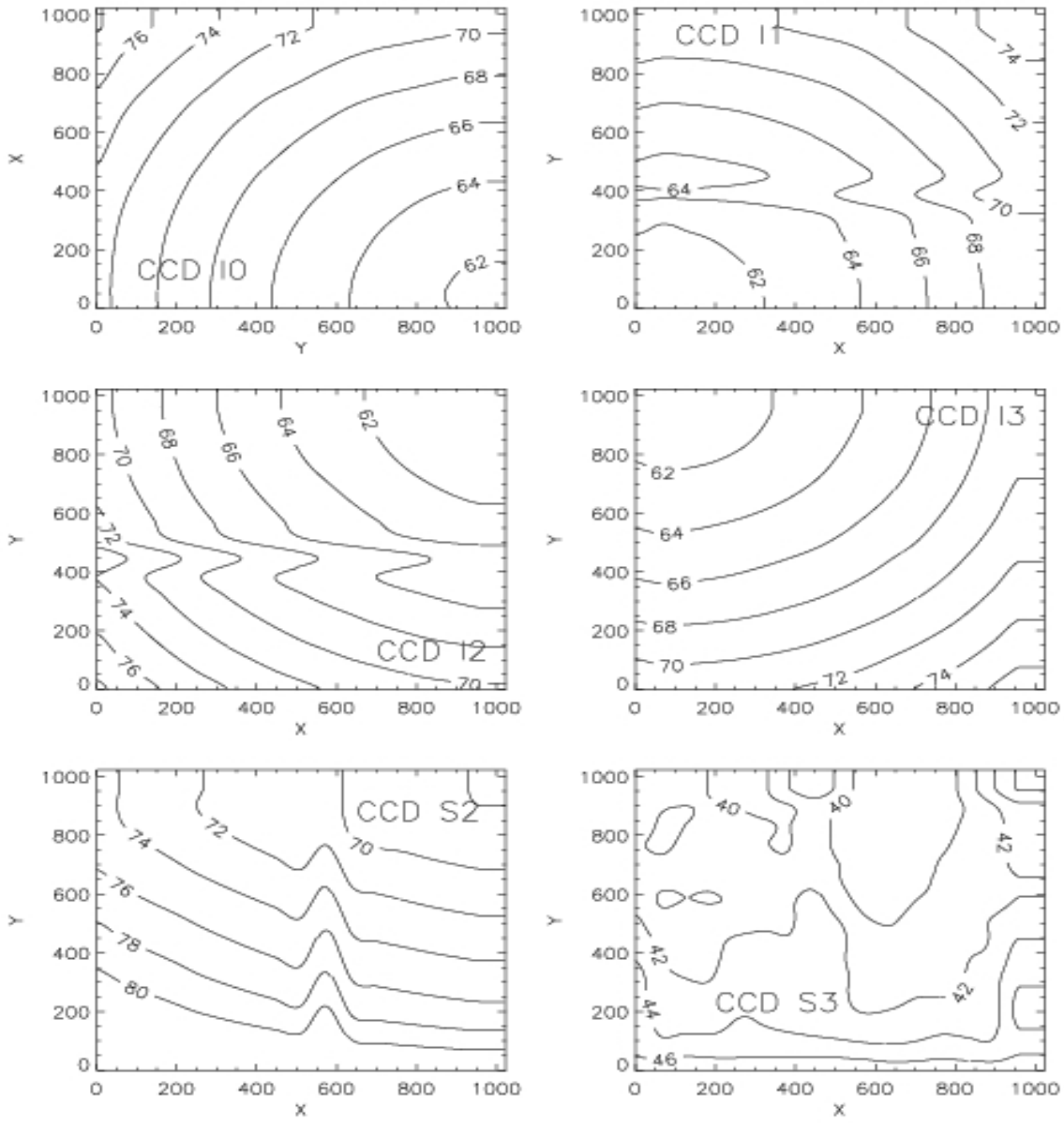

Fig. 7.— Contour maps of the energy conversion factors (*ECF*) in ACIS-I observations including ACIS-S S2 and S3 CCD chips. Figures are shown in chip coordinates rotated by 90° (CCD I1 and I3) and 270° (CCD I0 and I2) relative to CCD S3. The energy band is 0.3-2.5 keV and a photon index of $\Gamma_{ph} = 1.7$ was assumed. The *ECF*s are calculated at 16×16 grid points with a grid size of 32 pixels and smoothed with a cubic kernel. The *ECF* is in units of *erg* cm^{-2} *count*$^{-1}$.

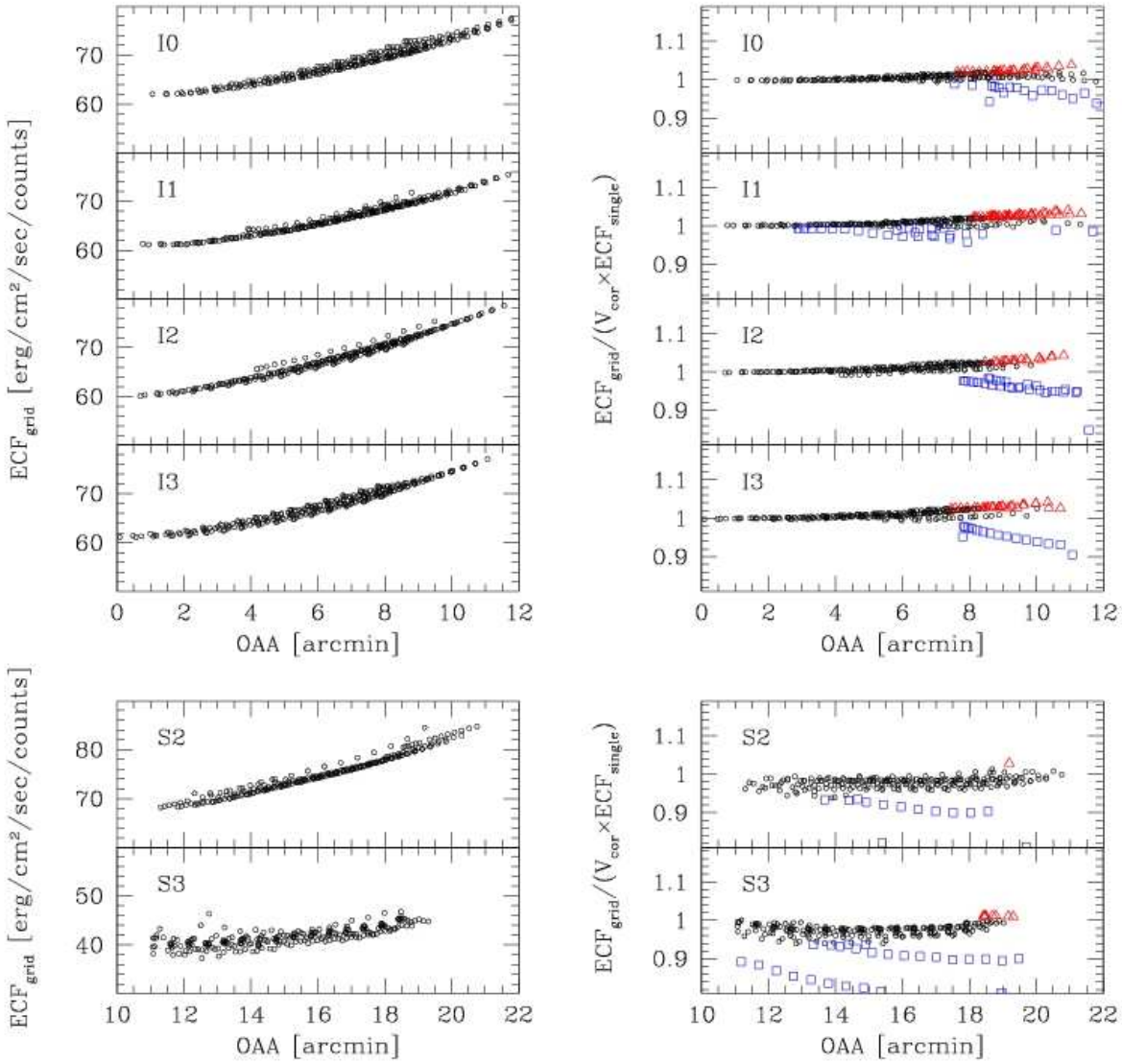

Fig. 8.— *left*. The spatial variations of the ECF_{grid} in the S band as a function of off axis angle in each CCD chip observed with ACIS-I including S2 and S3 CCD chips. The aim point of this observation is located on the I3 CCD chip, so the off axis angle of S2 and S3 chips is large. ECF_{grid} varies by at most $\sim 25\%$ depending on position in each CCD chip. *right*. The ratios of ECF_{grid} to the vignetting corrected ECF_{single}. Blue squares are caused by the exposure map defects such as a CCD chip edge or bad pixel strip effect. Red triangles are caused by lower quantum efficiency at larger off axis angles. The mean ratio is 1.00 ± 0.02 in the I0-I3 chips and 0.98 ± 0.02 and 0.97 ± 0.03 in the S2 and S3 chips.

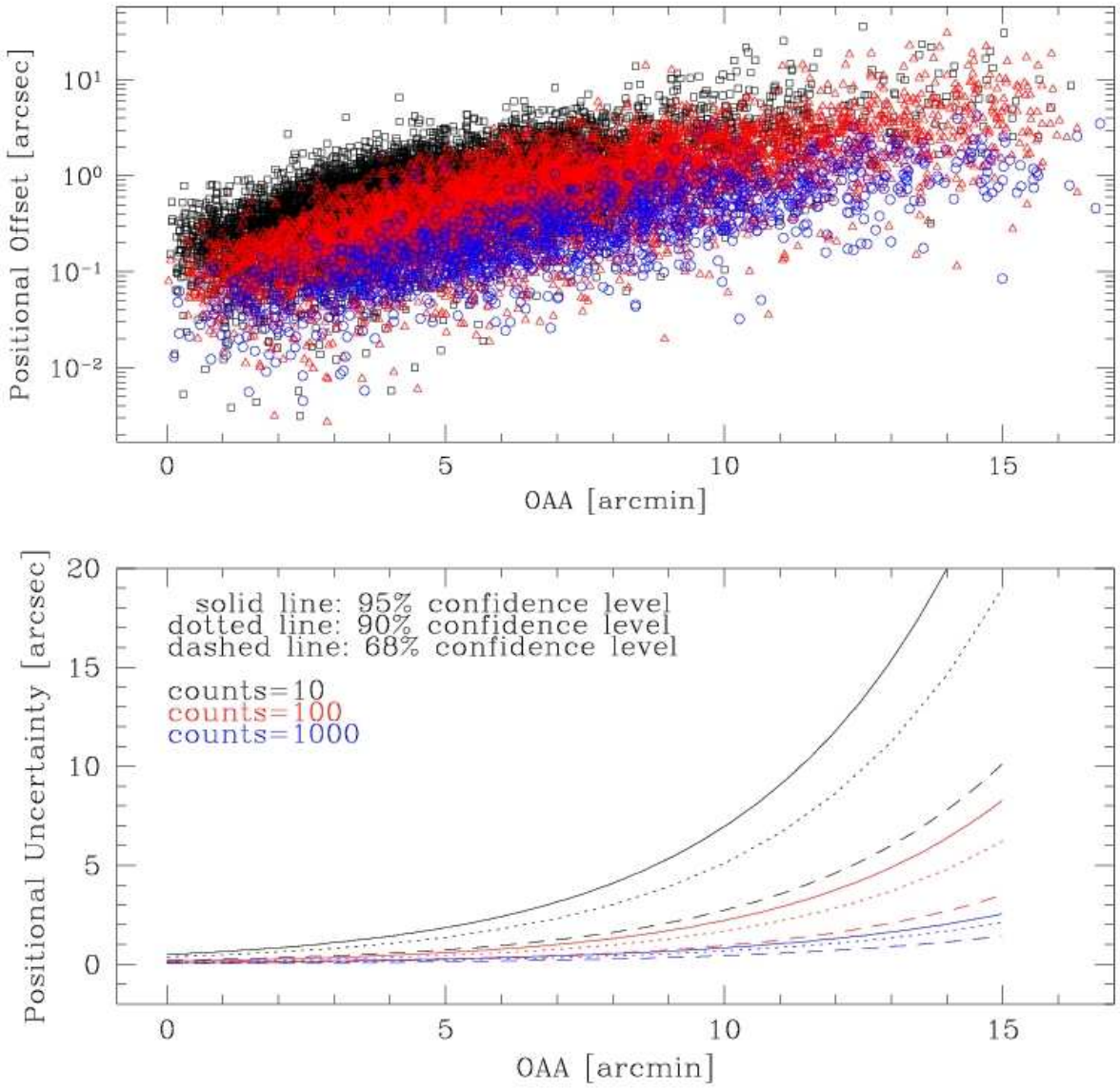

Fig. 9.— *top*. The positional offset of the artificial sources in three source count ranges as a function of off-axis angle. The black squares, red triangles, and blue circles represent artificial sources with count ranges of $0 < logC < 1.2$, $1.2 < logC < 2$, and $logC > 2$, respectively. The positional offset exponentially increases with off axis angle, and decreases as the source counts increase with a power law form. *bottom*. The positional uncertainties from the derived equations (see equation (12), (13), and (14) in §4.2.1) as a function of off axis angle for 10 source counts (*black*), 100 source counts (*red*), and 1,000 source counts (*blue*), respectively. The solid, dotted, and dashed lines represent the positional uncertainty at 95%, 90%, and 68% confidence levels, respectively.

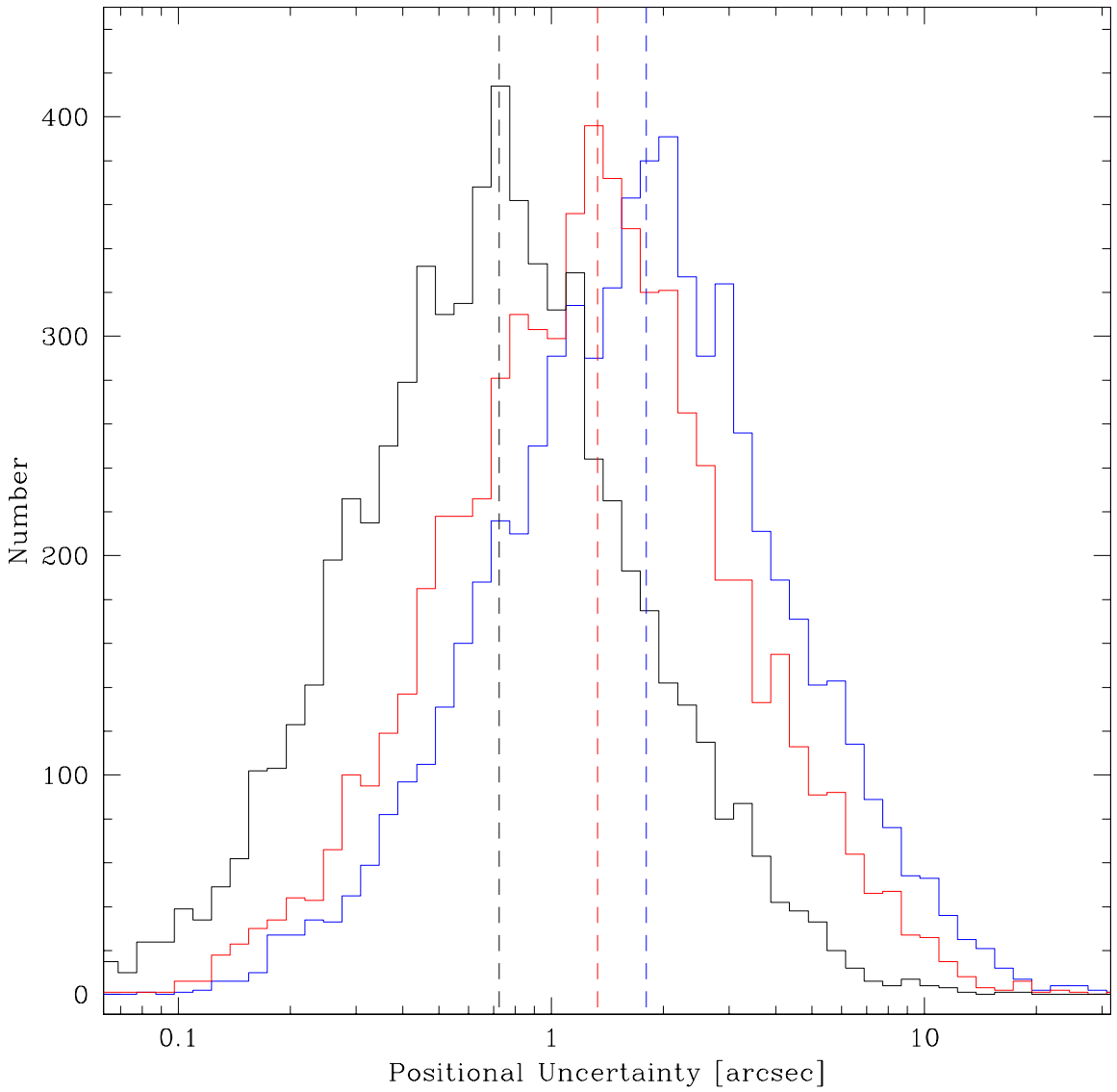

Fig. 10.— The number distributions of positional uncertainty of all ChaMP X-ray point sources estimated from our empirical positional uncertainty equations. Black, red, and blue histograms show the 68%, 90%, and 95% confidence level of positional uncertainty distributions, respectively. The median positional uncertainties for all sources are plotted as dashed lines and shown at $0.7 \pm 0.45''$, $1.3 \pm 0.8''$, and $1.8 \pm 1.1''$, respectively.

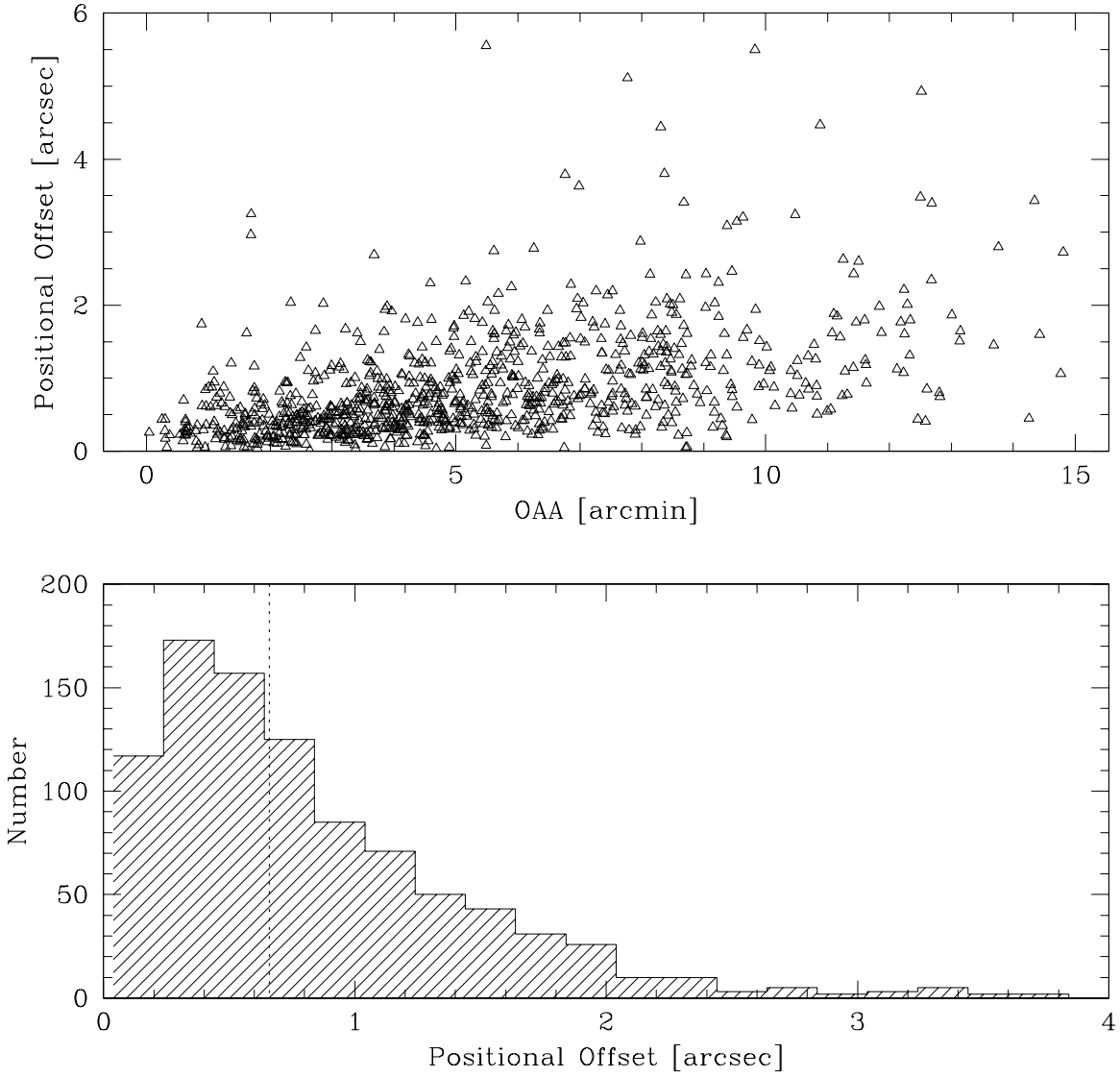

Fig. 11.— *top*. Positional offset between the matched ChaMP and *SDSS* sources as a function of off-axis angle. *bottom*. The number distribution of the positional offset between the matched ChaMP and the *SDSS* sources. The median positional offset is $0.7 \pm 0.4''$ and is denoted by the dotted line.

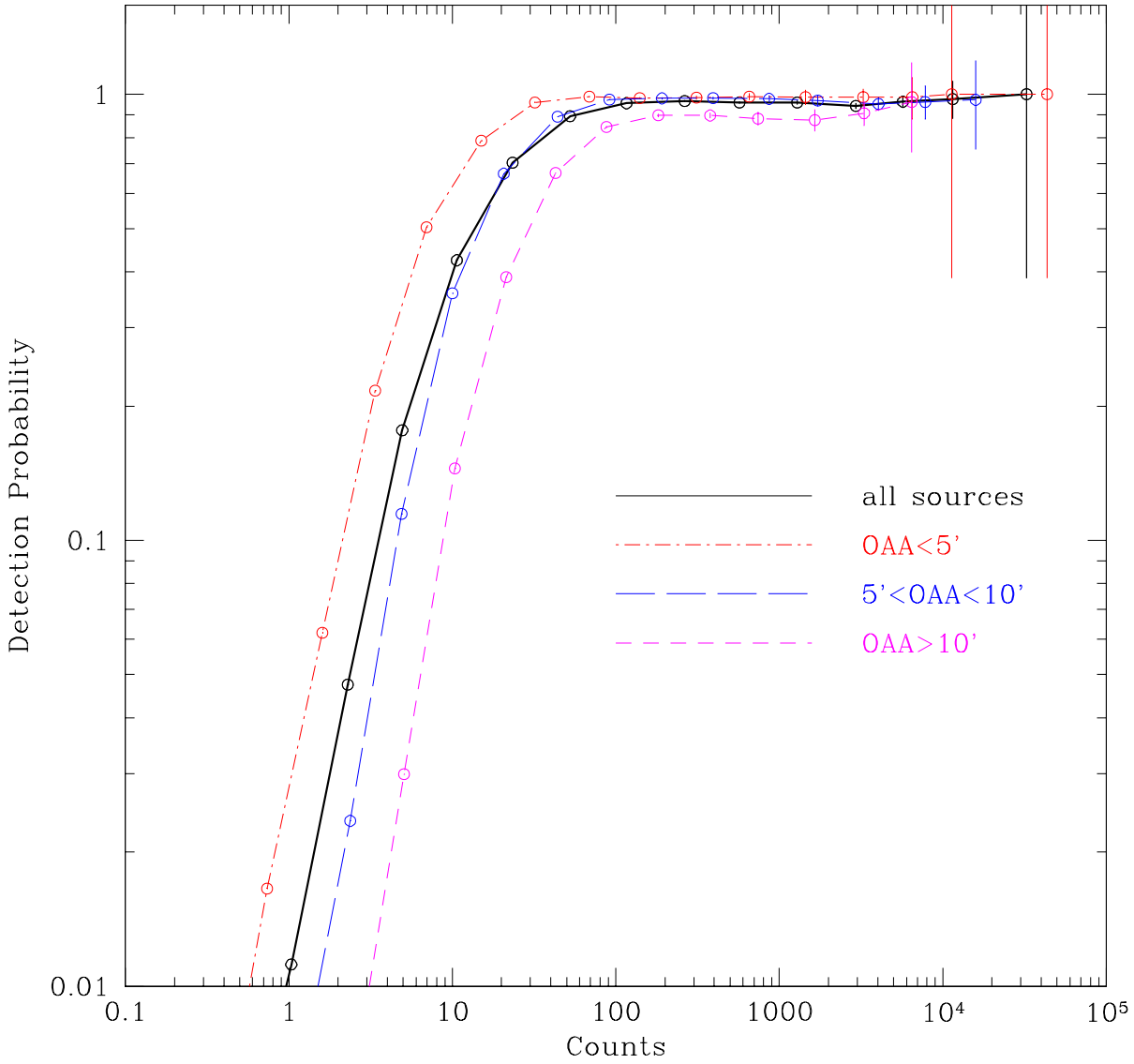

Fig. 12.— The detection probability of a source in the ChaMP catalog as a function of B band counts. The thick solid line represents the detection probability of all sources. The red dot dashed, blue long dashed, and magenta short dashed lines denote the detection probability of sources located at off axis angles, $OAA < 5'$, $5' < OAA < 10'$, and $OAA > 10'$, respectively. As expected, the detection probability decreases as the off axis angle increases.

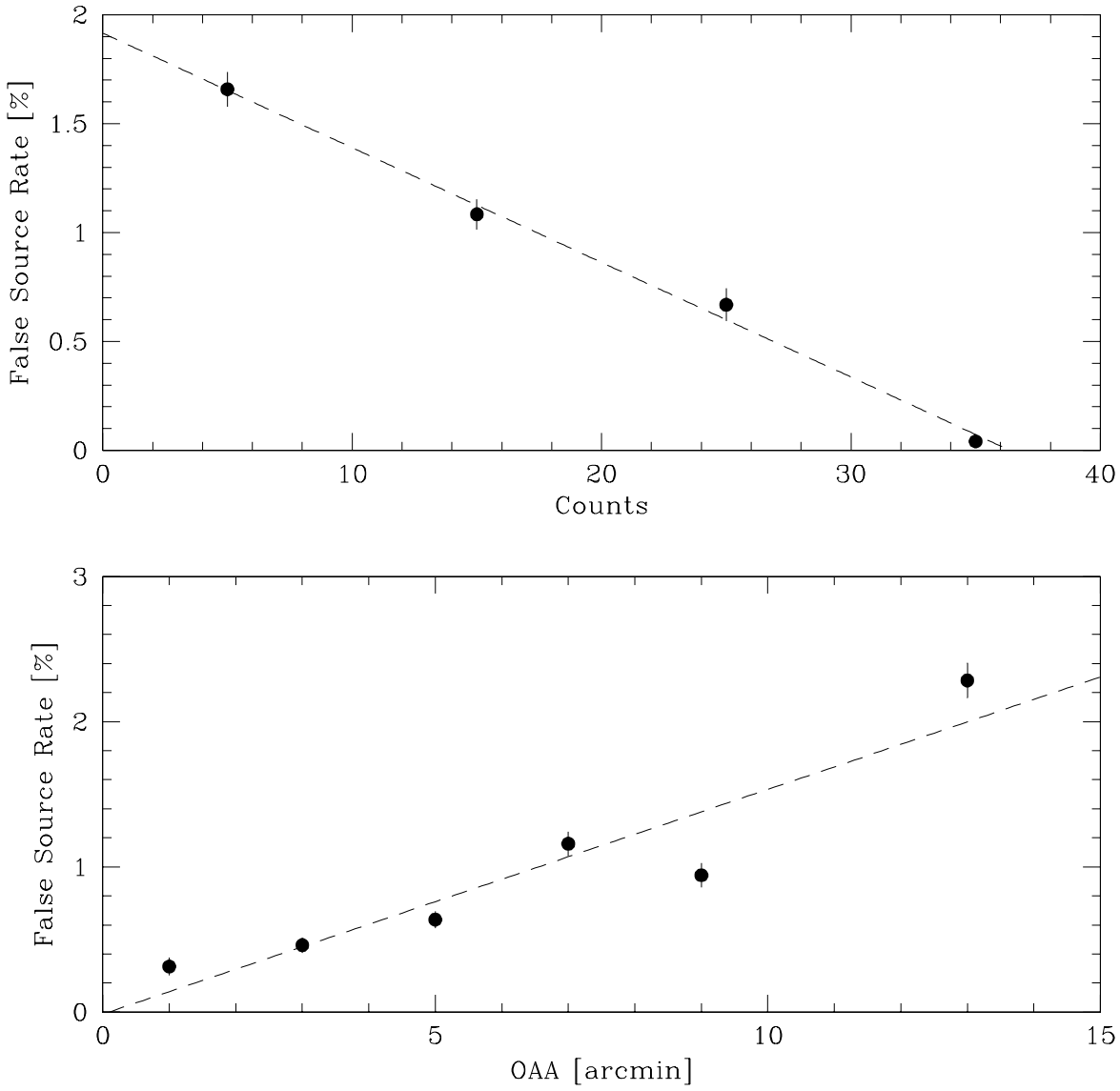

Fig. 13.— The false source detection rate as a function of source counts in the B band extracted by *wavdetect* (*top*) and off axis angle (*bottom*). $\sim$ 1% of the total detected sources are spurious sources and 80% of spurious sources have counts less than $\sim$ 30. The false source detection rate increases as the source counts decrease and as the off axis angle increases. The dashed lines indicate the best linear least square fit results (see §4.3.2).

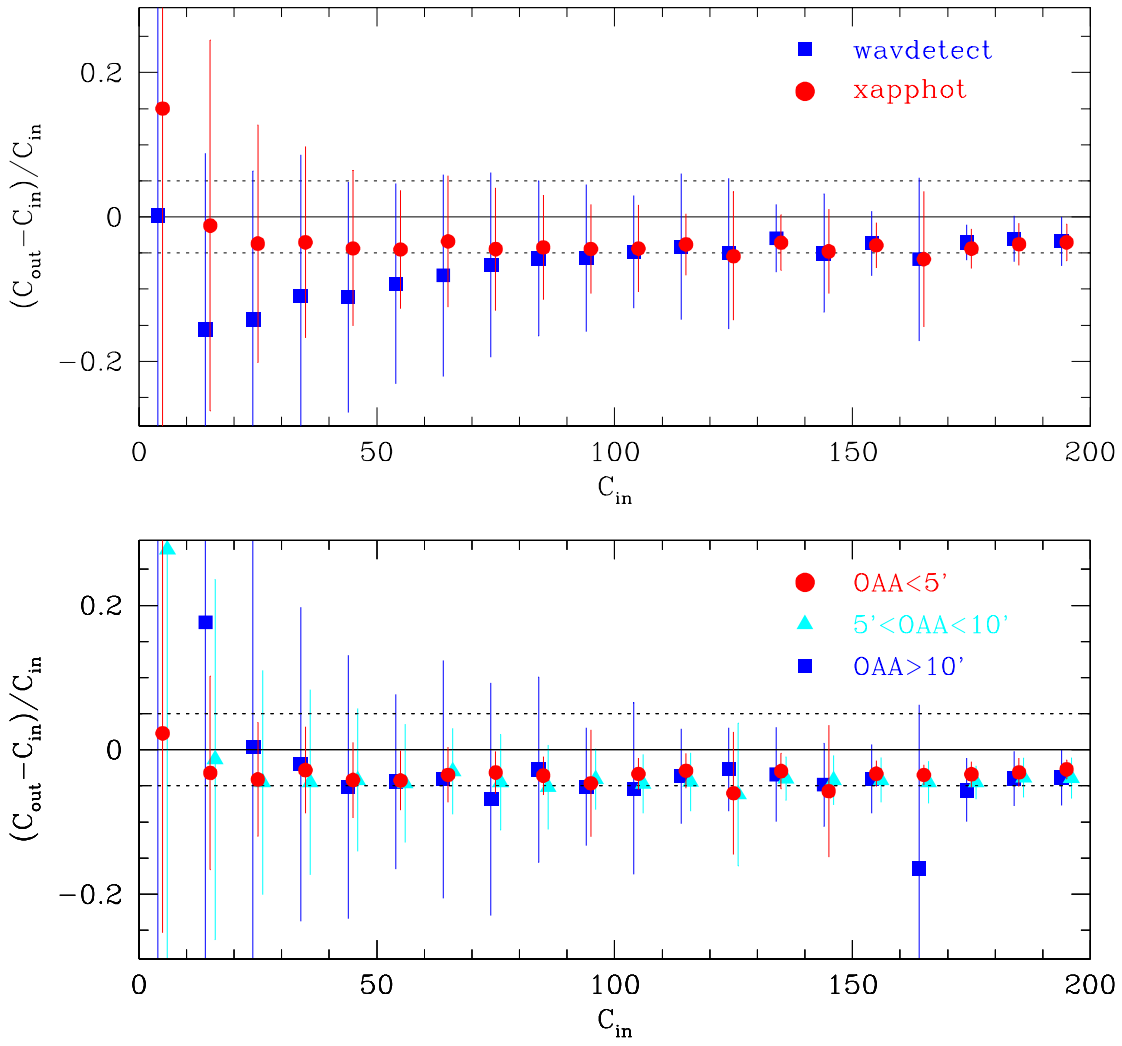

Fig. 14.— The count recovery rate as a function of input counts. *top*. Comparison of the count recovery rate from *xapphot* (*red circles*) with that from *wavdetect* (*blue squares*). Both *xapphot* and *wavdetect* recover the true counts well ($96 \pm 1\%$ level for *xapphot* and $94 \pm 3\%$ level for *wavdetect*), however, for source counts fainter than ~ 50, *wavdetect* recovers only $87 \pm 2\%$ of the true counts. Note that Eddington bias is visible in the first points of both *wavdetect* and *xapphot* count recovery rates. *bottom*. The count recovery rates of sources with $OAA < 5'$ (*red circle*), $5' < OAA < 10'$ (*cyan triangle*), and $OAA > 10'$ (*blue square*), respectively. Source counts are extracted using *xapphot*. As the off axis angle increases the uncertainty in the count recovery rate increases.

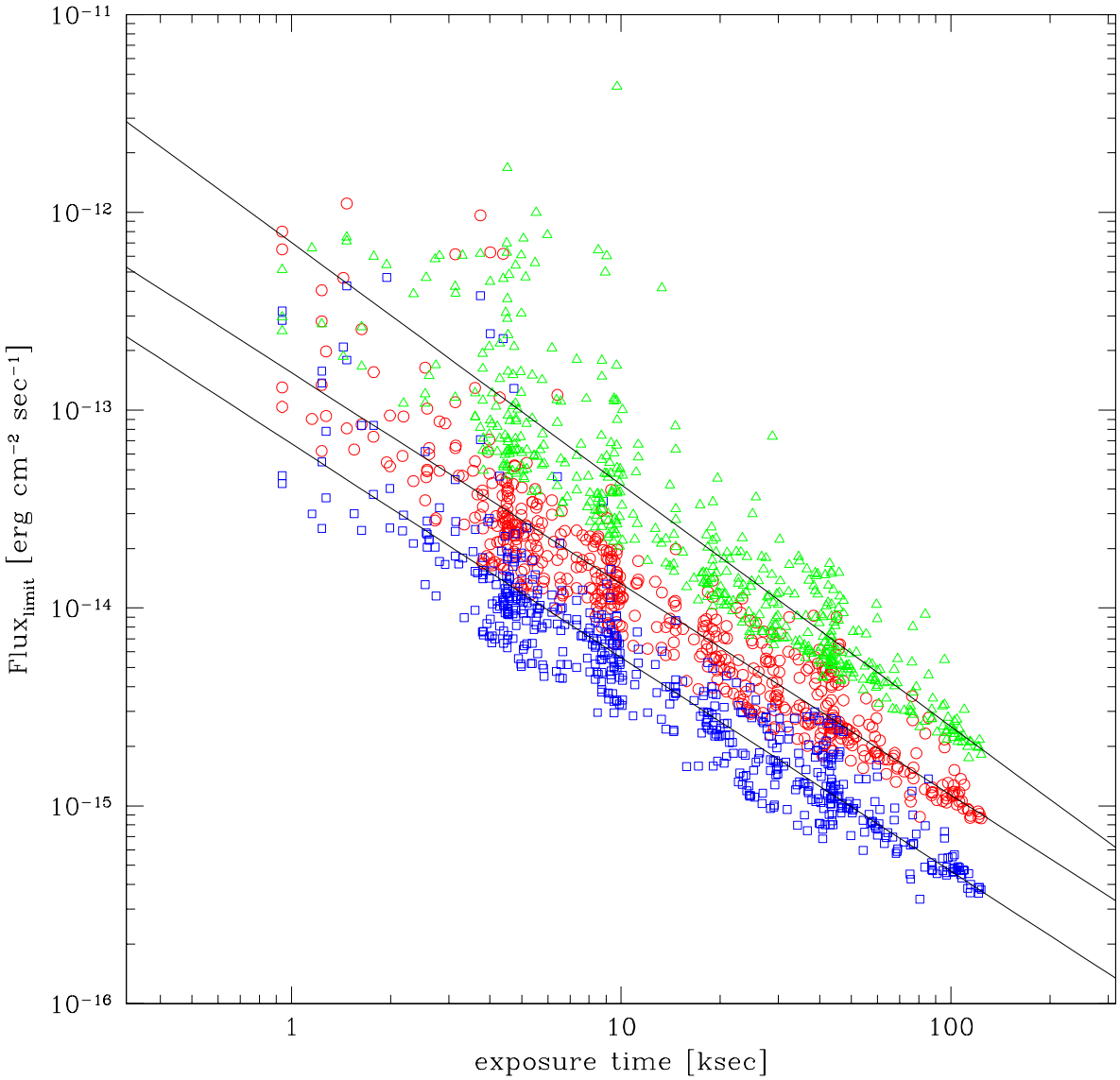

Fig. 15.— The flux limits of detected X-ray point sources in the ChaMP fields as a function of net exposure time. Four CCD chips (I0, I1, I2, and I3 for ACIS-I observations, and I2, I3, S2, and S3 for ACIS-S observations) per ChaMP field and the 130 ChaMP fields were used. Detected artificial X-ray point sources with $S/N > 2.0$ are selected in each CCD chip and their minimum flux is defined as the flux limit of that CCD chip. Red circles, blue squares, and green triangles represent the Bc, Sc, and Hc bands, respectively. The solid lines represent the best linear least squares fit results in each energy band. The scatter is caused by the varying sensitivity and detection probability of each CCD chip and observation. A photon index of $\Gamma_{ph} = 1.7$ was assumed.

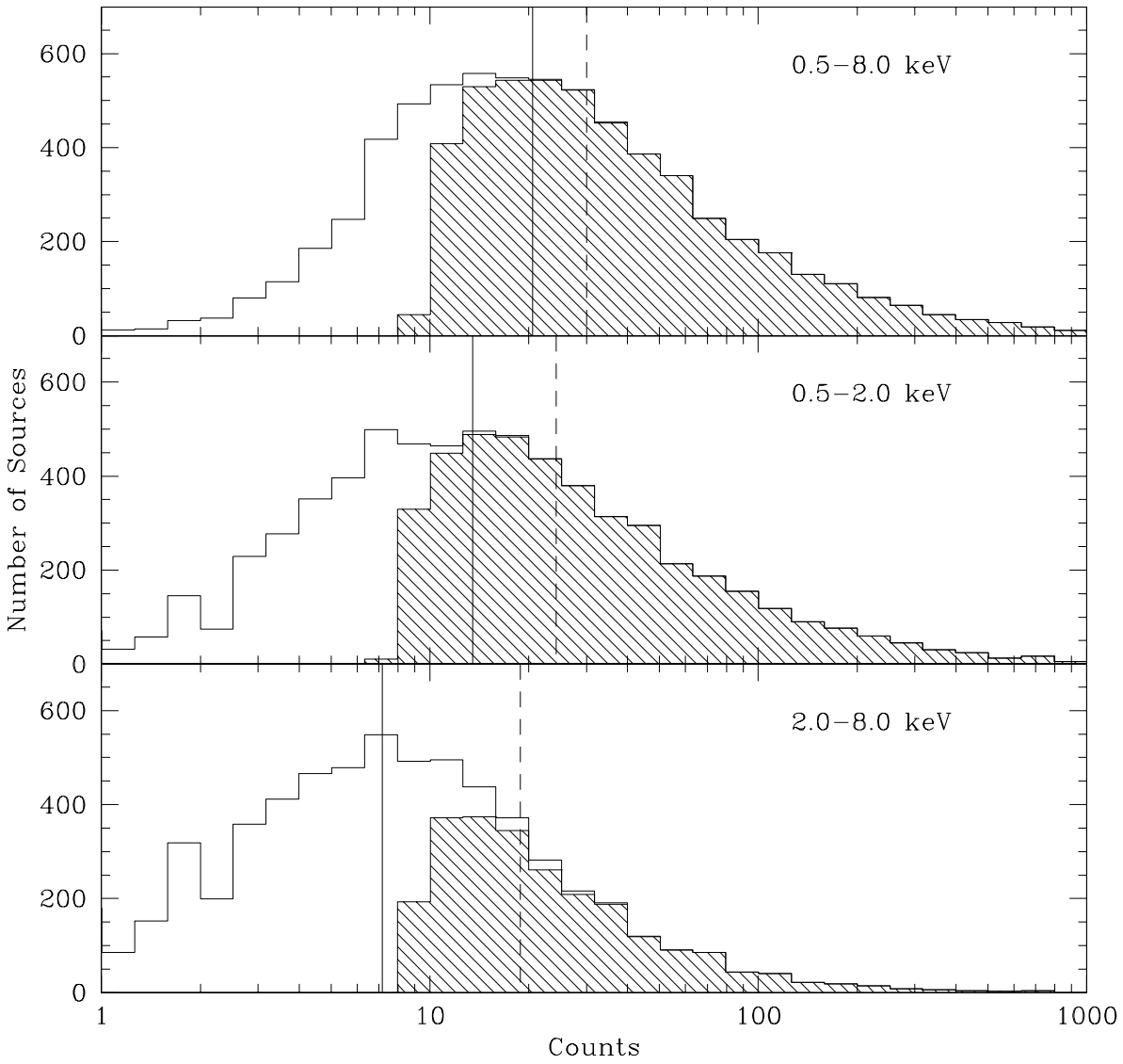

Fig. 16.— The distributions of source net counts in the Bc (*top*), Sc (*middle*), and Hc (*bottom*) bands, respectively. The open and shade histograms are for all sources and sources with $S/N > 2.0$, respectively, in each energy band. The solid and dashed vertical lines indicate the medians of the total sample and high S/N sample, respectively.

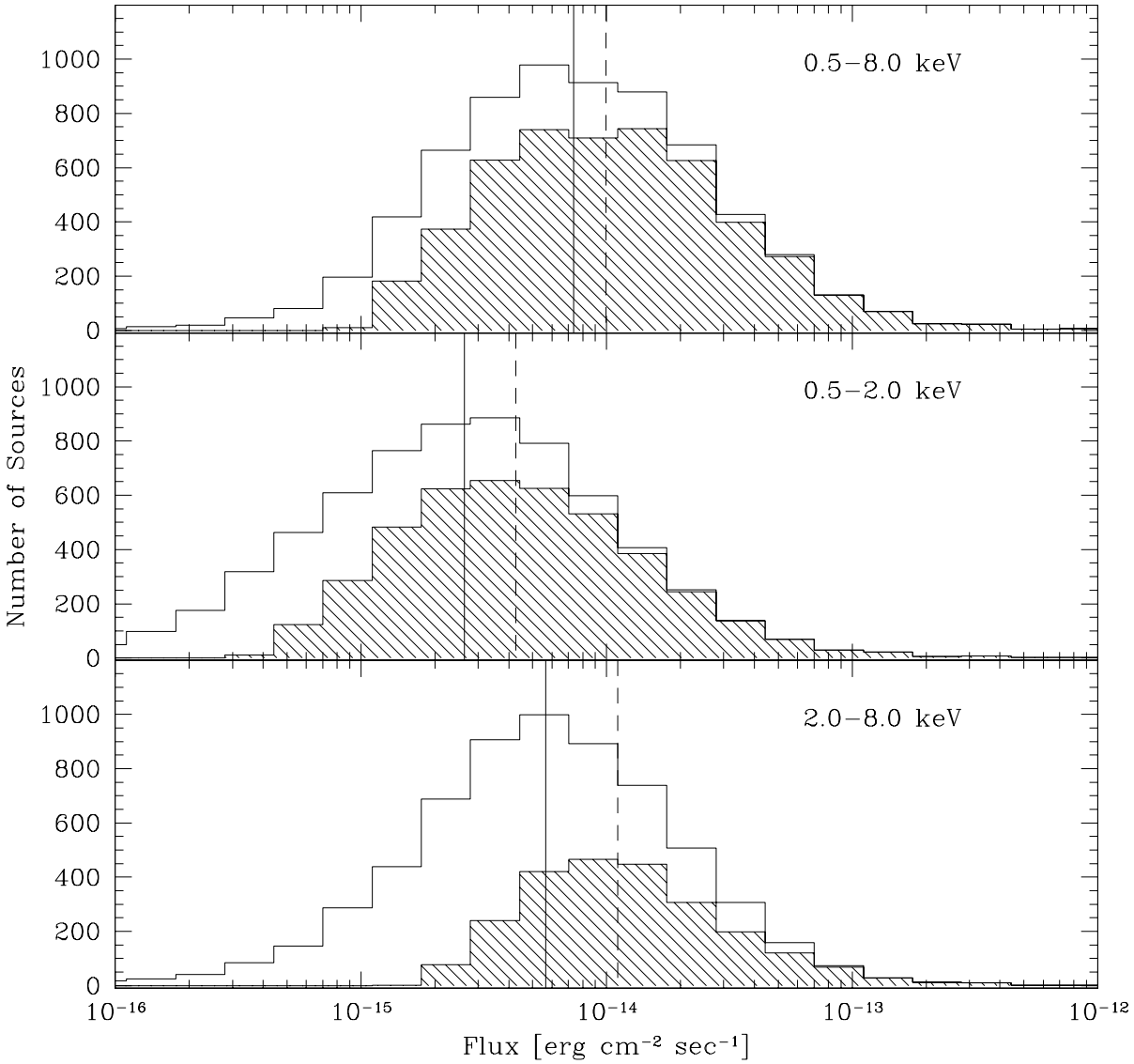

Fig. 17.— Same as Figure 16, but for flux. The flux was determined assuming a photon index of $\Gamma_{ph} = 1.7$ and Galactic absorption N_H.

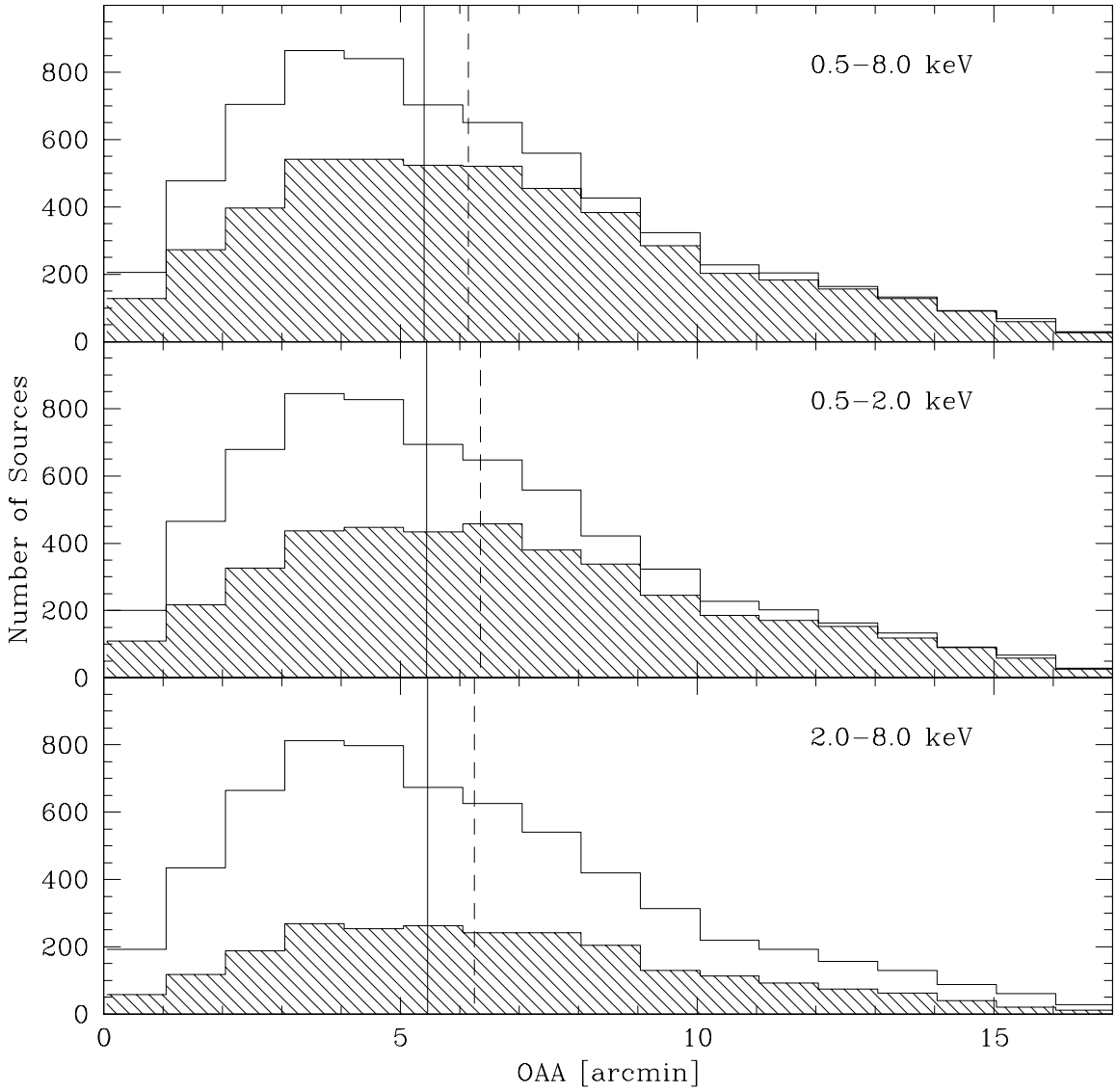

Fig. 18.— Same as Figure 16, but for off axis angle.

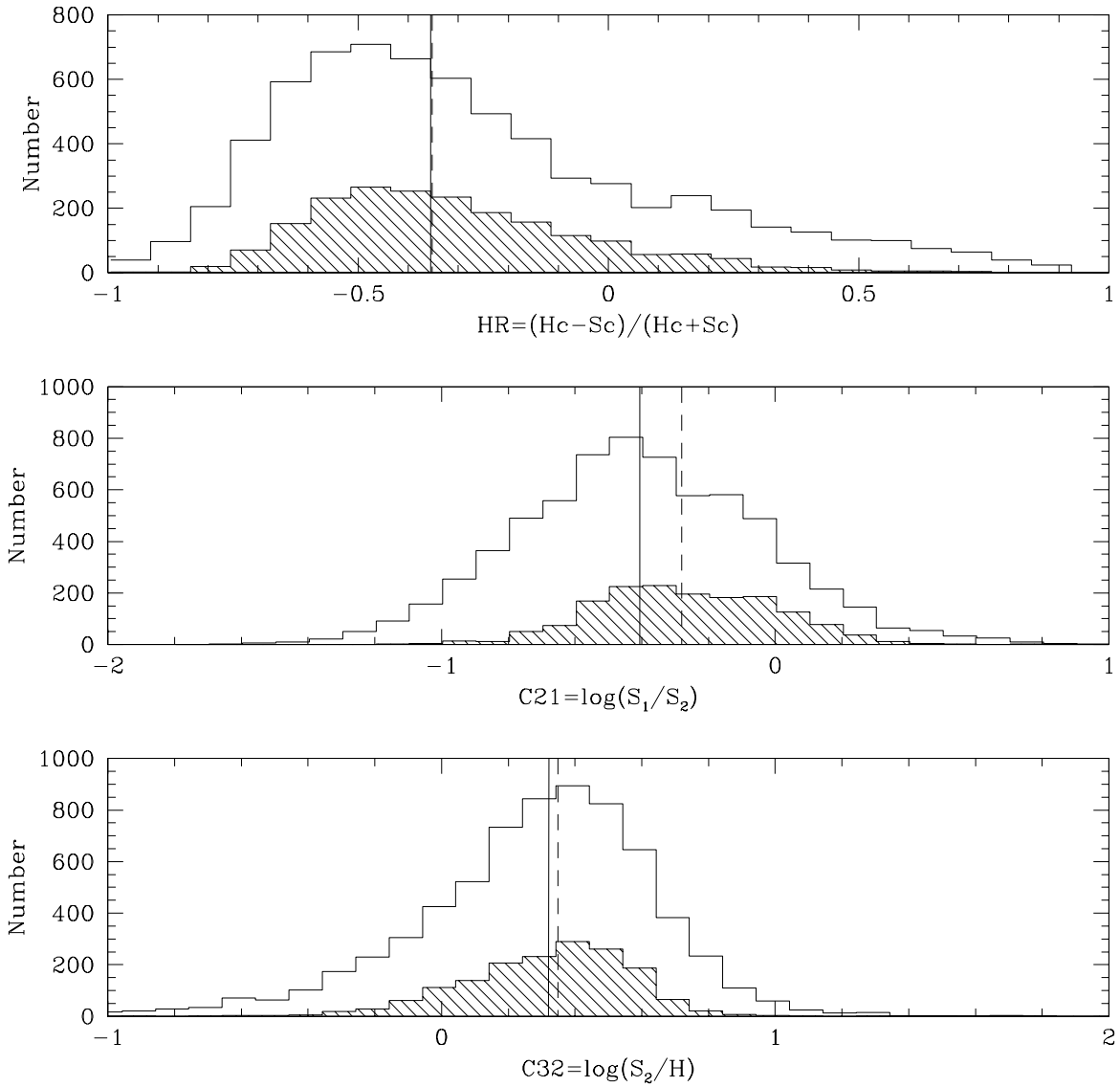

Fig. 19.— The number distribution of mean hardness ratio (*top*), the most probable values of the color C21 (*middle*) and C32 (*bottom*) of ChaMP X-ray point sources. The open and shaded histograms are for sources with $S/N \geq 0$ and $S/N > 2$ in both energy bands, respectively. This constraint yields a small number of shaded histograms. The solid and dashed vertical lines indicate the medians of the total sample and high S/N sample, respectively.

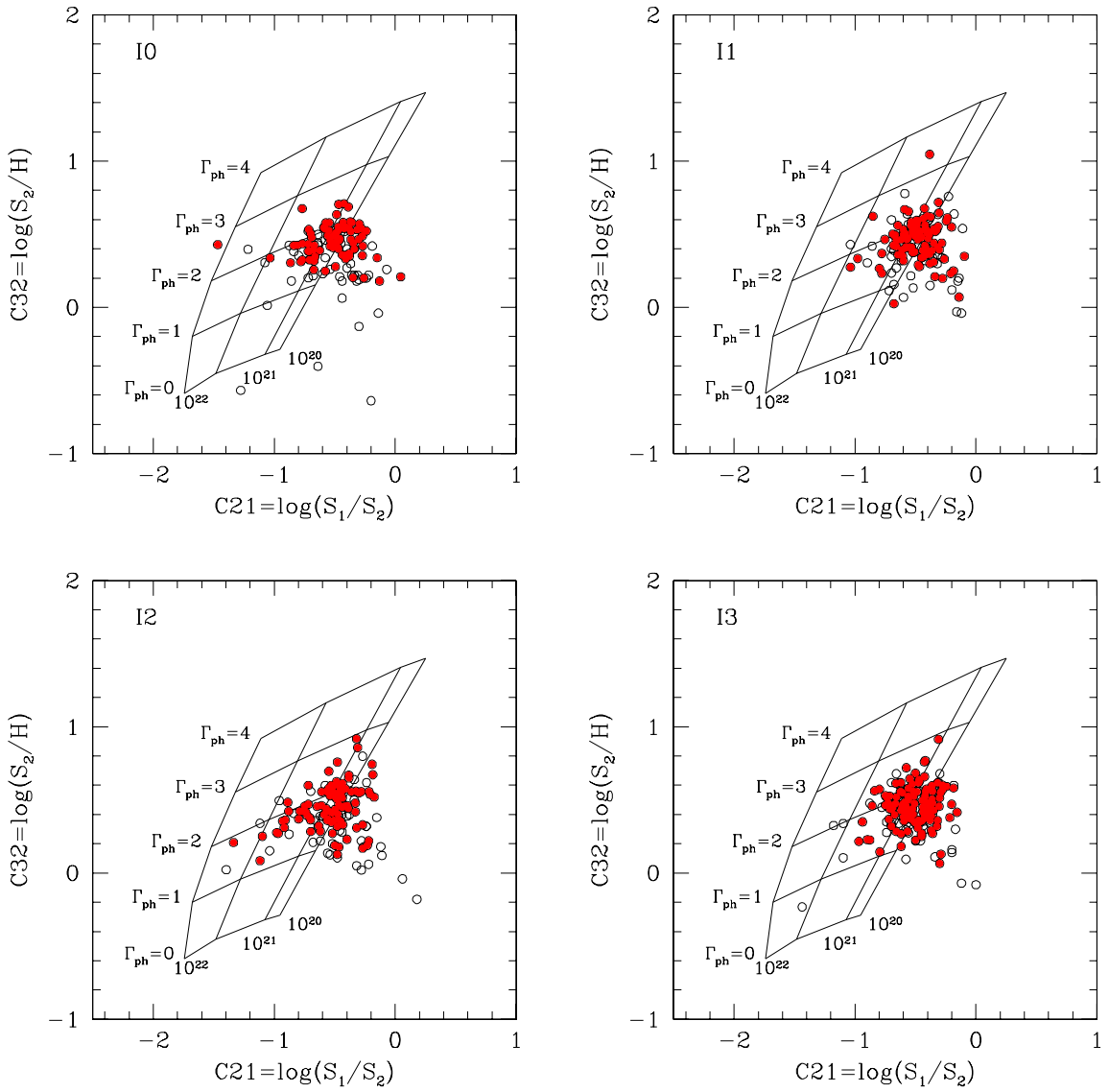

Fig. 20.— The color-color diagram of ChaMP X-ray point sources observed with ACIS-I. The open circles and red closed circles represent sources with $S/N > 1.5$ and with $S/N > 2.0$, respectively. The grid indicates the predicted locations of the sources at redshift $z = 0$ with various photon indices ($0 \leq \Gamma_{ph} \leq 4$, from bottom to top) and absorption column densities ($10^{20} \leq N_H \leq 10^{22}$ cm^{-2}, from right to left). Most sources are located within the ranges of Galactic absorption $10^{20} \lesssim N_H \lesssim 10^{21}$ cm^{-2} and photon index $1 \lesssim \Gamma_{ph} \lesssim 2.5$.

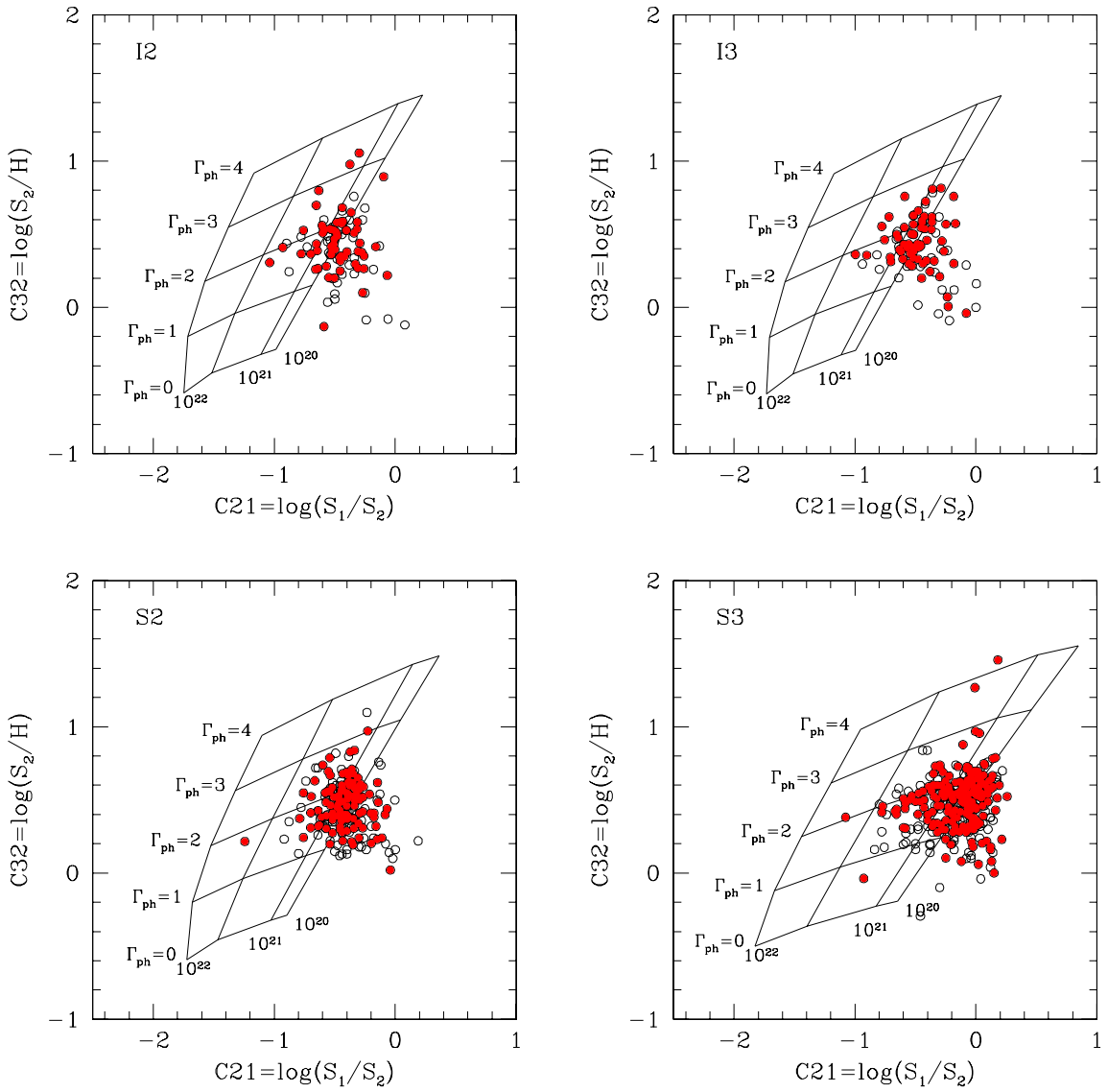

Fig. 21.— Same as Figure 20, but for ACIS-S observations.